UNIVERSITÀ DEGLI STUDI DI PADOVA

DIPARTIMENTO DI INGEGNERIA CIVILE, EDILE E AMBIENTALE

Department Of Civil, Environmental and Architectural Engineering

Corso di Laurea Magistrale in Environmental Engineering

TESI DI LAUREA

MODELING MULTIPLE FLOATING OFFSHORE WIND TURBINES WITH THE ACTUATOR LINE METHOD

Relatore:

Chiar.mo PROF. ERNESTO BENINI

Correlatori:

Chiar.mo DOTT. ALIREZA ARABGOLARCHEH

Laureando: FATEMEH REZAEI

Matricola 2088673

ANNO ACCADEMICO 2023-2024

Acknowledgments

This dissertation is submitted in partial fulfillment of the requirements for the master's degree in Environmental Engineering from the University of Padova. The dissertation includes the research work conducted during the period from April 2024 to October 2024, in collaboration with the Department of Civil Engineering and the Department of Industrial Engineering at the University of Padova.

I would like to begin by expressing my deepest gratitude to my supervisor, Prof. Ernesto Benini, from the Department of Industrial Engineering. His expertise, insightful feedback, and continuous support have been essential in shaping this thesis.
I also owe a great deal of thanks to my co-supervisor, Dr. Alireza Arabgolarcheh, for his insightful advice and continuous assistance. His feedback and collaboration have greatly enhanced the quality of my research, and I deeply appreciate his time and commitment.

I am also grateful to both the Environmental Engineering Department and the Industrial Engineering Department for providing the academic resources and opportunities that allowed me to complete this thesis in cooperation between the two fields. The interdisciplinary collaboration has been a rewarding experience.

Finally, to Nicolò and my family, who have always believed in me, even when I had stopped believing in myself.

Abstract

Expanding offshore wind energy is essential for achieving global renewable energy targets, particularly as fixed-bottom turbines are constrained by water depth. Floating Offshore Wind Turbines (FOWTs) provide a promising solution by enabling the deployment of wind farms in deeper waters, where wind speeds are higher and more consistent. However, FOWTs bring additional challenges due to platform motion, which affects the aerodynamics of the turbine and introduces complex wake interactions. This thesis presents the development of an Actuator Line Model (ALM) within the Open FOAM framework, designed to simulate the aerodynamic performance and wake behavior of FOWTs in a Triangular platform.

The ALM offers a computationally efficient method compared to fully blade-resolved simulations, accurately predicting the impact of wake dynamics on downstream turbines. This model integrates platform movement and aerodynamic forces, allowing for an in-depth analysis of critical performance metrics such as power coefficient, thrust coefficient, and wake distribution. The study focuses on different platform orientations and evaluates the influence of small angular deviations, which can result in substantial changes in wake behavior and turbine efficiency. These angle variations play a significant role in determining wake interference and turbine fatigue.

The results of this study show the critical importance of optimizing rotor orientation in triangular offshore wind platforms to reduce wake effects and enhance overall rotor performance. At T00, T10, and T70 rotor configurations, the downstream turbine is subject to significant wake-induced fatigue. In contrast, at T20, T30, T80, and T90 configurations the wake interference is reduced, leading to more uniform aerodynamic loading and better rotor efficiency. By capturing these dynamics, the ALM provides valuable insights into real-world conditions and enables better design and operation strategies for FOWTs, improving energy production and reducing fatigue-related maintenance.

This thesis utilizes a tool to simulate wakes on a triangular FOWT platform and highlights the importance of optimizing rotor placement and orientation to maximize energy capture, reduce mechanical strain, and ultimately lower the costs of operating offshore wind farms. The findings of the study provide a foundation for future research focused on reducing energy losses, extending turbine lifespan, and lowering the levelized cost of energy (LCOE) for offshore wind farms.

Keywords: Wind turbine, Actuator line model, FOWTs, Wake, Triangular Configuration

Table of Contents

Table of Figures

List of Tables

1. Introduction

Over three decades of research and innovation have driven the success of wind energy within the EU. By 2022, wind power accounted for 16% of the EU's electricity demand, with the Statistical Office of the European Union (Eurostat) reporting that it contributed 37% of the total electricity generated from renewable sources in 2021. Wind energy stands out as a crucial component in achieving the EU's energy and climate targets. The EU aims to have wind energy cover more than a third of its electricity demand by 2030, with projections indicating it could exceed 40% by 2050. Among various energy technologies, wind power has demonstrated one of the least adverse impacts on both human health and the environment. Over the past decade, innovations and economies of scale have substantially reduced the cost of wind energy, making it the most economical electricity source in numerous European regions today [1].

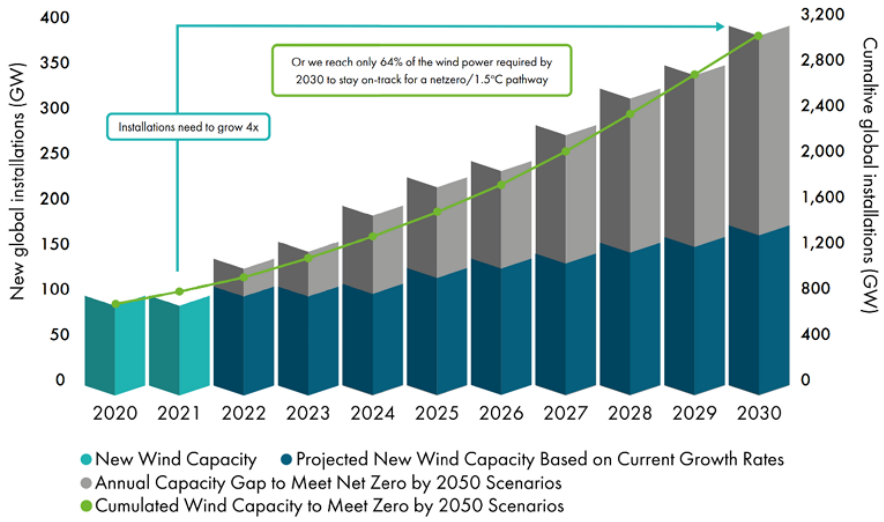

Figure 1. New Worldwide Wind Capacity Prediction 2020-2030 [2]

Offshore wind energy is a sustainable renewable energy source that is obtained by capturing the wind energy at sea, where the absence of obstructions allows the wind to travel at higher and more steady velocities. The first offshore wind turbine was installed in Denmark in 1991.

Since then, impressive advances have been made, both in terms of size and power. Development of new technologies and manufacturing systems have allowed the tip height to grow from 100 m in 2003 (3 MW turbine) to more than 200 m in 2016 (8 MW turbine), and the swept area to increase by 230%. Development is now focused on 15-20 MW turbines by 2030 (Figure 2) [3]. Net-zero goals for many countries rely on a massive expansion of offshore wind. According to the Global Wind Energy Council (GWEC), there is an expected surge from the current global capacity of 35 GW in 2022 to 380 GW by 2030. Currently, most offshore wind turbines are fixed. Supported by a structure that reaches from the bottom of the turbine tower to the seabed. Wind energy is stronger and more consistent in deep water areas: with approximately 80% of the practical offshore wind energy resource suited to water deeper than 60 m [4]. Before the development of floating structures, the placement of wind turbines in deep or complex seabed locations was impractical due to their reliance on fixed structures. However, with the advent of floating structures, which are moored to the seabed using flexible anchors, chains, or steel cables, wind turbines can now be placed far offshore. The utilization of floating wind turbines in deep waters is encouraged by several benefits, including steadier winds, reduced visual impact, and flexible acoustic noise requirements. A thorough understanding of the physical dynamics governing the response of the floating offshore wind turbines, as well as various design principles and analysis methods, is necessary to fully compete with conventional energy sources such as fossil fuels [5].

Figure 2. Installed Capacity (GW) of offshore Wind, 2019, IRENA [6]

The United Kingdom leads the world in offshore wind power installation with a capacity of 34% of total offshore wind installations, followed by Germany and China with 28% and 20% of total installations, respectively [7]. Offshore wind deployment is set to expand to Oceania and North America with the projects that would be built in the forthcoming years. Asia will become the prominent leader globally in offshore wind power commissioning in the next three decades, with a total capacity exceeding 100 GW by 2030 and 600 GW by 2050, as shown in Figure 2. Generally, the number of projects that are working on shifting towards floating offshore wind energy is increasing [8]. Now, the installed capacity of floating offshore wind turbines (FOWTs) is 121MW. However, it is projected that this figure will rise significantly to 18.9GW by the year 2030 and further to 264GW by 2050 [9]. The first significant research on FOWT platforms started in the 1990s, and the prototype of a FOWT was built in 2007. Since then, there has been a rapid expansion in FOWT research and development. In turn, this has led to a massive increase in the number of platform designs that are being developed and tested [10]. The investment growth decreases the Levelized Cost of Energy (LCOE), which is expected to be 40–60 €/MWh by 2030 [11]. Such price varies depending on the configuration and scale; however, the commercialization of FOWTs decreases the LCOE trajectory. The calculation of LCOE is usually performed based on the simplistic approaches of power calculation. The impact of turbine aerodynamics and its uncertainty still needs more study to have a more accurate LCOE [12].

In addition to structure design issues, FOWTs experience more complex aerodynamic phenomena compared to fixed-bottom HAWTs due to the platform motion [13]. Accurate prediction of aerodynamic load on wind turbine blades is essential for turbine design. The velocity experienced by the blade in FOWT varies due to several phenomena. The effect of blade element movement, the effect of the upstream rotor, and more complex phenomena such as interacting the blade with their own highly unsteady wake could result in dramatic large amplitude fluctuations in the aerodynamic load and power production. The flexibility of long slender blades in FOWTs can cause sudden blade deflections due to the mentioned load fluctuations. Considering the probable factors changes other turbine design concerns including lade materials and manufacture and control.

1.1 Offshore floating wind turbine design concepts

Increasing global offshore wind energy capacity is paramount to achieving Net-Zero goals. There are predictions that offshore wind will increase from the 2022 global capacity of 56 GW to 370 GW by 2030 and to 2000 GW by 2050. To accomplish this enormous expansion, wind turbines must be deployed in water depths at which fixed foundations for wind turbines are uneconomic or unfeasible as we will mention in the following part, so floating platforms become necessary. Floating offshore wind is still a relatively nascent technology, with only 121 MW of installed capacity globally as of 2022. However, a rapid scale-up is predicted, to an installed capacity of 18.9 GW by 2030. Allowing wind turbines to float introduces new challenges due to the platform moving in response to waves and wind. Wind turbines have mostly converged in design, but, as identified by Edwards et al. [14], floating offshore wind turbine (FOWT) platform designs are still evolving and diverging in design. Due to the recent rapid expansion in the number and diversity of FOWT platforms, an up-to-date review is needed.

In Edwards et al. [14], the authors reviewed the 22 FOWT platforms that have deployed a prototype, demonstrator, or farm-scale device at sea. In this work, the review is extended to 86 additional platforms either currently in the early (pre-deployment) stage of development or which never made it past this stage and are no longer being developed. The analysis of the platforms that have reached at-sea deployments yielded useful learning, highlighting design features and philosophies that are relied upon in commercial or near-commercial projects. However, larger-scale engineering necessarily becomes more risk-averse, and therefore it is informative to look at the evolution of early-stage devices. Trends in early-stage devices provide insights into the industry's past, current, and future priorities which cannot be seen from solely considering at-sea devices. To better understand these priorities, it is important to consider past early-stage trends that never made it to a larger-scale device, and how relative success, or lack thereof, in larger-scale devices has led to positive or negative feedback in early-stage devices. Furthermore, trends in recent early-stage devices ultimately help to predict future design directions and priorities.

Floating offshore wind has been studied since the 1990s. There have been a few review articles on platform designs during this time (e.g., Henderson and Witcher [15], Cruz and Atcheson [16,17], and Leimeister et al. [17]). However, there has not been a recent review on this subject,

and, over recent years, there has been a significant growth in the number and diversity of platform designs (for example, there have been at least 35 new platform designs in the past four years).

A balance among the two varying principles (i.e., the requirement for a stable foundation for the wind turbine's control and operation and the nature of the substructure being innate, to respond to environmental forces) is required for the design of the floating platform for wind energy [18]. As explained in Figure 3, the absence of rigid foundations results in an additional six degrees of freedom (DOFs) for the platform of floating turbines; three translational (surge X, sway Y, and heave Z) and three rotational (roll RotX, pitch RotY, and yaw RotZ). For the platforms of onshore wind turbines and bottom-mounted offshore wind turbines, the effect of soil-structure interaction (SSI) can be modeled with six degrees of freedom; three translational (horizontal forces in X and Y and vertical forces in Z), and three rotational (rocking moments in X and Y and a torsional moment in Z) respectively.

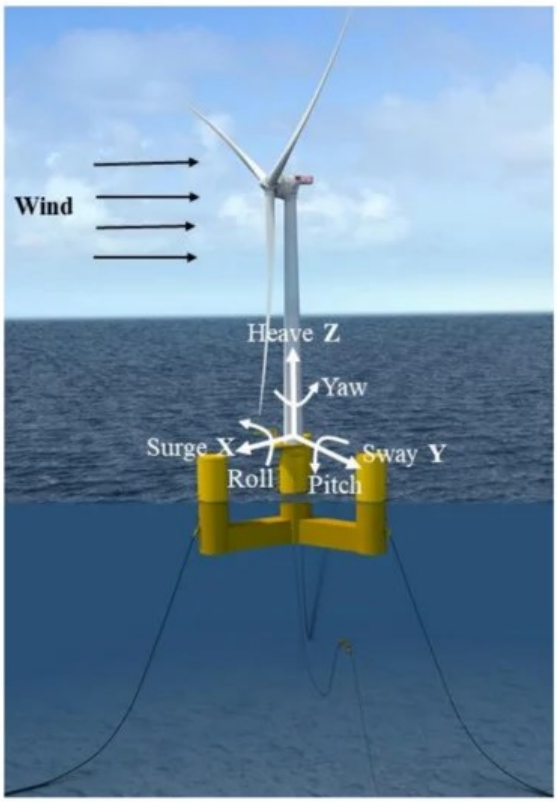

Figure 3. Six DOF for a floating platform, 2019, Naval Energies [6]

1.1.1. Single FOWT design concepts

The floating conditions require a new design and analysis of the rotor and its platform, which introduces new challenges. Different types of floating configurations for wind turbines have been or are being developed [19]. They include three main categories for fixed and floating support including monopile and tripod for fixed and barge, catenary moored semi-submersible platforms, the tension leg platform (TLP), and the spar-buoy with different characteristics [20]. These are mainly adapted from the oil and gas industry.

Each configuration has distinct characteristics. For instance, TLPs have smaller and lighter structures; however, stress on the tendon and anchor system is higher in these designs. Also, it can be said that the spar buoy is more suited to deeper waters (>~80 m) [21].

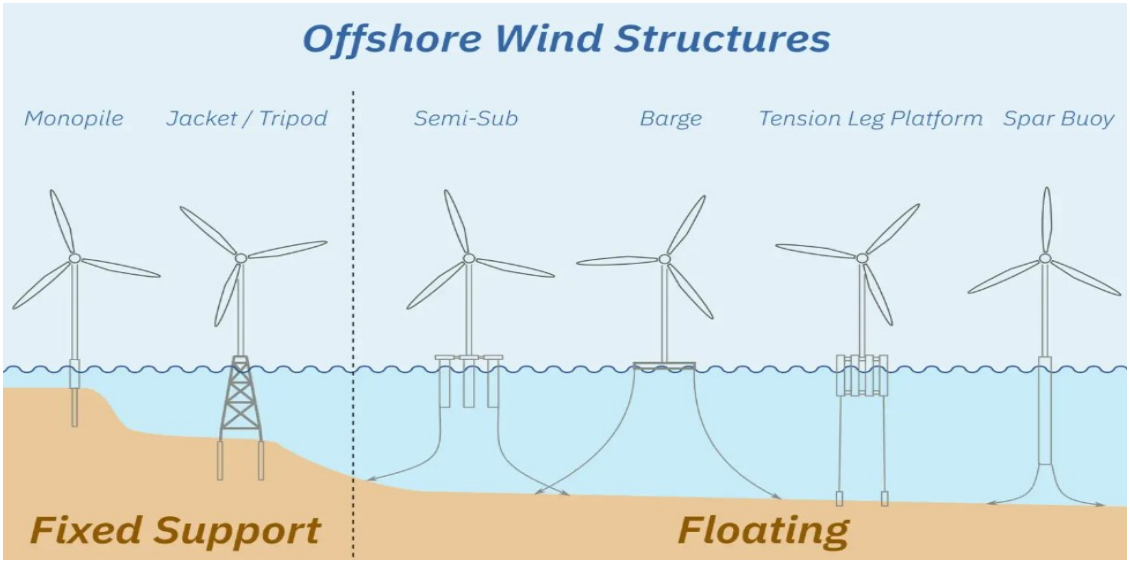

Figure 4. Offshore floating wind turbine conceptual designs [22]

More than 30 platform concepts have been proposed [22,23]. However, based on the primary mechanism adopted to satisfy the static stability requirements. A stabilization mechanism can be based on the following main stabilizing mechanisms or a combination.

1. Monopile

The most frequently used foundation type is the monopile. It commonly consists of a foundation pile and a transition piece, on top of which the turbine tower is placed. Foundation piles are made from steel plates which are rolled and welded together (as shown in figure 5).

Figure 5.Monopile foundation of offshore wind Turbine [24]

2. Tripod/ Jacket

A tripod foundation is a structure with three legs that diverge from a single node to their respective positions on the seabed. A foundation pile is driven into the ground at the base of each leg of the tripod section. On top of the tripod section, the turbine tower is placed. Complications with production and installation make it relatively expensive. The main transition node where the three legs meet the central column is sensitive to fatigue. Stiffness benefits are only interesting in large water depths, but then the base becomes restrictively large. The conventional installation method is to load several tripods onto a barge which is towed offshore. At a predetermined location, a structure is lifted off the barge, using a large crane (on the barge). Simultaneously, a smaller crane guides the tripod to its final position. The loads on the tripod structure will be mainly in the axial direction. Therefore, scour protection is generally not required.

Figure 6. Tripod on a barge, on their way to Alpha Ventus wind farm [25]

Jackets, also known as spaceframes or truss-towers, are relatively complex steel structures. Despite a reduction in construction materials (and hence weight), jackets are relatively expensive. At the water depth where monopiles become uneconomical, jackets take over. However, due to ongoing developments, the monopile concept is used for increasingly deeper waters, and the application of jackets is shifted to even deeper waters.

Figure 7. Senvion 5MW Turbine on Jacket (Ormonde Project)[26]

3. Ballast stabilized

The center of gravity of the entire system is moved below the center of buoyancy by placing massive ballast deep at the bottom of the floating structure. When the platform is tilted, this creates a stabilizing restoring moment that counterbalances rotational displacements.

Figure 8. Sketch of ballast stabilized floating wind turbine [26]

4. Buoyancy (or waterplane) stabilized

For this kind of stabilizing mechanism, the waterplane area has a central role in the restoring moment. A large waterplane area or smaller cross-sectional areas at a longer distance from the central axis can provide a significant second moment of area concerning the rotational axis. When a rotational displacement happens, it can create a larger stabilizing righting moment.

5. Mooring stabilized

When the structure is inclined, the restoring moment is generated by high-tensioned mooring lines.

Even though the floating platforms are utilized in different concepts, they can all be matched in the modified stability triangle concept that is represented in Figure 9. The position of Spars, semi-submersibles or barges, and tension leg platforms (TLPs), as three of the main platforms, are also pointed in this triangle.

A spar buoy is a ballast-stabilized cylindrical steel or concrete structure that resembles a fixed monopile foundation. Catenaries are usually used to keep it in place, but vertical taut spread cables are sometimes used to minimize heavy moments. Spar-Buoys are comparatively long, with lengths of up to 100 meters where most of the structure is submerged, to offer enough stability. Because of this, the device is often used in waters with a depth of more than 100 meters.

Semi-submersible platforms usually consist of three columns placed on the edges of a triangle. The wind turbine is either installed on one of these columns or in the triangle's center by a fourth one. This floater type involves two hulls; The top hull provides the necessary buoyancy to keep the platform afloat, while the ballast hull ensures the system's stability. In contrast, the waterplane-area stabilizer in the barge system is a plane structure. The semi-submerged structure protects the lower part from being affected by waves. The platform is held in place by catenary or taut lines made of wires, ropes, or chains anchored to the seabed, like Spar-Buoys.

Finally, the tension leg platform (TLP) is a mooring stabilized system. This method has been widely employed in the oil and gas industry for up to 1,500 meters of depth [23]. They are held in place solely by their updraft and mooring line tension. They are held in place solely by their updraft and mooring line tension. The base of tension leg platforms is fully submerged.

In contrast to semi-submersible platforms, they are kept in place by tensioned tendons rather than catenary moorings. Tensioned tendons are made up of metal or synthetic wires that are attached to the seabed using gravity or suction anchors or steel-driven piles.

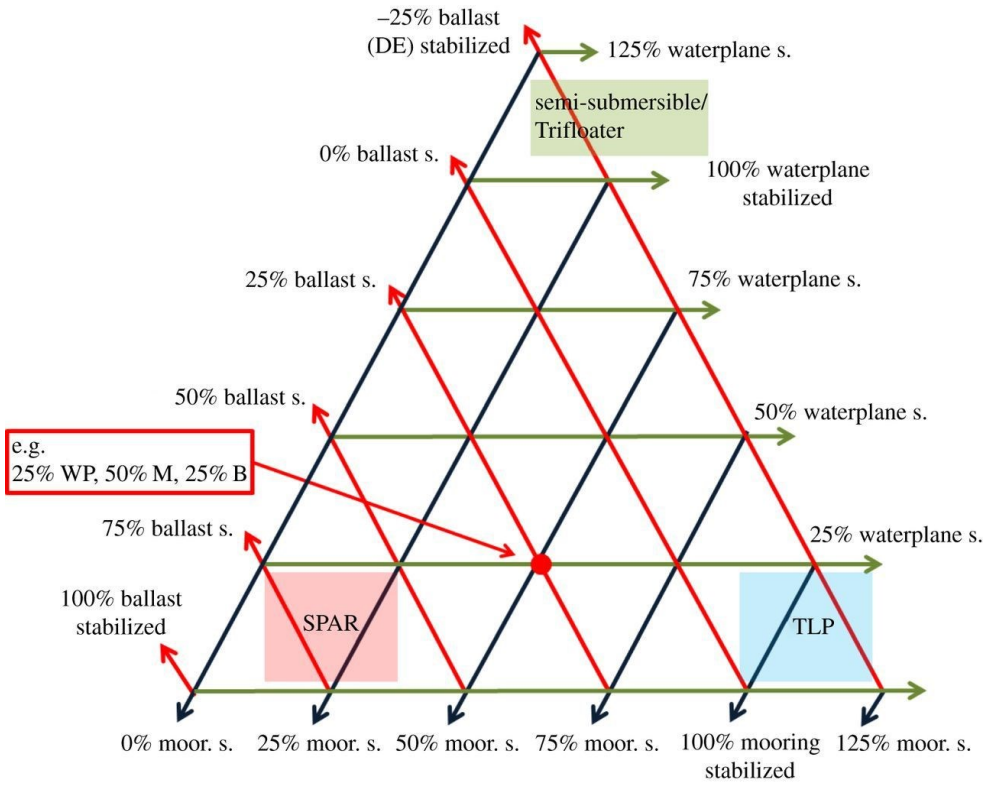

Figure 9 Stability triangle for floating structures [27]

The assessment of three main different floater concepts of spar, semi-submersible, and TLP is presented in Table 1. All the mentioned concepts have their advantages and disadvantages that need to be chosen based on the demand. The combination of these stability mechanisms leads to so-called hybrid floating concepts. As a result, the features of several systems can be merged into a single floating framework. Tension Leg Buoy (TLB) is a common hybrid floating concept that is a spar floater moored with tendons. For instance, the Floating Haliade by Alstom in France, the Ocean Breeze by Xanthus Energy in the UK, the TLB series by the Norwegian University of Life Science, and the SWAY or Karmoy in Norway. Nautica Wind Power combined a TLP with a semi-submersible to support a two-bladed wind turbine known as the single-point moored AFT (advanced floating turbine) [28].

Table 1. Advantages and Disadvantages of the main floater concepts

Type	*Advantages*	*Disadvantages*
Semi-submersible platform	• Most viable for deep waters • Low draft requirements • Low mooring costs [14,34] • Easy to tow	• Higher wave-induced motions • Complex structure
Barge Platform	• Less complex • Low anchor costs • Easy decommissioning	• Support structure is relatively expensive • Large wave-induced motions
Spar buoy platform	• Lower wave-induced motions • Higher stability • Simpler design	• High fatigue loads in the tower • Need deeper water
TLP platform	• Lower fatigue loads • Lower wave-induced motions • Simple structure	• Higher mooring costs • Hard to tow and install

To achieve the lowest overall cost of the whole platform system for its entire life, it is necessary to optimize the floaters for wind turbines because as the depth increases, the construction cost of the wind farm increases due to the floating foundation [29]. The breakup of the total cost of the system for a typical TLP-type floating offshore wind turbine is shown in figure 10, which includes the costs of maintenance, decommissioning, and operations.

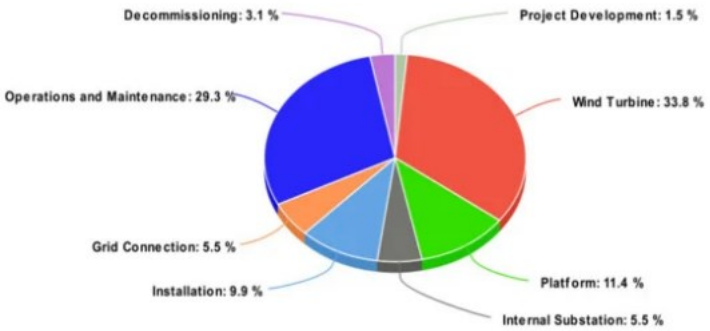

Figure 10. Cost Estimation for Offshore Wind Projects based on data from [30]

1.1.2. Multi FOWT design concepts

Wind energy has experienced significant growth over 30 years, becoming a crucial player in meeting energy needs. Placing wind turbines in deep or complex seabed areas was impractical due to reliance on fixed structures. However, with the emergence of floating structures wind turbines can now be situated far offshore. Research into the aerodynamic

performance of wind turbines has predominantly centered on grid-connected horizontal axis models. Enhancing the capacity and extending the blades of a single-rotor wind turbine (SRWT) are commonly seen as ways to boost its ability to harness wind energy [31]. These methods may create new difficulties in manufacturing and maintenance, such as increased production costs and higher demands for durable materials. Moreover, effectively coordinating the aerodynamic performance of each turbine presents a challenge for the development of multi-rotor designs [32,33].

Recognizing the constraints of SRWTs, attention has shifted to the concept of multi-rotor wind turbines (MRWTs) for wind energy extraction. Verma's research takes a deep dive into the past of MRWTs [34], all the way back to Denmark in 1873 when they first appeared with a twin-rotor design sporting six blades on each rotor [34]. Then, Percy H. Thomas came up with a clever patent for a two-rotor turbine, aiming to find the spot between efficiency and cost with each rotor having just two blades [34]. Henk Lagerweij from Lagerwey Wind has put up MRWT prototypes to tackle engineering problems, like how these multiple turbines interact with each other [35]. Just a few years back in 2016, Vestas teamed up with the Technical University of Denmark to unveil a prototype of a four-rotor MRWT, proudly boasting about how much better it is compared to the old single-rotor models [36].

MRWTS offers distinct advantages over their large-scale SRWTs. MRWTs feature smaller and medium-sized blades, resulting in benefits such as long blade lifespan, reduced weight, and faster rotation. Studies have consistently shown that MRWTs, with their smaller blades, are more efficient at capturing wind energy compared to SRWTs. Research by Laan et al. [37] Explored the power output of MRWT wind farms and found that they could generate 0.3–1.7% more electricity annually than equivalent single-rotor wind farms. Zhao et al. [38], Investigated blade loads in multi-wind turbine wind power systems under varying wind conditions. Their findings suggested that replacing a single large turbine with multiple smaller ones could mitigate the effects of wind. While MRWTs offer promising benefits, concerns about their manufacturing and maintenance persist. Jamieson and Branney analyzed a 20 MW multi-rotor wind turbine design, finding significant cost advantages over single-turbine designs [39].

A crucial aspect of designing wind turbines is understanding how air flows around them, known as aerodynamics. This becomes even more important when multiple turbines are placed

close together, as they can affect each other's performance. Smulders and colleagues conducted wind tunnel tests with two turbines side by side and found that, together, they produced slightly more power than expected [40].

Although multi-rotor turbines have many potential benefits, little is known about how complex wakes and the airflow patterns left behind them affect each other. Understanding multi-rotor turbine wakes is of both practical and fundamental importance. Several studies have investigated this matter. Ghaisas et al. [41], Found that the wake behind a multi-rotor turbine was less turbulent and recovered more quickly than behind a regular turbine, especially when the rotors were spaced further apart. Speakman's research showed that changing the angle of the turbine blades could affect how much the wake spreads out, potentially making wind farms more efficient. [42] Bastankhah et al. [43], Explored the effect of different geometric configurations on multi-rotor turbine wake characteristics. They found that the recovery rate in multi-rotor turbine wake increased with an increase in rotor pitch. While the effects of rotor number and rotation direction on wake recovery were not significant. However, these studies have their limitations, often using simplified models that may not fully capture the complexities of airflow near the turbines.

Initially, two concepts for multi-turbine platforms will be examined. Following this, there will be an overview of the description, status, advantages, and disadvantages of both single and multiple-turbine platforms. Finally, an innovative idea for a multi-turbine floater will be introduced.

One multiple-turbine concept consists of a single pontoon-type floater (semi-sub) with several turbine towers on it to share anchor costs and provide wave stability as seen in the figure below. Another concept in multi-floating offshore wind turbines is called wind hunter, the wind hunter concept is a portable system that allows a huge floating platform to travel the high seas and anchor in a windy spot. This is just in its concept advantages but could have potential. Most existing sea-based wind turbines are fixed now at an enormous cost and are only as effective as the wind present in that area as shown in Figure 11.

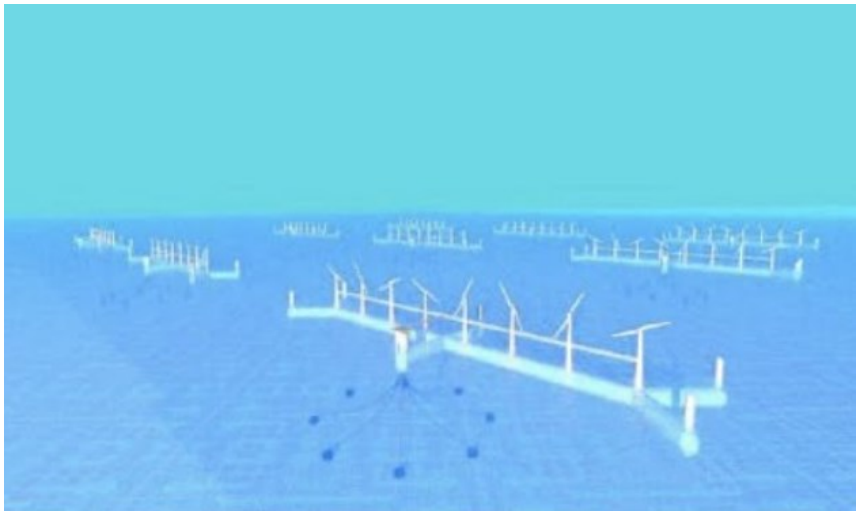

Figure 11. A single pontoon-type floater with several turbine towers on it [44]

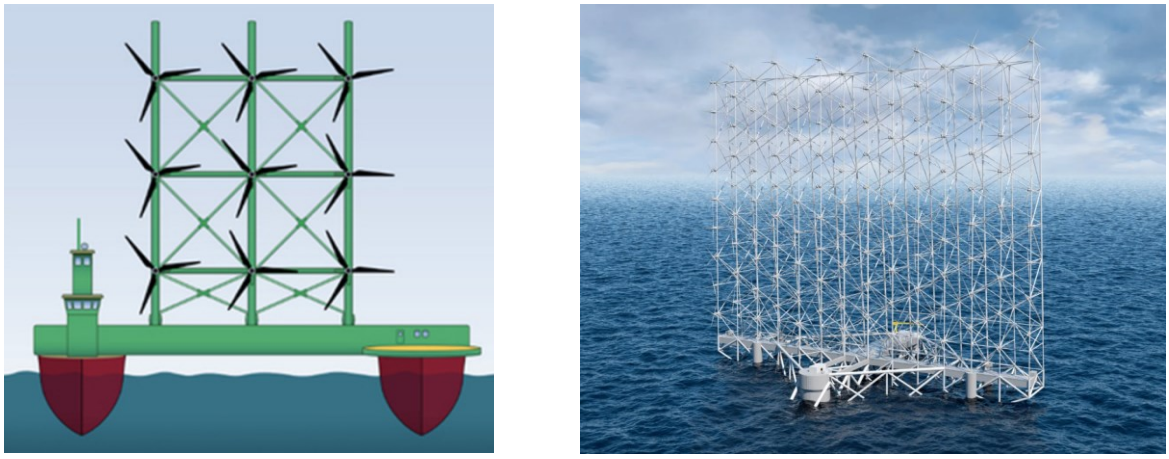

Figure 12. Wind hunter System[45,46]

The Wind hunter system concept is an offshore, floating system that uses several wind turbines for power output to produce hydrogen by electrolyzing water. This continuously manned, safe, and stable system will be easily maintained on board while relocating to the best wind conditions for the wind turbines. The produced hydrogen gas may be compressed and stored as gas or liquefied and placed in insulated tanks. The compressed or liquefied hydrogen may be transferred by helicopter, surface ships, or by other means.

Another multiple-turbine concept is to place an array of smaller turbines on a single tower and platform. In an analysis of the first concept, it was determined the cost would be very high and it was questionable whether the large structure could withstand extreme wave loading as shown in Figure 8, an agreement of SSAB and Hexicon, to develop far offshore platforms. The

combined technology will offer advantages within the market for renewable energy. A first demonstration unit is planned for Swedish waters in 2017. Hexicon will together with SSAB optimize the steel material in the foundation of the wind platforms to ensure functionality and cost-effective solutions during their complete life cycle. The floating foundations with several wind turbines enable efficient wind park configuration in locations where winds are stronger and environmental impact is reduced [47].

Figure 13. SSAB, Hexicon to optimize steel for offshore wind platforms[48]

Because turbine spacing is poorly optimized, both multiple-turbine concepts require the floating structure to either yaw with wind direction changes or compromise energy production when the wind shifts off the prevailing direction. Systems consisting of multiple turbines on a single floater may prove to be more expensive than single-turbine floaters because of the additional support structure required to connect several rotors or towers. However, for very large systems (>20-MW per structure) it may be possible to lower overall system weight with multiple turbines due to cubic mass scaling laws.

In advance the WindSea Project [49] Done by this concept, three turbines on one platform meant that you could significantly increase the output of each offshore wind turbine platform. The unit was designed with unique scalability considering the assumed increase in turbine capacity. The original design had a total capacity of 9,6 megawatts, 300% more than any other windmill design at the time. The units were made ready at the dock, requiring only an 8-meter water depth at the dock, allowing for plug-and-play once placed on-site.

Figure 14. The Wind Sea concept [50]

1.1.3 Single and Multi-Turbine Turbine Comparison

In the past, many windfarms simulations were performed using a single turbine to represent the entire wind farm, it is like representing a conventional power plant with a single large synchronous generator, it has been very successful for predicting instabilities, such as sub-synchronous resonance, in simulating conventional large synchronous generator power plant. A wind farm is usually very large and there are diversities in the wind farm (wind speed, line feeder impedance, etc.) that make individual turbines respond differently to the same fault. In a real wind farm, there are many wind turbines connected to the point of interconnection. Most of the generators used are induction generators or a combination of generators and power converters. As shown in Table 2 here is a general comparison between single and multi-wind turbines.

Table 2. Single and Multi FOWT comparison

FOWT	*Advantages*	*Disadvantages*
Single-turbine-floater	• Simplicity • Modularity for manufacture • Lower structure requirement • Standard yaw control options	• Individual anchor costs
Multiple-turbine-floater	• Wave stability • Shared anchors • Mass optimization possibilities	• Hight cost support structure • Wave loading • Complex yaw control

1.2 Analysis approaches

Analyzing and designing Floating Offshore Wind Turbines (FOWTs) presents greater complexity compared to land-based counterparts and existing offshore structures. This complexity arises from the multifaceted nature of the involved physics, encompassing aerodynamics, hydrodynamics, and structural dynamics, including mooring cables analysis. When selecting a numerical modeling method, there's a crucial balance to strike between accuracy, fidelity, and computational efficiency, considering the phenomena under study and the desired data precision. Fidelity pertains to how much simplification is applied to the physics involved and the level of confidence in the model's accuracy. Computational efficiency, on the other hand, measures the time required for the model to simulate a problem with standard computing equipment. Numerical models are categorized into low-, mid-, and high-fidelity, with higher fidelity demanding more computational resources and potentially compromising computational efficiency. The choice of fidelity level depends on the simulation's objectives and the required level of analysis and precision. During the initial phases of Floating Offshore Wind Turbine (FOWT) design, low-fidelity models are typically employed for sizing analysis and optimization. As the design progresses, mid-fidelity models, also known as engineering-level tools, come into play to examine the operational and challenging conditions faced by FOWTs. High-fidelity models are then often employed for thorough investigations during the final design stages, particularly for accurately assessing structural stresses. It's common to adopt a multi-fidelity approach, incorporating elements from each level of fidelity models at various stages of the design process.

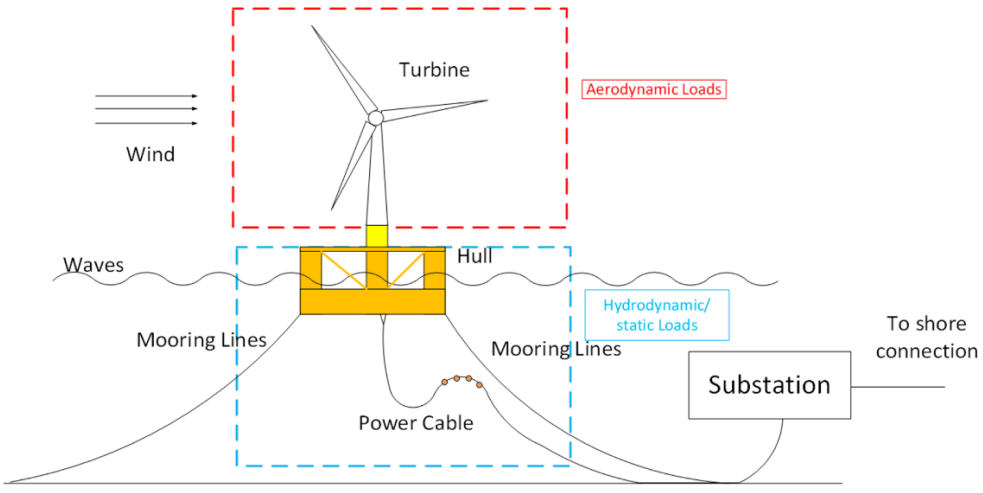

Figure 15. Basic components of a floating wind turbine along with the key physical effects [51]

1.2.1 Hydrodynamics

More investigation is required to fully comprehend the interaction of ocean waves and wind turbines. This interaction is essential for many reasons some of which are mentioned as follows:

a) Because some of the structures' natural frequencies may overlap within the bandwidth of the ocean wave spectrum, this contact might generate resonance.

b) Higher natural frequencies in TLP can be near to sum-frequency wave loading, resulting in ringing.

c) In spar buoy and barge systems, the lower natural frequencies can be close to difference-frequency wave loading and create slow drift motions.

Numerical modeling approaches for hydrodynamic issues were created primarily for the marine and offshore oil and gas industries, but they can also be utilized for FOWT floaters and platforms. For the computation of first- and second-order wave excitations, the Potential Flow technique, the Morison Equation, or a combination of the two is utilized. These approaches provide the necessary accuracy with a reasonable computing cost, but they can have issues with complex geometries.

The diffraction/radiation approach is divided into first-order, second-order, higher-order, and nonlinear methods that are based on the potential flow theory (concerning wave steepness). The oscillation amplitudes are assumed to be minimal compared to the floating body's cross-sectional area, and viscous effects are neglected. The floating body is divided into panels in this technique, and hydrodynamic loads are calculated by integrating the dynamic pressure across the wetted panels. Submerged geometry is the hydrostatic equilibrium in still water.

The Morison equation is used for structures that include slender cylindrical members. It can simulate structures in waves and currents, as it models inertial loads and viscous loads, unlike the potential flow model. Morison et al. [52], Developed this empirical equation for infinitely long cylindrical offshore structures. The Morison equation is limited as it ignores the floating body's effect on the incident wave field.

When either the PF methods or ME is insufficient to capture certain hydrodynamic phenomena, a combination of them can be utilized. This can be considered a computationally efficient alternative for CFD modeling. The hybrid method can be utilized for platforms that

include large columns and slender braces or when the viscous drag effects resulting from severe sea states are present.

The high-fidelity CFD models can capture complex flow problems such as vortex shedding around heave plates. Due to the high computational cost of CFD, it is usually just employed to tune model parameters for lower fidelity models. It is complicated to draw direct comparisons between the accuracy of CFD models and PF + ME models. A variety of parameters are involved in determining the model's accuracy. Performing the simulation by steady-state equations or transient equations, the investigated load cases, tuning the hydrodynamic coefficients, mesh characteristics, and user competence, and confirming a converged result for the CFD model are some involved parameters. Also, the calculation of the second-order PF solution, rather than first-order wave stretching, and the correct viscous damping in the model are involved in the accuracy of the PF + ME solution [53,54].

1.2.2 Mooring cables

Mooring systems allow floating constructions to be employed in deep oceans where standard jacket foundations are either too expensive or too difficult to install. The mooring system, which is normally made up of a series of cables, provides the structure with both station-keeping and dissipation effects. The design goal is to have a mooring line system with durability to resist external forces but show stiffness properties for the FOWT platform to work beyond the wave excitation frequencies. The initial step is selecting the anchor based on a soil's holding capacity. The number of anchors required should make a balance against the external forces applied on the FOWT. The minimum breaking strength, or MBS, of a line, is then determined by its holding capacity. Following that, mooring properties, including line material, line length, and clump weights, are chosen based on a desired performance requirement. After that, iterative simulations are done to see if the line meets the required safety margins [55].

Many factors should be considered in the adopted mooring design, including material fatigue properties, anchor holding strength, seabed clearance and between other subsystems, breaking loads, special considerations for fiber ropes (for example, compression fatigue and creep characteristics), tower and wind turbine motion limitation, and permissible platform offset. These factors should be balanced with the environmental loads.

Mooring systems usually consist of a combination of the following elements:

- Mooring line: Wire rope or Fiber (synthetic) rope

- Anchor: Drag embedment anchor, Plate anchor, Suction pile, Pile and screw anchor, or Gravity anchor
- Clump weights and buoyancy modules.
- Connection equipment and hardware: Triplite, Shackle, or Splices

1.2.3 Aerodynamics

The fluctuation in relative wind velocity caused by platform motions is the most challenging factor in the aerodynamics of FOWTs. Dynamic inflow, also known as unsteady dynamics, is a phenomenon that can cause rotor thrust loading to overshoot, resulting in negative damping. An accurate simulation is crucial for estimating power output. In addition to improving power generation, the turbine controller should also minimize the consequences of dynamic inflow [56]. Moreover, an appropriate aerodynamic simulation is vital for assessing fatigue reduction [57]. And blade lifetime prediction. The evolution of turbine wake and its effects on the turbine dynamics, downstream turbines, and FOWT farm layout is another important issue that needs to be investigated.

As previously stated, choosing the appropriate numerical method to utilize within the design stages is a trade-off between the available time and monetary budget and the required level of uncertainty and accuracy. The following section presents a review of the conventional method and prior research.

1.3 Prior works

Nowadays, the wind industry faces challenges in developing wind farms [58]. The wakes of wind turbines interact with each other in the wind turbines downstream as well as with the turbulent atmospheric boundary layer (ABL) [59]. The increasing interest in Floating Offshore Wind Turbines (FOWTs) has triggered numerous research efforts in various directions including, for instance, floaters, mooring lines, hydrodynamics, aerodynamics, structural fatigue, and a further interest in upscaling rotors. Now, the main challenge that needs to be overcome is the high Levelized Cost of Energy (LCOE) as mentioned by Bosch et al. [60] and Kausche et al. [61]. Improving blade design and performance remains an important topic to address the LCOE problem [62]. With improved loading predictions, blades can be designed better, and maintenance schedules can be driven by informed guidelines. Despite the good knowledge accumulated in the past twenty years or more for the fixed rotor situation, the

floating rotor exhibits highly complex three-dimensional motions because of the hydro-aerodynamic interactions acting on the whole structure. The resulting wake flows are, therefore, increasingly complex because of phenomena such as blade-vortex interaction, vortex-vortex interactions, blade flow three-dimensionality as well as unsteady airfoil behavior and dynamic stall. Due to these intrinsic complexities, current research efforts in hydrodynamics and aerodynamics remain mainly uncoupled, with few exceptions such as Wang et al. [63] and Liu et al. [64]. Concerning hydrodynamics, full-body Navier-Stokes simulations have been used to predict loading on both the foundation [65], as well as mooring lines [66]. More simplified methods based on the FAST (Fatigue, Aerodynamics, Structures, and Turbulence) code, developed by the National Renewable Energy Laboratory (NREL) [67], have been used for the analysis of these loads by Roald et al. [68]. Chan et al. [69], also developed an approach using fluid-impulse theory for load calculation and implemented a module in FAST. Experimental measurements of hydrodynamic loads have also been carried out by Shin et al. [70]). Apart from information on loads, better hydrodynamic models allow for a better prediction of the motion of the wind turbine. With an uncoupled aerodynamic approach, such motions must be prescribed and therefore this information becomes essential in the study of FOWTs. The uncoupled high-fidelity aerodynamic analysis of FOWTs, such as Computational Fluid Dynamics (CFD) simulations, mainly employs prescribed platform motions obtained from lower-fidelity coupled analysis tools, such as FAST. This uncoupled approach could already be very insightful concerning elucidating the novel unsteady aerodynamic phenomena associated with FOWTs and, thus, could be employed to improve the lower-fidelity models. In addition, these are useful since they provide a quicker alternative to coupled simulations and can provide an accurate description of the physics (see Sebastian and Lackner [71]). FOWTs experience various motions of the platform, and they have distinct effects on the wake aerodynamics. Among the motions, the pitching and surging platform motions are identified as the two dominant motions for FOWTs [72], therefore, the majority of the literature has focused on these two motions. The effects of platform pitching motion on rotor power performance and wake were investigated by several authors such as Fang et al. [73], Fu et al. [74], Shen et al. [75], and Leble and Barakos [76]. For example, Wen et al. [77] studied the rotor power for different tip speed ratios and reduced frequency and showed that the power variation increases with increasing tip speed ratio and reduced frequency. This is consistent with earlier findings from Sant et al. [78] and Micallef and Sant [79] in independent

experimental and numerical campaigns, respectively. Alternative approaches such as the use of vortex lattice methods (VLM) to study the effect of platform pitching were carried out by Jeon et al. [80], where the presence of a turbulent wake state was also noted under low-speed inflow conditions. Lin et al. [81] report full-body rotor CFD computations involving both pitching and surging motion to analyze the unsteady aerodynamics of the rotor. Surging is the other dominant platform motion for FOWTs and has received attention in the literature and is also the focus of Rezaeiha et al. [82].

Analytical modeling

In wind turbine modeling, modeling of physical induction inflow near the rotor disk is an important issue. Even using the elliptic formation of Navier–Stokes equations around a turbine shows that a disturbance signal downstream affects the flow in the rotor disk and upstream. However, due to complexity and higher computational cost, elliptic solutions techniques are not commonly used [83]. Vortex modeling is another method for rotor wind speed calculations in which lifting lines or surfaces represent the blades and the vortices[84].

The parabolize Navier–Stokes equation, which is more common than the two mentioned methods, simplifies Navier–Stokes by ignoring the diffusive momentum transport term in the primary flow direction [85]. This method omits the pressure gradient term along the transverse direction to have a more straightforward equation that is commonly used in engineering problems [86]. The actuator disk or 1-D momentum theory is usually applied to calculate induced velocity components in parabolic flows.

The actuator disk (1-D momentum theory) approach is based on the momentum theory. The wind turbine is modeled as an actuator disk in this model, assuming an infinite number of blades. The flow is considered steady, inviscid, non-rotational, incompressible, and asymmetric with constant pressure profiles. The thrust is also assumed to be uniform over the disk area and a constant velocity through the disk [87,88].

The inverse 1-D momentum theory approach, as described in[88], is a simple approach for the estimation of forces applied to the rotor plane. Some researchers have combined it with a CFD algorithm in which conventional thrust curves are calculated according to induced velocity, whereas the conventional method was according to U_∞ [89].

Blade Element Momentum (BEM) theory, introduced by Glauert [90], is one of the most used methodologies for investigating turbine aerodynamics. BEM depends on blade aerodynamic characteristics and the Cl and Cd of the blade section. In BEM, two equations for axial and tangential forces are written, and estimating the induction factor for velocity is solved by an iterative algorithm [91,92]. This method is beneficial from the computational cost point of view, compared to numerical methods like CFD or Lattice Boltzmann methods (LBM). In terms of accuracy, the results of this method are satisfying in the case of the availability of airfoil data [93]. Nevertheless, its initial formulation had a shortage of modeling phenomena such as angular movement of the platform and wake.

In general, the turbine wakes are studied in two regions: i) a near-wake region that starts right downstream of the rotor and extends until about two rotor diameters, and it is followed by ii) the far-wake region that is developing further away. In region i), the formation and development of the flow are mainly influenced by how blade shapes affect the tip vorticities and can be simulated by using flow field solvers (e.g., CFD or LBM). In the second region, which is indeed relevant to wind farm design, the wake's effect is primarily characterized by growing turbulence intensity and reduced average wind speed [94]. Atmospheric turbulence also influences the far-wake region, which accelerates wake recovery for velocity deficit and turbulence intensity [95].

Even by calculating turbine wake using high-fidelity methods, the wake superposition concept is a source of error in wind farm wake modeling. Geometric sum, Linear sum, Energy balance, and Quadratic sum are four approaches that are mainly used for this purpose [96]. Van Leuven considered the effect of the closest turbine in his model. His approach worked well for the Zeebrugge wind farm [97]. However, for offshore wind farms, where the wake effects can be more dominant, the importance of the wake superposition method is even greater [98]. Habenicht [99] Compare the mentioned superposition methods for four different offshore wind farms. His results showed that linear and quadratic methods give less error compared to others.

For simulation using BEM theory, some models for investigation of the wake are developed. Frandsen [100] developed an infinite wind farm boundary layer (IWFBL) model according to the difference in shear stresses above and under the turbine hub height. The Jensen wake model [101,102] considers a control volume from the rotor plane to the point. It is assumed that wakes expanded linearly, and flow is axially symmetric, with no rotation, no turbulence, and a conic-

shaped wake profile. Based on this model, the PARK model was developed to consider the effect of multiple wakes on the velocity [103,104].

With a simple wake calculation procedure, the Larsen model was introduced first in 1988. Initially, this model was derived from the axis-symmetric form of RANS equations by neglecting the pressure term [105,106]. Since this version was derived for considering the single wake case, it was redeveloped in 2009 to provide a solution for multiple wake situations. In this version, boundary conditions are defined at the rotor plane and at a distance of 9.6D downstream [107]. The dynamic wake meandering (DWM) model considers wakes as passive tracers driven by the large-scale turbulence structures in the atmospheric boundary layer. This model is based on equations for velocity or wake deficit, meandering of the wake, and rotor-added turbulence [108,109].

In the offshore application of wind farms, specifically for floating turbines, the dynamic stall is a potential phenomenon that is due to the turbine's forward-backward motion that leads to oscillation in the angle of attack. The pitch, surge, and other wind turbine movements can considerably affect the flow field around wind turbine blades. The mentioned theories have a fundamental limitation as they are not able to let the 3D flow across various rotor radial elements. The suitability of models that consider the transient nature of the flow, e.g., dynamic wake models (see [110,111]), and it was showed for floating configurations, more advanced approaches are necessary.

Computational fluid dynamics (CFD)

Free Vortex Wake (FVW) models solve the turbine wake in a time-accurate manner; this allows the vortices to convert, diffuse, and stretch. This model is based on a Lagrangian approach in which vortex filaments released from the blade are used, whereby the turbine wake is discretized into some Lagrangian markers, so the unsteady nature of the FOWT wake is modeled through shed vorticity. Blades are modeled using lifting lines or source/doublet panels in free vortex methods. As the prescribed load based on tabulated airfoil data is employed for the lifting lines, the model's accuracy is affected by input data. Unfortunately, the airfoil data are usually available just for static conditions, and corrections must be employed for modeling not resolved using this method [112].

In the case of modeling blades by means of panels, additional models are required to calculate the onset of the stall which makes the model able to consider these separations. Also,

the lifting line Free-Vortex Wake (FVW) approach is limited to predicting the aerodynamic loads in large surge movements when there is a dynamic stall. This is because the local flow around the blade profile is unavailable in this method.

Unsteady Reynolds-Averaged Navier–Stokes equations (URANS) have been comprehensively used to study wind turbine and wind-farm flows [113]. The fast growth in computational power leads to important progress in developing, validating, and applying turbulence-resolving CFD tools. Large-eddy simulation (LES) that is widely applied for wind turbine applications (e.g., see[113]) needs the parametrization of the smallest scales (sub-grid), whereas the larger and more energetic scales are explicitly resolved. This is unlike RANS and other reduced-order models (e.g., linearized Navier–Stokes solvers) that parametrize all scales of the turbulence [113]. Nevertheless, for complex turbulent flows, the results of LES are sensitive to the parameterization of subgrid-scale turbulent fluxes and subgrid-scale forces that include turbine-induced forces. Despite the high computational cost ($\sim 10^3-10^4$ CPU hours per simulation) and in the case of appropriate parametrizations, the accuracy of LES was shown to be high for simulating the turbulent boundary-layer flow around wind turbines and wind farms [113].

Pitch, surge, and other movements of floating offshore wind turbines can considerably affect the flow field around the blades. Considering this point, acquiring an accurate prediction of unsteady aerodynamic loads using the conventional form of BEM approaches is questionable. Tran and Kim [43], performed a CFD simulation to support this doubt. They used a dynamic mesh approach mesh for assessing the effects of periodic pitching motion of a FOWT. The effects of vortex–wake–blade interaction was investigated using three numerical methods, i.e., UBEM, FAST with BEM, and GDW (FAST's AeroDyn with the general dynamic wake modeling). The result could be compared to two different regions. In the case of only small pitching motion amplitude, i.e., in the range of 1–2°, the obtained predictions of the BEM model regarding produced power and thrust showed overall good agreement with CFD. On the other side, for a higher range of pitching motion amplitude, the BEM model produced results with lower accuracy than CFD, e.g., FAST-GDW showed a difference of 24% compared to CFD in power estimation at pitching motion amplitude of 4°. According to the authors, the conventional form of UBEM is not able to provide sufficiently flawless results in the case of pitching motions are significant.

1.3.1. Hybrid BET-CFD

In FOWTs, the pitch and other wind turbine movements can considerably affect the flow field around blades. Hence, an accurate prediction of unsteady aerodynamic loads calculated by the conventional form of BEM approaches is debatable for FOWT.

Even though simulation of the flow field is vital for capturing meaningful wake characteristics, experimental measurements, and fully blade-resolved CFD, either using URANS or hybrid URANS-LES are computationally expensive and often impossible to use in a multirotor wind farm. To overcome this shortcoming, hybrid analytical-computational models could reduce the computational cost order to help fill the knowledge gap about the flow field [114].

Recently novel approaches combined analytical and computational methods. CFD as a computational method solves the flow field, and the effect of the rotational turbine on the flow field is calculated using an analytical method such as Blade Element Theory (BET). Actuator Line (AL) or Actuator Disc (AD) are among the novel approaches that use CFD for flow field simulation. In these approaches, BET is used to calculate the loads on the flow, and then it can be applied using a source term in the momentum equation. The loads in the AD case are distributed over all the cells in the disc representing the turbine rotor, and for the AL, the loads are applied at the location of blade elements.

Actuator disk, actuator line, or blade element disk are among hybrid methods that introduce considerably higher physical fidelity compared to BEM. These methods are often referred to as “CFD-based computational-efficient” (CFD-CE) models; contrary to BEM methods, CFD-CE does not rely on BEM theory for calculating the induced-velocity field at the rotor disk. In these methods, flow velocities are incorporated from the flow solution provided by CFD. Among the mentioned CFD-CE models, the Actuator disk model is more straightforward in terms of set-up; nevertheless, it is not capable of considering swirl in the wake. The blade element disk approach can predict swirl, although the swirl effect is circumferentially averaged, and the method is not able to capture tip vortex formation [115]. Finally, the actuator line model provides the means to resolve the tip vortex and the corkscrew wake pattern. Accordingly, the AL model is by far one of the most promising approaches to accurately predict the wake behavior while maintaining a relatively cheaper computational effort compared to the blade-resolved approaches.

In the developed actuator line model by N. Troldborg et al. [116,117], a rotating line of momentum sources is utilized instead of each of the blades. Although the fundamental formulation of ALM is already disclosed, there are still some challenges in choosing its constitutional working parameters, such as the radius of the body-force projection function (ε), the grid spacing along the actuator line (Δ_{grid}), and the spacing between actuator points ($\Delta_{b)}$ which are of most critical ALM parameters.

There is no solid agreement on the projection function because, from one point of view, the radius should be as short as feasible to have a compact representation of force distribution along the blades. From the other point of view, the force-distributed region needs to be in proportion to the real region of force on the blade [118]. As suggested by Troldborg [118], $\varepsilon/\Delta_{grid}=2$ can be considered as a compromise between stability and accuracy. Regarding the parameter Δ_{grid}, 30 to 60 grid points along each actuator line and $\Delta_b \leq \Delta_{grid}$ were suggested to be considered. An ALM simulation performed by Martínez et al. [119], showed that their model was very sensitive to the Gaussian radius ε in a manner that increased this parameter directed to overprediction of power. A study by Jha et al. [120], showed that a constant Gaussian radius ε along the blade leads to overprediction of blade tip loads. A tip-loss function is required to deal with this problem, for instance, the Prandtl tip-loss factor [118] or the more advanced correction offered by Shen et al. [121]. Martínez-Tossas et al. [122], reformulated the filtered lifting line theory to utilize a kernel larger than the optimal value, which was advantageous in LES simulations.

Rocchio et al. [123], tried to calibrate the ALM parameters utilizing the data obtained from the immersed boundaries method to make their simulation practical for the turbulence wake downstream of a single fixed airfoil. It was showed a considerable boundary layer separation occurs for high angles of attacks, while ε/c was a function of the angle of attack, which could be incorporated by relating ε/c to C_D [124]. There are also some other studies devoted to defining appropriate parameters for ALM [125,126]. In a study by Martínez-Tossas et al. [127], they coupled actuator line and disk modeling with LES (Large-Eddy simulations); However, their model did not treat tip loss or downwash effects.

Creech et al. [128], employed the LES actuator line model to investigate the effect of support structures in a tidal turbine with contra-rotating rotors. It was shown that by disregarding support structures, the result of the numerical model is doubtful for the interrelated perspectives of turbine reliability, performance, and fluid dynamics.

A hydrofoil tip loss correction technique was introduced by Edmunds et al. [129]. By comparing their result against the IFREMER tidal turbine experiments [130], an improvement in the accuracy of the model was established. Wimshurst et al. [131] researched the application of the data from the 3D blade-resolved computations in correcting and modifying the spanwise loading correction factor in Shen et al.'s [132]tip loss functions. In a further study [133], the tip correction factor recalibrated individually in the axial and tangential directions for the MEXICO rotor data. Furthermore, they also employed blade-resolved computations to deliver a physical explanation of the tip-loss effect [134]. Also, in 2018, they contrasted the results of four LES codes with the implementation of ALM. The authors indicated the status of the inflow turbulence that should be considered and characterized based on the real field condition [135].

1.4 Summary and Status

Despite several benefits of the 3D blade-resolved computations in terms of accuracy, its computational cost is a barrier. While the published papers on ALM are mostly focused on fixed-bottom wind turbines, there is a lack of sources that investigate the capabilities of the ALM in the simulation of FOWTs. Given the above, the primary aim of the present work is to employ an ALM-CFD simulation to investigate the effects of the platform motions on the wake evolution as well as the aerodynamic performance of FOWTs. Since the ALM-CFD is not considered a high-fidelity method, this paper shows the abilities and limitations of this method that help researchers avoid the higher computational cost of blade-resolved CFD according to their needs. An Open FOAM library is developed to implement the ALM model in floating conditions.

2. Computational model

In this project, we implemented a methodology developed by Alireza Arabgolarcheh from the Industrial Engineering Department at the University of Padova to analyze the behavior of floating offshore wind turbines (FOWTs). Specifically, we used the actuator line model (ALM), a computational fluid dynamics (CFD) technique that represents turbine blades as actuator lines, to study how FOWTs interact with the wind and ocean environment. This approach allows for a detailed investigation of the aerodynamic forces and rotor wake effects that impact the performance and stability of these systems. To achieve this, the method developed a specialized C++ library within the OpenFOAM toolbox, which is designed for solving partial differential equations. The library utilizes a body forces technique in the flow solver to simulate the movement of solid turbine components. By analyzing lift and drag forces, we calculated the forces acting on various turbine parts such as blades, hub, and tower, all within a Cartesian framework linked to the rotor. We'll start by introducing the Actuator Line Model used to simulate body forces, followed by an explanation of the flow solver. Additionally, we'll discuss the methods employed to consider dynamic stall and tip vortex effects, and finally, we'll present the turbine model itself.

2.1 fvOptions

In recent years, there has been a significant increase in the use of Computational Fluid Dynamics (CFD) in various industries. More resources have been allocated to the development of different CFD software. However, a drawback is the considerable investment of time and money required for the redevelopment of these software codes. OpenFOAM, being one of the most popular open-source CFD software, has the potential to streamline the development process. This study focuses on integrating the Actuator Line Model (ALM) into OpenFOAM

by creating necessary libraries. OpenFOAM includes a feature called fvOptions, which allows for the addition of various source terms to equations during runtime without altering the source code. Figure 16 illustrates the flowchart for coupling these components: the left side represents functionalities handled by existing OpenFOAM libraries, while the right side depicts the main functions developed in this project. The coupling between these components is facilitated through the fvOptions framework.

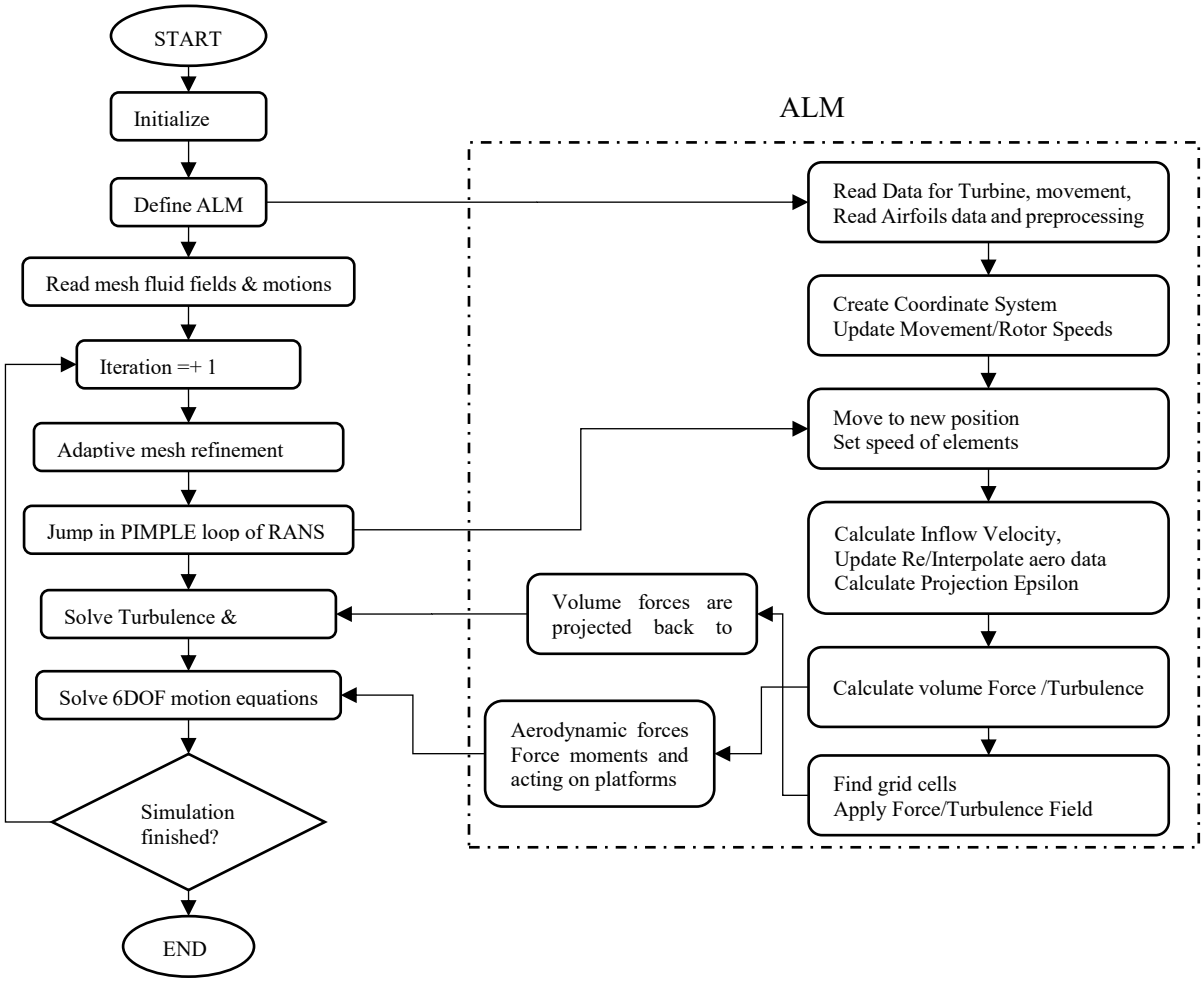

Figure 16. Flowchart for coupling the OpenFOAM solver with the developed ALM libraries [136]

Many CFD applications include equation structures that should be manipulated at run time using user-specified finite volume options, given by the shorthand fvOptions. The fvOptions is a framework introduced to allow selecting any physics that can be represented as sources or constraints on the governing equations, e.g., porous media, MRF, and body forces. Figure 17 shows how it provides additional source/sink terms or enforces constraints for the momentum equation. All other transport equations, including turbulence equations, can be modified

similarly. Hence, the developed code provides the source term to be injected into the OpenFOAM source through the fvOptions framework.

```
// Solve the Momentum equation
MRF.correctBoundaryVelocity(U);
tmp<fvVectorMatrix> tUEqn
(
    fvm::ddt(U) + fvm::div(phi, U)
  + MRF.DDt(U)
  + turbulence->divDevReff(U)
 ==
    fvOptions(U)
);

fvVectorMatrix& UEqn = tUEqn.ref();
UEqn.relax();
fvOptions.constrain(UEqn);

if (pimple.momentumPredictor())
{
    solve(UEqn == -fvc::grad(p));
    fvOptions.correct(U);
}
```

Figure 17. A part of the OpenFOAM solver code that includes fvOptions [136,137]

2.2 Actuator Line Model (ALM)

The fundamental philosophy of the actuator Line methodology is to substitute the physical geometry of the blades with only its impact on the flow field. The ALM uses a chain of spanwise element points in place of sections, each with a constant airfoil, twist, chord, and oncoming wind. The volumetric forces made by each blade section are projected into the flow field, whereby it inserts the same forces on the fluid as the turbine blades through source terms in the momentum equations. The aerodynamic forces of blades are calculated based on lift and drag coefficients that are usually obtained from tabulated airfoil data. These forces are formulated as follows:

$$F_l = \frac{1}{2} C_l(\alpha) \rho \left|\vec{U}_{rel}\right|^2 cw\hat{e}_l \tag{1}$$

$$F_d = \frac{1}{2} C_d(\alpha) \rho \left|\vec{U}_{rel}\right|^2 cw\hat{e}_d \tag{2}$$

Here α denotes the local angle of attack measured as the angle between the chord and the local relative flow, C_l is the lift coefficient, C_d is the drag coefficient that is obtained from tabulated

airfoil data. The lift and drag coefficients can be interpolated linearly for the local Reynolds number. Here, $\vec{U}_{rel}$ indicates the relative velocity, resulting from inflow velocity ($\vec{U}_i$) and the element velocity ($\vec{U}_e$). The rotation of the rotor and the motion of the platform are involved in the element velocity.

$$\vec{U}_{rel} = \vec{U}_i + \vec{U}_e + \vec{U}_{platform} \tag{3}$$

$$\vec{U}_e = \vec{U}_{rotor\,rotation} + \vec{U}_{platform} \tag{4}$$

The inflow velocity was sampled at the element point (i.e., the applied Gaussian force center) in the early forms of actuator line modeling. Nonetheless, such Gaussian forces could create a bound vortex around the actuator line element point as the vortex center was on the actuator line. In case the velocity is sampled at the element point, the inflow velocity might not be influenced by the vortex-induced vorticity [138]. Some studies, including Mittal et al. [139] and Churchfield et al. [138], proposed that the location of velocity sampling should be moved ahead of the actuator line. In the current project, to address the problem of uncertain velocity sampling location, the inflow velocity ($\vec{U}_i$) was averaged over a series of sampling points in the identical spanwise section with a sampling radius away from the element point. Hence, a total number of 16 sampling points were determined at a distance equal to $2\Delta x_{grid}$ from the location of elements to interpolate from the velocity field resolved by CFD.

In ALM, forces are inserted along a one-dimensional line. In this regard, the most straightforward way is to apply the forces in only cells through which the actuator line passes. Nevertheless, making such sharp input steps of force can generate numerical instability. Furthermore, given that the actual forces generated by airfoils are not focused on a point and spread over the surface, the previous approach is not physically realistic.

Once the lift and drag forces are calculated, the total force in the radial direction $R_n(r)$ is obtained by resolving the forces in the plane of a rotor:

$$R_n(r) = F_l(r)\cos\big(\alpha(r)\big) - F_d(r)\sin\big(\alpha(r)\big) \tag{5}$$

This formula combines the contributions of both lift and drag forces projecting them onto the plane of the rotor where $\alpha(r)$ is the local angle of attack at the blade element.

A 3D isotropic Gaussian function for force projection was proposed by Sørensen and Shen[140]. Based on their suggestion, the aerodynamic forces are calculated and then smoothly projected onto the flow field using a Gaussian function as follows:

$$\boldsymbol{F}_{field}(x_c, y_c, z_c, t) = -\sum_N \sum_e \vec{F}_{N,e}(x_{N,e}, y_{N,e}, z_{N,e}, t) f_{tip} \eta_{N,e} \tag{6}$$

$$\eta = \frac{1}{\varepsilon^3 \pi^{3/2}} \exp[-({}^{r}/_{\varepsilon})^2] \tag{7}$$

where $\boldsymbol{F}_{field}$ is the volumetric force field at the position of the cells, f_{tip} is tip correction function, and $\vec{F}$ indicates the forces at actuator element points that are calculated based on lift and drag forces. Also, N is the body index (i.e., blades, hub, and tower), and e denotes the actuator element point index.

The Gaussian function is represented by η, while ε is the projection width, and r is a distance from the actuator point to the grid cell center where the force projection is applied. The parameter $\boldsymbol{F}_{field}$ should be added as the source term into the momentum equation through $S_{fvOptions}$ whereby the spread sectional force of each element is implemented using the Gaussian distribution as additional body force at each cell. Deciding on the width of the Gaussian function is still an area that requires to be studied more. In this regard, some research has been performed that included research by Churchfield et al. [138]. From one point of view, as ε becomes smaller, the actuator line resembles a line and the results approach reality, on the other side it must be large enough compared to the grids to preserve numerical stability. Besides, it is known that a blade conforming to $\varepsilon/c =$ constant yields improved results. In the current model, the width of the Gaussian function is controlled by ε as the following:

$$\varepsilon_l = \frac{c}{4} \tag{8}$$

$$\varepsilon_d = \frac{cC_d}{2} \tag{9}$$

$$\varepsilon_g = 4\sqrt[3]{V_{cell}} \tag{10}$$

$$\varepsilon = \max[\varepsilon_l, \varepsilon_d, \varepsilon_g] \tag{11}$$

Utilizing a Gaussian function leads to having a negligible value even at far distances. The maximum value of r in Eq. (7) that is the radius of the projection sphere is limited, and its maximum is calculated as follows:

$$r_{max} = \varepsilon \sqrt{\log \frac{1}{0.001}} + c \tag{12}$$

Consequently, the modification of force field is only accomplished for cells inside the projection sphere. This approach is a practical technique in order to decrease the computational cost.

It is known that while approaching the tip of the blades, the averaged induced velocity between two vortex sheets should tend to zero exponentially. In other words, the flow shows the tip effect caused by the pressure equalization from the suction and pressure sides in the blade tip cross-section. Furthermore, there are rotational effects that are due to Coriolis and centrifugal forces, particularly for cross-sections near the blade root. Hence a modification is necessary to take these effects into account and f_{tip} function is applied to the 2D airfoil's lift and drag coefficients.

$$f_{tip} = \frac{2}{\pi} arccos\left[exp\left(-g \frac{B\,(R\,-\,r)}{2\,r\ sin(\alpha + \beta)}\right)\right] \tag{13}$$

Here β is pitch angle that includes blade pitch and twist. The g coefficient depends on different parameters such as the number of blades, TSR (λ), and chord distribution. For simplicity, the function is chosen to be only dependent on the variable $B\lambda$ as follows:

$$g = exp\,[-C_1\,(B\lambda\,-\,C_2)] + 0.1 \tag{14}$$

Coefficients $C_1$and C_2 were determined empirically using data at two different tip speed ratios (NREL rotor at 10 m/s and WG 500 rotor at TSR=14). The function is shifted with a minor value of 0.1 to be consistent for infinite tip speed ratio cases or an infinite number of blades. The final form uses $C_1$and C_2 whose values are 0.125 and 21, respectively. Function g is needed to adjust the influence of the tip vortices on pressure distribution in the blade tip region.

The determination of the linear and angular velocity vector can be achieved using either a prescribed movement or the acting forces and moments on the turbine. Likewise, the position and orientation of the rotating center need to be determined. Subsequently, all elements are updated at each time step as follows:

$$\vec{x}_{r.c.}^{\,n+1} = \vec{x}_{r.c.}^{\,n} + \vec{v}_{r.c.}\Delta t \tag{15}$$

$$\vec{\theta}_{r.c.}^{n+1} = \vec{\theta}_{r.c.}^{n} + \vec{\Omega}_{r.c.}^{n} \Delta t \tag{16}$$

here $\vec{x}_{r.c.}$ is the position of the rotating center of the floating wind turbine structure, and its orientation is denoted by $\vec{\theta}_{r.c.}$. In this equation, $\vec{v}_{r.c.}$ and $\vec{\Omega}_{r.c.}$ denote the instantaneous linear and angular velocities of the whole turbine structure around the rotating center, respectively. When the position of the new-calculated rotation center is determined, the elements position and orientation are updated utilizing a rotation matrix from axis-angle representation. Vector $\vec{X}_e^n$ in Figure 12 represents the current element position relative to the rotating center. The rotation of $\vec{X}_e^n$ for a finite rotation angle of $\Delta\theta = |\vec{\Omega}|\Delta t$ around the axis of $\vec{\Omega}$ is expressed by the following equation:

$$\vec{x}_e^{n+1} = \vec{x}_e^n + \Delta\vec{x} \tag{17}$$

$$\Delta\vec{x} = |\vec{x}_e^n - \vec{x}_{r.c.}|[(\cos(\Delta\theta) - 1)\hat{e}_r + \sin(\Delta\theta)\,\hat{e}_\theta] \tag{18}$$

The unit vectors $\hat{e}_r$ and $\hat{e}_\theta$ are defined as:

$$\hat{e}_\theta = \frac{\vec{\Omega}_{r.c.} \times \vec{x}_e}{|\vec{\Omega}_{r.c.} \times \vec{x}_e|} \qquad \hat{e}_r = \frac{\hat{e}_\theta \times \vec{\Omega}_{r.c.}}{|\hat{e}_\theta \times \vec{\Omega}_{r.c.}|} \tag{19}$$

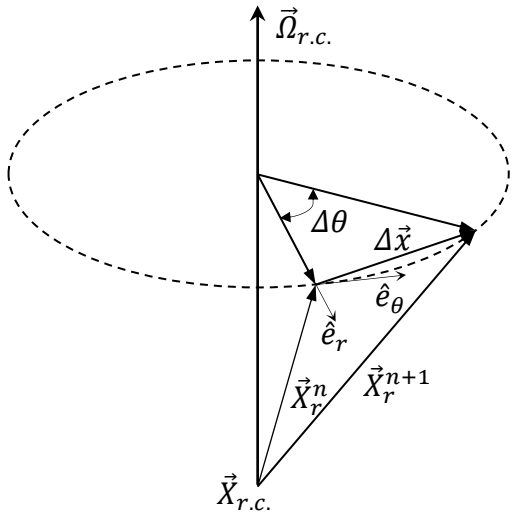

Figure 18. Solid-body rotation coordinates [137]

The rotation is applied using $R(\varphi, u)$ rotation matrix that is introduced in Eq. (20). The shorthand notations of $S_\xi = \sin\varphi$, $C_\xi = cos\varphi$ and $V_\xi = 1 - \cos\varphi$, are applied.

$$R(\varphi,u)=\begin{bmatrix} C_\xi+u_x^2V_\xi & u_xu_yV_\xi-u_zS_\xi & u_xu_zV_\xi+u_yS_\xi \\ u_yu_xV_\xi+u_zS_\xi & C_\xi+u_y^2V_\xi & u_yu_zV_\xi-u_xS_\xi \\ u_zu_xV_\xi-u_yS_\xi & u_zu_yV_\xi+u_xS_\xi & C_\xi+u_z^2V_\xi \end{bmatrix} \tag{20}$$

The same procedure is applied for all other vectors that need to be rotated, e.g., $\vec{\omega}$. Along with rotations, the translation of elements is achieved just after updating the rotation center, which can be expressed as:

$$\vec{x}_e^{n+1}=\vec{x}_e^{n}+\vec{v}_{r.c.}\Delta t \tag{21}$$

2.3 Definitions

The non-dimensional parameters of the tip speed ratio (λ), power coefficient (C_P), and thrust coefficient (C_T) are defined as the following equations:

$$\lambda=\omega R/U_\infty \tag{22}$$

$$C_P=\frac{P}{\frac{1}{2}\rho U_\infty^3 A}=\frac{\sum_N\sum_e \omega r\delta F_t}{\frac{1}{2}\rho U_\infty^3 A} \tag{23}$$

$$C_T=\frac{F_a}{\frac{1}{2}\rho U_\infty^2 A}=\frac{\sum_N\sum_e \delta F_a}{\frac{1}{2}\rho U_\infty^2 A} \tag{24}$$

where A is the rotor swept area, P denotes the produced power from the product of the radius and the tangential force (rF_t), and F_a is the axial force acting on the rotor.

2.4 Governing equations

The finite volume method (FVM) was employed to compute the turbulent flow field around the wind turbine. The three-dimensional Reynolds-averaged Navier–Stokes equations (RANS) are formulated as follows [141]:

$$\frac{\partial\rho}{\partial t}+\frac{\partial}{\partial x_i}(\rho u_i)=0 \tag{25}$$

$$\frac{\partial}{\partial t}(\rho u_i)+\frac{\partial}{\partial x_j}(\rho u_iu_j)=-\frac{\partial p}{\partial x_i}+\frac{\partial}{\partial x_j}\left[\mu\left(\frac{\partial u_i}{\partial x_j}+\frac{\partial u_j}{\partial x_i}-\frac{2}{3}\delta_{ij}\frac{\partial}{\partial x_j}\right)\right]+\frac{\partial}{\partial x_j}\left[-\rho\overline{\acute{u}_i\acute{u}_j}\right]+ \tag{26}$$

$S_k+S_{\text{fvOptions}}$

The Reynolds stress term ($-\rho\overline{\acute{u}_\iota\acute{u}_J}$) was modeled based on the Boussinesq hypothesis according to Eq. (27), whereby the Reynolds stresses are concerned with the mean velocity gradients.

$$-\rho\overline{\acute{u}_\iota\acute{u}_J} = \mu_t\left(\frac{\partial u_i}{\partial x_j}+\frac{\partial u_j}{\partial x_i}\right)-\frac{2}{3}\left(\rho k+\mu_t\frac{\partial u_k}{\partial x_k}\right)\delta_{ij} \tag{27}$$

$$\mu_t = \rho\nu_t = \rho C_\mu\frac{k^2}{\epsilon}$$

The URANS approach is widely used to study wind turbine and wind-farm flows [142,143]. While LES can deliver more reliable results, it involves finer mesh and computational costs [142]. Given that the main idea behind utilizing of ALM in this project is decreasing computational cost, the commonly used high Reynolds number model of $k-\epsilon$ realizable with its standard turbulent constants [144] was chosen. It is noteworthy because there is no solid part while using ALM, the simulation of boundary layer and accurate prediction of the transition onset on blades is not required [145].

Compared to the standard model, the realizable model includes an alternative formulation for the turbulent viscosity. Moreover, a modified transport equation for the dissipation rate has been derived from an exact equation for the transport of the mean-square vorticity fluctuation. The realizable model has shown substantial improvements over the standard model in the existence of strong streamline curvature, vortices, and rotation. In computational domains that contain both rotating and stationary fluid zones (for example, multiple reference frames, rotating sliding meshes), this model might produce non-physical turbulent viscosities. However, in ALM, there is just one stationary fluid zone. Transport equations for ϵ and k are [146]:

$$\frac{D}{Dt}(\rho k) = \nabla\cdot(\rho\, D_k\nabla k)+\rho\, G-\frac{2}{3}\rho(\nabla\cdot\,\boldsymbol{u})k-\rho\epsilon+S_k+S_{\text{fvOptions}} \tag{28}$$

$$\frac{D}{Dt}(\rho\epsilon) = \nabla\cdot(\rho\, D_\epsilon\nabla\,\epsilon)+C_1\rho|\boldsymbol{S}|\epsilon-C_2\rho\frac{\epsilon^2}{k+(\nu\epsilon)^{0.5}}+S_\epsilon+S_{\text{fvOptions}} \tag{29}$$

In sum, The finite-volume method was utilized for solving the governing equations. The incompressible flow approximation was assumed since the concerned Mach number values remained below 0.1 (conventionally, a Mach number below 0.3 stands for incompressible

flow). A second-order Crank–Nicolson method was applied for time integration for the temporal discretization.

Terms $S_{\text{fvOptions}}$ in momentum, turbulent kinetic energy, and turbulent kinetic energy dissipation rate equations are calculated by the developed ALM C++ library. The PIMPLE algorithm was employed for pressure-velocity coupling. This algorithm is a combination of SIMPLE and PISO algorithms. The matrices are solved by selecting the generalized geometric-algebraic multigrid (GAMG) for pressure and a preconditioned bi-conjugated gradient (PBiCG) for velocity [141].

2.5 Geometric model

This study aimed to adapt the actuator line model (ALM) introduced by Troldborg et al.[117] for broader applications and to eliminate sensitivity issues related to different cases. To ensure the current code was accurate, it was tested on fixed-bottom turbines, which avoid the complications of platform movement and other interferences. Two different test scenarios were examined. The accuracy of the ALM relies heavily on reliable input data, so the NREL Phase VI, known for its comprehensive data, was chosen for this purpose. Additionally, the NREL 5-MW turbine, representing a larger wind turbine, was also included in the study.

The National Renewable Energy Laboratory (NREL) Phase VI reference wind turbine was modeled based on the test sequence S settings represented in reference [147]. In this sequence, an upwind, rigid turbine with a 0° cone angle was utilized, and the test was applied for wind speed, ranging from 5 m/s to 25 m/s. This case is based on a constant speed, constant pitch, and stall-regulated wind turbine. The rotor is a two-bladed rotor with twisted, tapered blades and shaped based on the S809 airfoil [148,149]. The main characteristics of the turbine are summarized in Table 1. The chord and twist distributions are demonstrated in Figure 19.

Table 2. The NREL Phase VI technical data and sequence S settings [22].

Parameter	*Value*	*Parameter*	*Value*
Rotor configuration	Upwind	Rotating angular velocity	71.63 [rpm]
Number of blades	2	Tip pitch angle	3 [°]
Rotor radius	5.029 [m]	Air density	1.23 [kg/m^3]
Hub height	12.2 [m]	Air kinematic viscosity	1.46e-5 [m^2/s]
Cone angle	0 [°]	Blade sectional profiles	S809

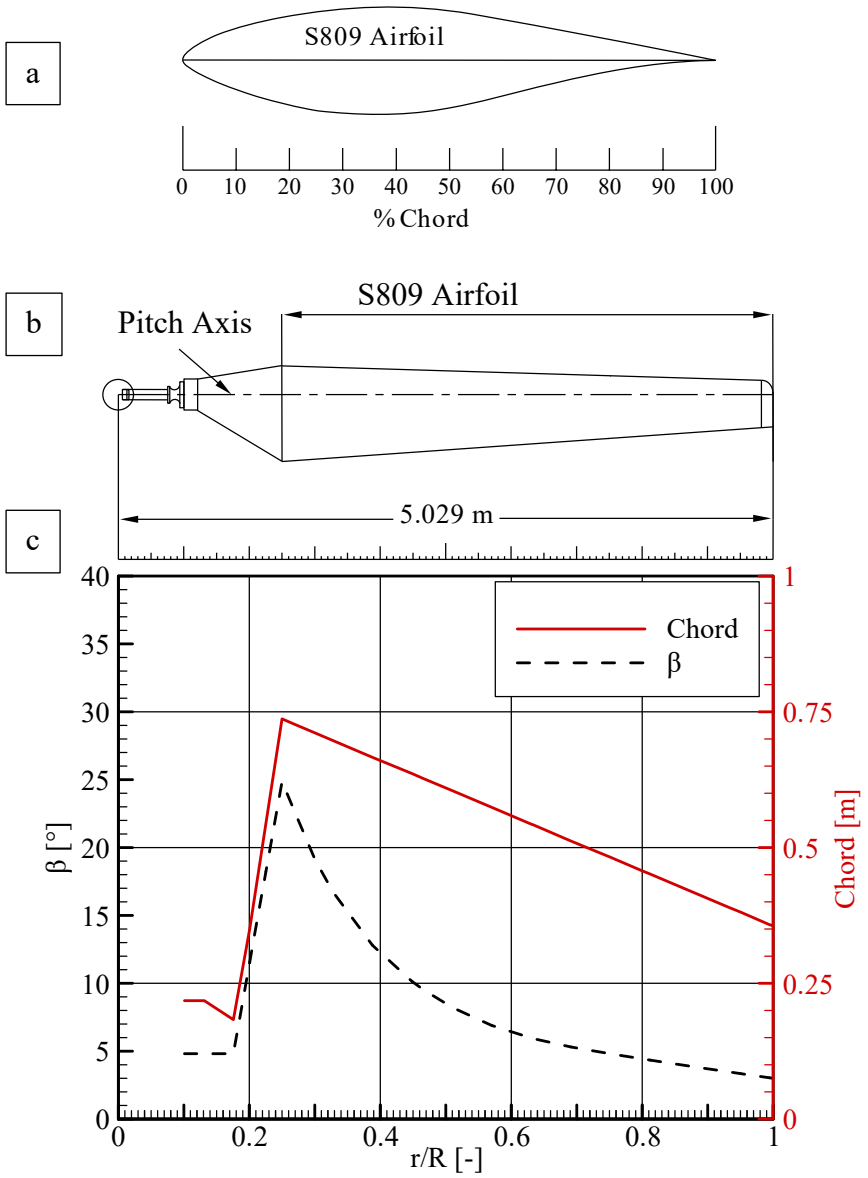

Figure 19. Representations of the blade. (a) S809 airfoil shape. (b) blade shape. (c) Spanwise distributions for twist and chord of the NREL Phase VI blade [147].

The NREL 5-MW wind turbine was designed by the National Renewable Energy Laboratory to be a representative utility-scale wind turbine suitable for a floating offshore installation. This is a conventional three-blade upwind turbine with a rotor diameter of about 126 m and a hub height of nearly 90 m. The blades are composed of a series of Delft University (DU) and NACA 64xxx airfoils, as shown in Figure 20 and Table 3. This turbine is designed as a variable-speed variable-blade-pitch-to-feather-controlled turbine. The rated wind speed is 11.4 m/s, and under the rated wind speed, the rotor speed is 12.1 rpm, and the produced power is 5 MW.

Table 3. Blade data for the NREL 5MW reference turbine

Radius [m]	*Chord [m]*	*Twist [°]*	*Axial Distance [m]*	*Azimuth Distance [m]*	*Air foil*
1.5	3.542	13.308	0.000E+00	0.000E+00	Cylinder1
2.8667	3.542	13.308	8.153E-04	3.447E-03	Cylinder1
5.6	3.854	13.308	2.484E-02	1.050E-01	Cylinder1
8.3333	4.167	13.308	5.947E-02	2.514E-01	Cylinder2
11.75	4.557	13.308	1.091E-01	4.612E-01	DU40_A17
15.85	4.652	11.48	1.157E-01	5.699E-01	DU35_A17
19.95	4.458	10.162	9.832E-02	5.485E-01	DU35_A17
24.05	4.249	9.011	8.319E-02	5.246E-01	DU30_A17
28.15	4.007	7.795	6.793E-02	4.962E-01	DU25_A17
32.25	3.748	6.544	5.339E-02	4.654E-01	DU25_A17
36.35	3.502	5.361	4.090E-02	4.358E-01	DU21_A17
40.45	3.256	4.188	2.972E-02	4.059E-01	DU21_A17
44.55	3.01	3.125	2.051E-02	3.757E-01	NACA64_A17
48.65	2.764	2.319	1.398E-02	3.452E-01	NACA64_A17
52.75	2.518	1.526	8.382E-03	3.146E-01	NACA64_A17
56.1667	2.313	0.863	4.355E-03	2.891E-01	NACA64_A17
58.9	2.086	0.37	1.684E-03	2.607E-01	NACA64_A17
61.6333	1.419	0.106	3.282E-04	1.774E-01	NACA64_A17
63	0.5	0	3.282E-04	1.774E-01	NACA64_A17

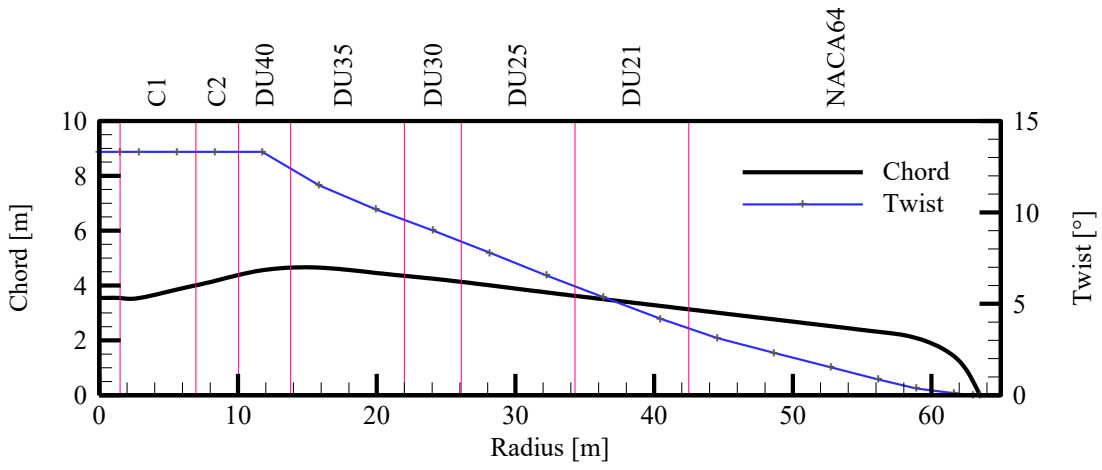

Figure 20. NREL 5 MW Chord and twist design [136]

Table 4 shows the NREL 5MW wind turbine properties and the rotational speed and tip pitch angles used for the NREL5MW baseline are listed in Table 5.

Table 4. Properties of NREL 5MW wind turbine

Parameter	*Value*	*Parameter*	*Value*
Rotor configuration	Upwind	Power Output	5 MW
Number of blades	3	Cut-in wind speed	3 m/s
Rotor diameter	126 [m]	Rated wind speed	11.4 m/s
Hub height	90 [m]	Cut out wind speed	25 m/s
Rotor Mass	53220 kg	Rated Tip Speed	80 m/s
Air density	1.23 [kg/m^3]	Cut-in rotor speed	6.9 rpm
Air kinematic viscosity	1.46e-5 [m^2/s]	Rated rotor speed	12.1 rpm
Blade sectional profiles	DU and NACA series	Overhang—Shaft Tilt—Precone	5[m]—5°—2.5°

Table 5. Simulation condition for NREL 5MW baseline

Wind Speed [m/s]	*Rotor Speed [rpm]*	*Tip speed ratio [-]*	*Tip pitch angle [°]*
6	7.92	8.71	0
8	9.16	7.55	0
11.2	12.1	7.1275	0
15	12.1	5.32	10.45
20	12.1	3.99	17.47
25	12.1	3.19	23.47

3. Validation and Verification

3.1 Computational Domain and Boundary Conditions

The computational domain in this study is in a Cartesian coordinate system. The cuboid computational domain consists of non-conformal hexahedral (cubic) grids for three rotors in triangular configuration from a top-down view shown in Figure 21 in a specific configuration (T00) which they are placed at each vortex, the upstream one (rotor A) in T00 configuration is perfectly align and positioned over the rotor C and for this specific configuration the wake of rotor B is not effecting on downstream rotor (rotor C). Generally, this type of mesh makes local refinement possible in the areas of interest that can significantly reduce the computational resources required for the simulation, also we considered the fixed structure for turbines regardless of structure motion, but as this configuration is just used in offshore windfarms, we refer it as an offshore platform, considering the wind direction along the x-axis. The boundary conditions for the wind turbine simulation are expressed in Figure 22-a. A uniform freestream velocity boundary was applied for the inlet condition. The inlet velocity magnitude was set to the examined velocity at the NREL experiment [150], and the direction was set in the X-direction. A pressure outlet boundary condition was set for the outlet condition, and the reference pressure was considered the standard atmospheric pressure. Consequently, the dynamic pressure field is determined considering this condition. The no-slip boundary conditions were applied for the two lateral walls, the base and the upper side of the domain.

The multi-view representation as shown in Figure 22 can ensure the accurate simulation of the aerodynamic forces, wake interactions, and overall rotor performance. Subfigure (a) provides a 3D view of the computational domain, highlighting the boundary conditions essential for simulating the airflow around the rotors. Subfigure (b) shows the front view of the computational grid, where the rotor cross-section is located, illustrating the grid's resolution necessary for capturing rotor-induced flow disturbances. Subfigure (c) presents the side view

along the tower axis, emphasizing the vertical grid refinement needed to capture the interactions between the turbine tower and the airflow.

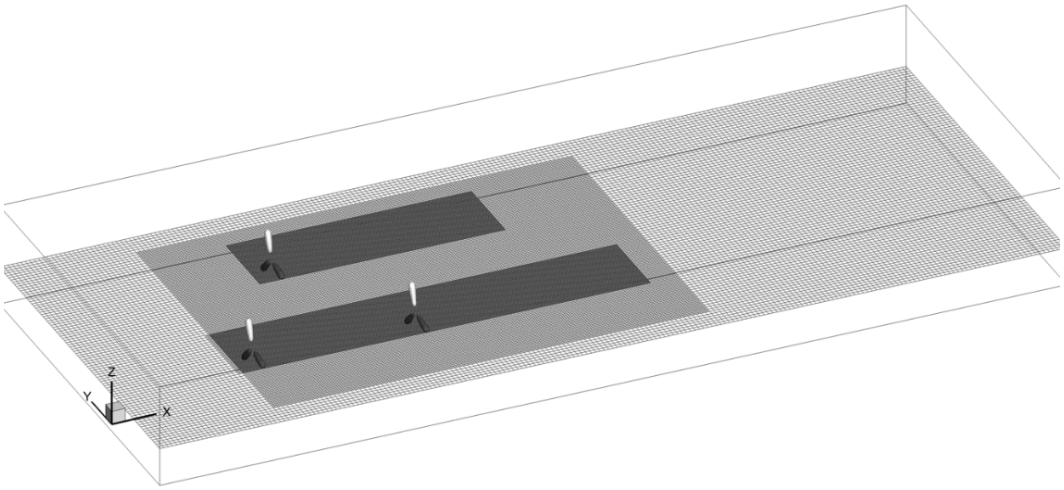

Figure 21. The computational grid for three turbines in a triangular configuration from the top-down view

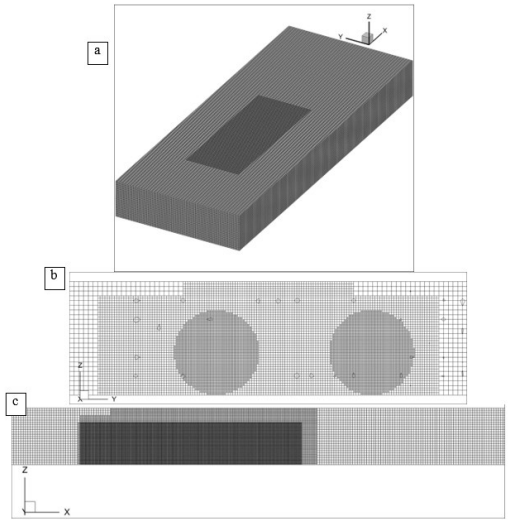

Figure 22. (a) A schematic view for computational domain and boundary conditions. (b) The computational grid from the front view, the section is on the rotor. (c) The computational grid from the side view, the section is one the tower axis.

The verification examinations for domain size, mesh resolution, and time step size are described in the following for the NREL Phase VI case at a wind speed of 7 m/s and tip speed ratio (TSR) of 5.4. Prior to any data sampling, the number of time steps necessary for a converged solution was revealed.

3.2 Averaged power coefficient

In Figure 23, the time history of the power coefficient (C_P) and power coefficient change relative to the last rotor revolution ($\Delta C_P / C_{(P,30)}$) were plotted for the first 30 revolutions of the rotor on normal and logarithmic scales of revolutions, respectively. Following 20 revolutions, the difference between two consecutive revolutions was less than 0.3% and the value of ΔC_P declined below 1%. Instantaneous values presented in this work correspond to the last revolution (revolution 20), while average values were calculated over the last five revolutions.

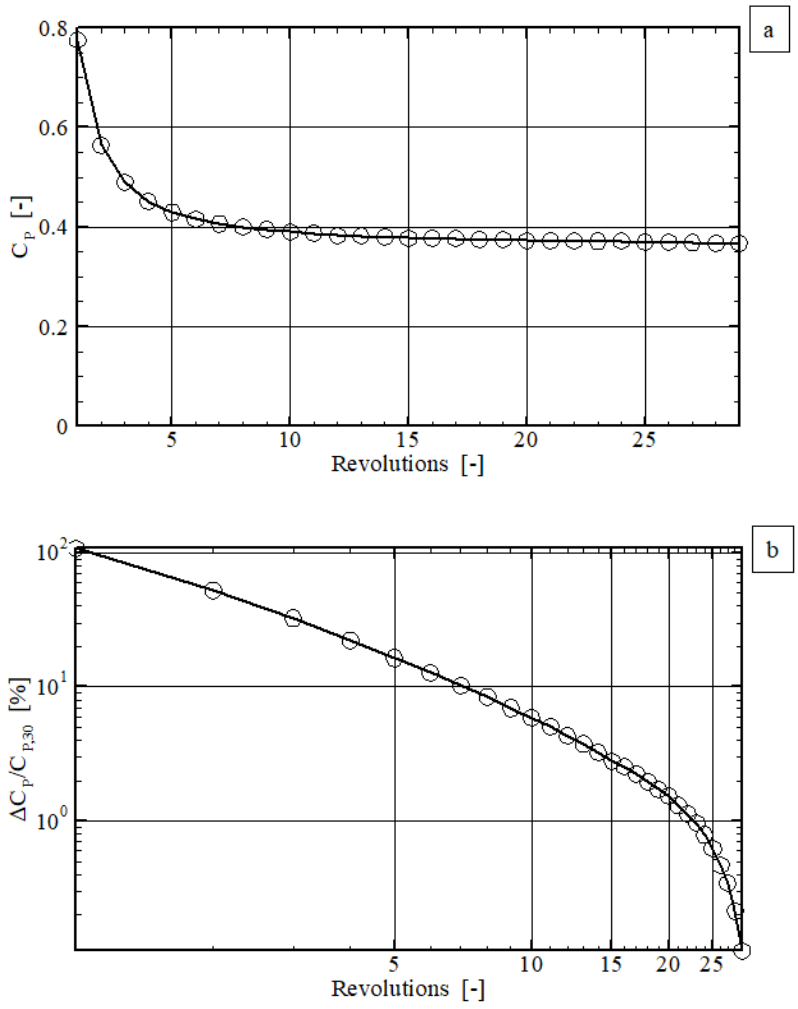

Figure 23. History of averaged power coefficient (a) and its change relative to the last revolution of the turbine on log-scale (b) vs. the number of revolutions.

3.3 Sensitivity Study of Domain Size

The study of NREL Phase VI was simulated by considering a domain that is geometrically like the wind tunnel used in reference [150]. Accordingly, the height and width of the domain

section were set to 36.6m and 24.4m. Due to the selected outlet boundary condition and inlet boundary condition, the impact of upwind and downwind distances (d_i, d_o) on the produced power of wind turbines was investigated as described in Table 6. This assessment was carried out at a wind speed equal to 7m/s. The domain length was extended according to Table 6, and the mesh size was kept the same. The data were compared with the most extended domain (case 7). The results showed that for cases longer than case 1, the difference was less than 0.1%. A compromise was achieved between accuracy and computational cost, and therefore case 2 was selected for this study.

Table 6. Test matrix for the sensitivity study of the domain size

Case #	*Distance to the inlet* d_i	*Distance to the outlet* d_o	*Domain Size* $W \times H \times L$	*# Cells*	C_P/C_{P-ref}
1	1.5	7.5	79	395k	1.0140
2	2.5	7.5	88	400	1.0033
3	4.5	7.5	106	409k	1.0021
4	8.5	7.5	141	427k	1.0014
5	2.5	5	66	389k	1.0139
6	2.5	9	102	407k	1.0031
7	8.5	9	154	434k	1.0000

Accordingly, a cuboid of (10×3×4) D was used as the computational domain to simulate the NREL Phase VI wind turbine.

3.4 Grid Sensitivity Analysis

Grid sensitivity analysis was organized in two phases. Firstly, the mesh size near the blades was examined. Figure 24 demonstrates the size of the most refined grid near the elements (ΔX). It is clear from this plot that the size of grids should be less than 0.25 m in the blade region while coarser grids cause an unacceptable error or simulation failure. As the idea behind the ALM is reducing the computational cost compared to blade-resolved CFD approaches, a second analysis was accomplished to assess the effect of grid size in areas far from the blades. The computational domain was divided into four zones to have coarser grids in the far region, as shown in Figure 22-c. The examined configurations are listed in Table 7. Based on this plot, case D with underlined data was chosen as the optimum case, consisting of around 400,000 cells.

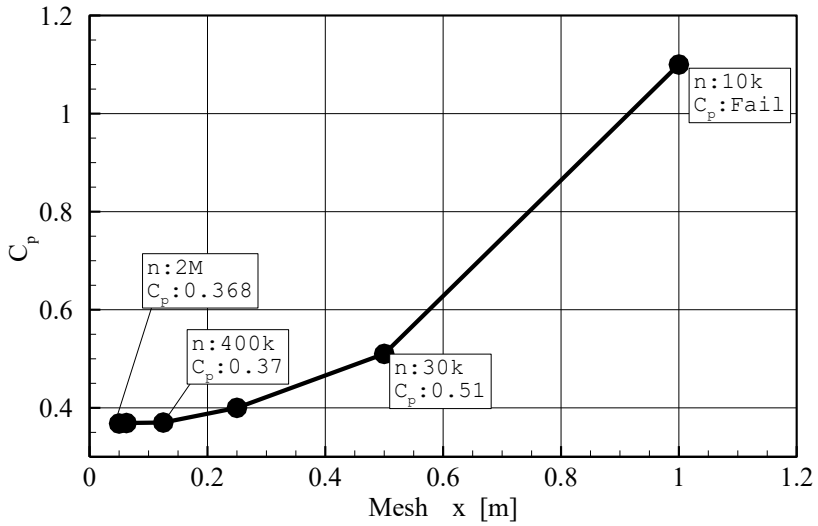

Figure 24. Mesh independence study near the blades, n is the total number of cells.

Table 7. Mesh independence study for mesh size [m] in each region

Case#	*Region 1 (outer)*	*Region 2 (Wake)*	*Region 3 (turbine)*	*Region 4 (rotor)*	C_p
A	1	1	1	1	fail
B	1	1	0.5	0.25	0.44
C	1	0.5	25	0.25	0.45
D	**1**	**0.5**	**0.25**	**0.125**	**0.37**
E	1	0.25	0.125	0.125	0.37
F	0.5	0.5	0.125	0.05	0.368

The effect of time step size on the produced power coefficient (C_P) was also assessed. The results of the assessment are presented in Table 8. To increase the reliability of the assessment and to avoid the missing phenomenon that occurs in short periods, the data are obtained for cases with 0° and 30° of yaw angles. This helps to ensure involving phenomenon associated with rotor misalignment. The shortest time step with a value of $\Delta\theta$ = 0.216° was considered as the reference case. Hence the subscript "ref" refers to case 1. To make data comparable, the ratio of C_P/C_{P-ref} is plotted in Figure 25. Figure 25 indicates that for time steps smaller than $\Delta\theta$= 0.432°, there was a difference of less than 2% in C_P compared to the smallest time step that investigated [151].

Table 8. Test matrix for the study of $\Delta\theta$. All sizes are given in turbine diameters (D).

Case #	$\Delta\theta$ *[°]*	*Time steps per revolution [-]*	Δt *[s]*	d_i *[-]*	d_o *[-]*	*Domain Size [-]* $W \times H \times L$
1	0.216	1667	0.0005	2	8	88
2	0.432	833	0.001	2	8	88
3	0.864	417	0.002	2	8	88
4	1.728	208	0.004	2	8	88
5	3.456	104	0.008	2	8	88
6	6.912	52	0.016	2	8	88
7	13.824	26	0.032	2	8	88

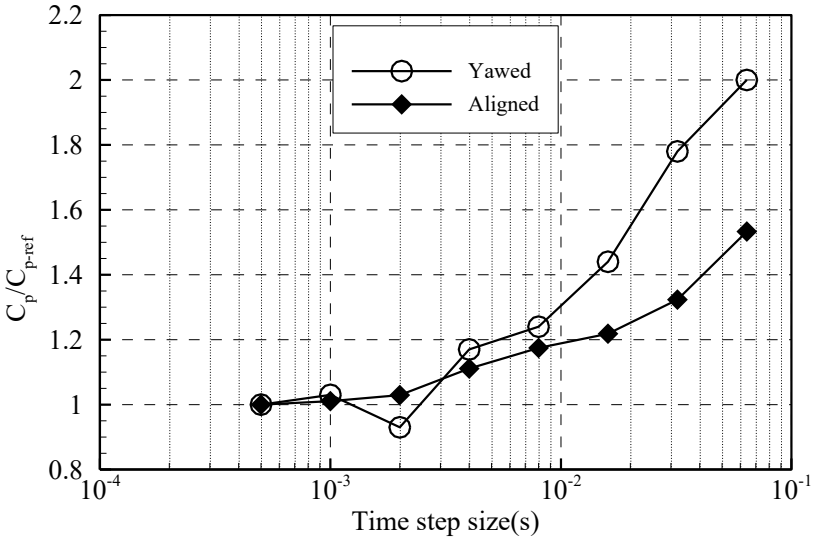

Figure 25. Cp independence study for time steps per revolution [151]

3.5 Validation

Once the independence of results from the numerical factors was verified, the results of the current code were validated against other methods that are available in the literature. As mentioned before, the reason behind choosing the NREL Phase VI test case was the availability of adequate experimental data. Hence, the ALM result for this case is compared with the NREL experimental data [147] in Figure 26. The power coefficient (C_p) is represented against TSR and the output rotor torque is reported as a function of wind speed to have a better illustration in both high and low TSR regions. Evaluating the power coefficient showed a good general agreement with experimental measurements; likewise, the computed aerodynamic torque was consistent with the experimental data at the tested wind speeds.

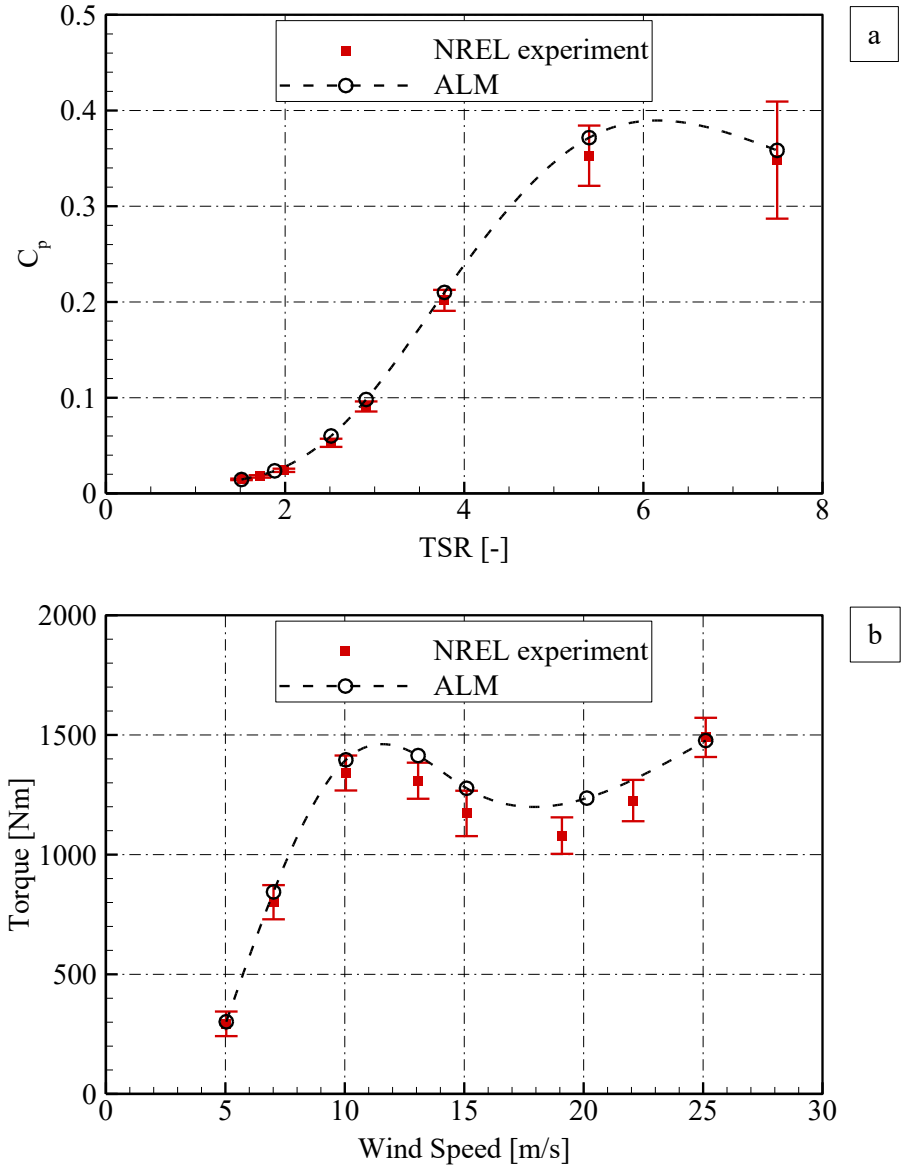

Figure 26. Comparison of ALM results of NREL Phase VI wind turbine with experimental data [147]. a) Power coefficient for TSR of the bottom-fixed wind turbine; b) torque out for the investigated wind speeds.

The large-size wind turbine, NREL 5-MW case, is studied in Figure 27. This figure assesses the capability of the current ALM code in the simulation of large-size offshore wind turbines. The same procedure was accomplished for mesh and time step size verification. Because the experimental data for this wind turbine are not available, the results were validated with several methods, including the BEM results obtained using the FAST code from NREL [152], OVERFLOW2 by Chow et al. [143], Overset by Cheng et al. [153], Open FOAM by Liu et al.

[154], Open FOAM-MRF by Wu et al. [154], and EllipSys3D by Sorensen et al. [155] and nonlinear vortex lattice method (NVLM) by Lee et al. [156]. Design and simulation parameters were chosen as similar as possible in ALM and FAST simulations. Figure 27 indicates that the results of the ALM code are in perfect agreement with those reported by Chow; thus, the currently developed ALM code is not case-dependent and valid for both cases.

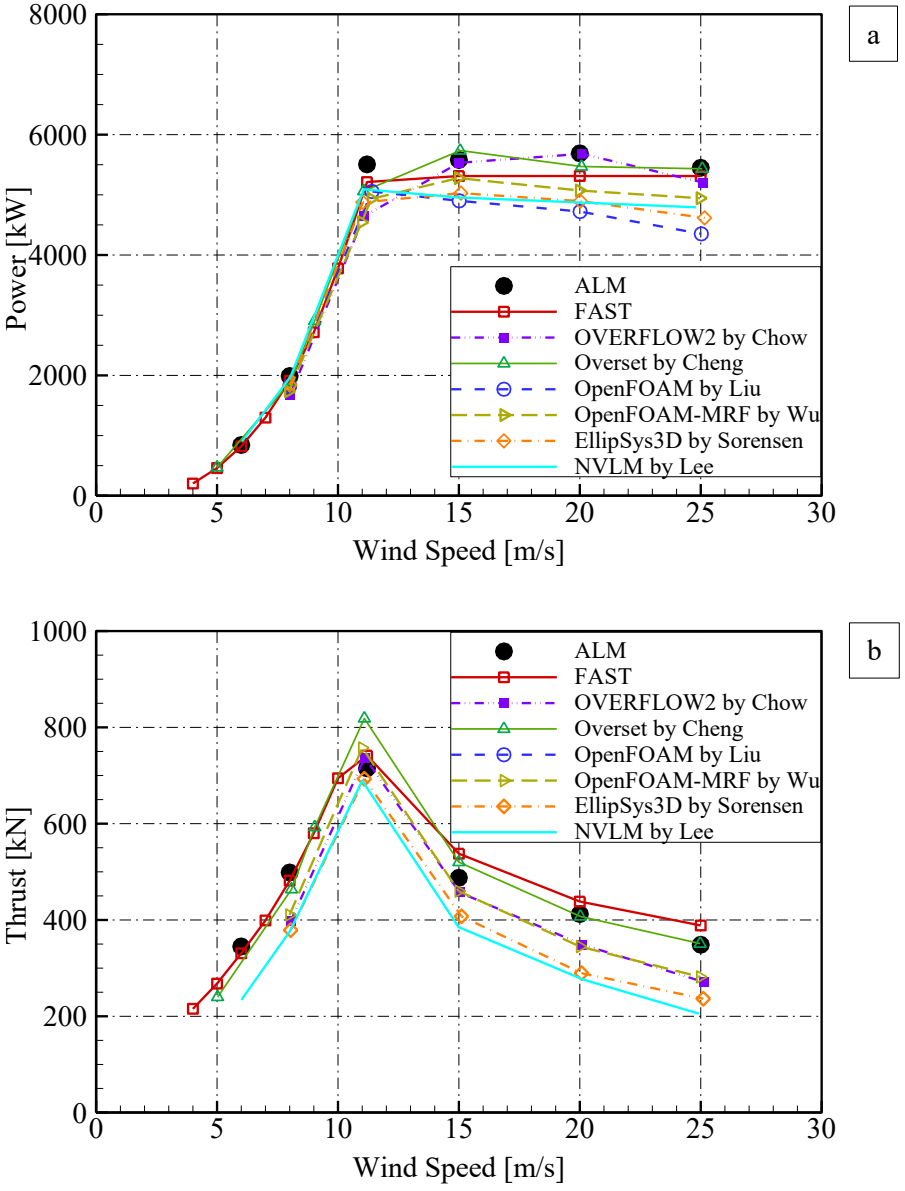

Figure 27. Comparison of ALM results with the FAST code and other literature [143,153–156], for NREL 5-MW wind turbine.

The main benefit of ALM over the other high-fidelity models is the comparatively low computational cost. Therefore, the computational cost for the developed ALM code, a Blade-resolved RANS simulation [157], and a Blade-resolved LES simulation [158] are compared in Table 9. As can be observed, even using a smaller time step, the ALM code is significantly less expensive in terms of computing. It is worth noting that the computational time for delivering results using BEM codes such as FAST is some minutes. Therefore, the point that makes ALM favorable over BEM is the shortcoming of BEM in capturing wake geometry, 3D inflow distribution, and weakness in skewed flows, yaw condition, and the vortex ring state. These occurrences are even more important in floating offshore wind farms than onshore wind farms.

Table 9. Comparison of the computational cost of the three models

Model	*ALM*	*Blade-resolved RANS [157]*	*Blade-resolved LES [158]*
Number of cells	~ 0.4 *10^6	8.5*10^6	11*10^6
dθ [°]	0.86	2	1
CPU model	Xenon4116-2.1 GHz	Xeon4116-2.1 GHz	2.4 GHz
Core hours / revolution [hr]	0.5	40	266

4. Results and discussion

This section uses the developed actuator line model to study floating offshore wind turbines. After verifying the results and comparing the results with available data in the literature, different movements of an offshore floating wind turbine will be investigated.

4.1 Platform Layout

In this study, we are analyzing the spatial arrangement of three offshore wind turbines configured in a triangular formation. The rotors are strategically positioned to optimize energy capture while minimizing wake interference. The analysis focuses on specific angular positions that are critical for understanding the dynamics of the rotor's layout.

The results indicate that in 40°, 50°, 60°, 100°, 110°, and 120°, the changes in rotor positioning and overlap are like those observed in 0°, 10°, 20°, 30°, 70°, 80°, 90°. As a result, analyzing the first group angles would likely repeat the same patterns due to the Chiasmus patterns of Turbines. Therefore, we focus only on the key angles (main 7 angles), as they provide a complete understanding of the rotor configuration without unnecessary repetition as shown in Figure 28.

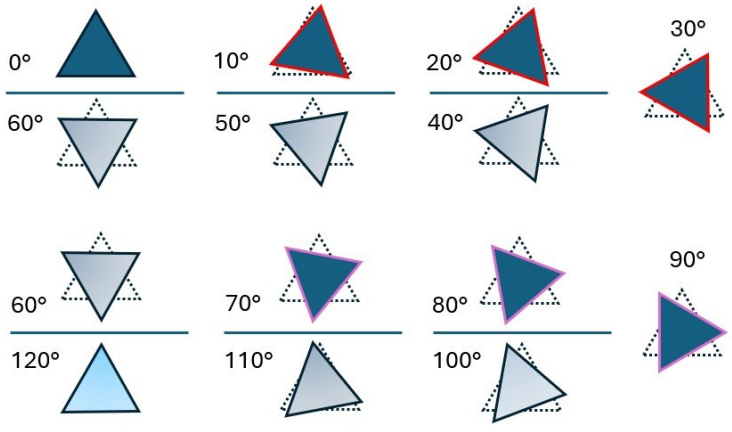

Figure 28. Triangular Offshore Wind Turbines Layout with 10 degrees of rotors Rotation

The rotors labeled A, B, and C in the vertex of the triangle (Figure 29) [159], are arranged at the vertices of an equilateral triangle. This geometric layout ensures that each rotor is equidistant from the others, providing a balanced distribution of aerodynamic forces. The triangle rotates, with critical data points recorded at specific angles to assess the impact on energy efficiency and wake interactions.

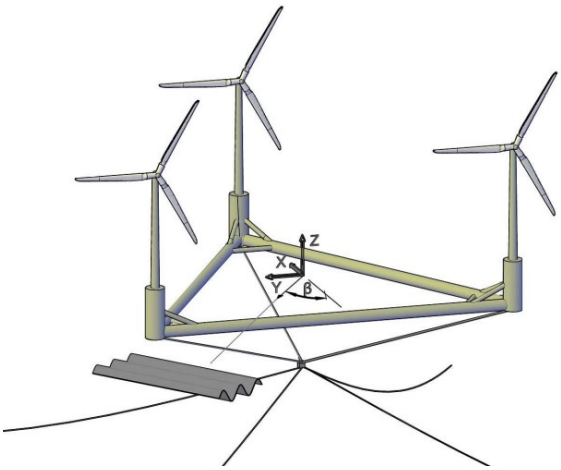

Figure 29. Schematic of the wind Turbines rotor on triangular platform

As shown in Figure 29, the structural layout of a triangular platform supporting three floating offshore wind turbines. The rotors are positioned at each corner of the triangular framework, which is held in place by mooring lines that anchor it to the seabed. This configuration is optimized for shared infrastructure, reducing anchor costs and potentially enhancing stability in oceanic conditions. The platform's triangular shape is designed to minimize wave-induced motion and improve overall efficiency, while the mooring system ensures that the structure remains securely anchored in place despite the dynamic forces acting upon it. This innovative design helps improve the deployment of floating offshore wind turbines in deeper waters, where wind speeds are higher and more consistent. Figure 30 illustrates the rotational pathways of three offshore rotors arranged in a triangular configuration, with positional analysis conducted at key angular intervals (0°–360°). Each line represents the direction and movement of the rotors at specific angles, showcasing how their spatial arrangement shifts as the triangle rotates. The chart highlights the changes in positioning at different angles, with arrows indicating turbine alignment at intervals such as 0°, 10°, 20°, and 30°, as well as 40°, 50°, 60°, 100°, 110°, and 120°. This visual representation demonstrates the symmetrical nature of the turbine positions as the angles progress, revealing patterns of

alignment and overlap that are essential for understanding aerodynamic interactions and wake effects.

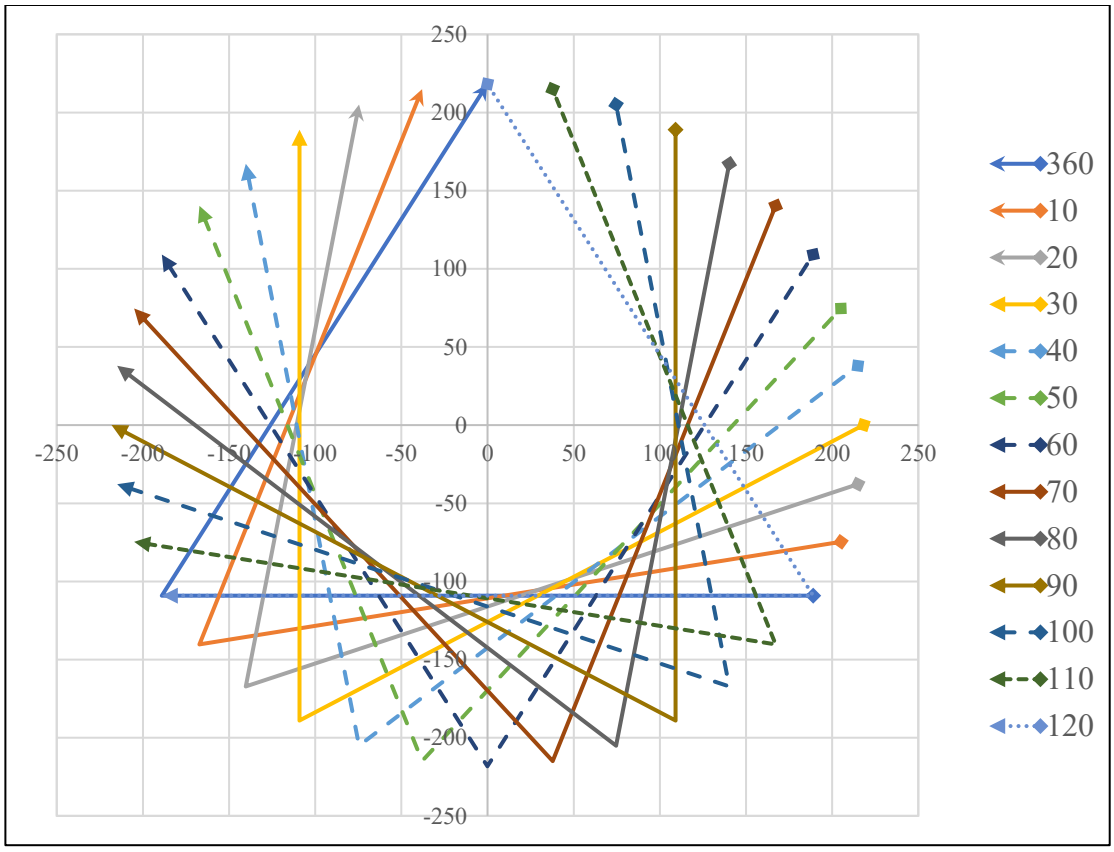

Figure 30. Rotational Pathways of Offshore Wind Turbines in a Triangular Configuration: Positional Analysis at Key Angular Intervals (0°-360°)

Table 10 provides a detailed analysis of the positional coordinates and overlap values for three rotors (A, B, and C) arranged in a triangular configuration at key angular intervals. The coordinates for each turbine are listed at various angles. The table highlights the overlap values between the rotors, with positive values indicating overlap and negative values representing a reduction in overlap. For instance, at 0°, the overlap is 2, but as the rotors rotate to 30°, the overlap becomes -1, and further reduces to -3.90 at 80°. Additionally, the minimum lateral distance between the rotors is presented, revealing key intervals where the rotors are closest (0° and 70°) or farther apart (30°, 90°), which directly impacts wake interactions and energy efficiency. In this study, avoiding overlap in the wake of rotors is crucial because when one rotor is positioned in the wake of another, it receives lower wind energy due to the drop in wind speed behind the first rotor. This wake interference not only reduces the power output but also increases the mechanical stress on turbines, decreasing their efficiency and lifespan. Figure 31 visually complements the data in the table by illustrating the changes in the overlap between

rotor A and B as the angular configurations shift. As a result, we have overlap on wake till 20° and after that as the overlap on rotor A and B is almost eliminated, thus, which means the turbines are positioned with minimal wake interaction.

Table 10. Positional Coordinates and Overlap Values for Offshore Wind Turbines in a Triangular Configuration at Key angles

Angle (degrees)	*Turbine A Coordinates*	*Turbine B Coordinates*	*Turbine C Coordinates*	*Overlap*	*Minimum Lateral Distance*
0°	(0.00, 218.24)	(-189.00, -109.11)	(189, -109.11)	2	0
10°	(-37.90, 214.92)	(-167.18, 140.28)	(205.07, -74.64)	0.95	66
20°	(-74.64, 205.08)	(-140.28, -167.18)	(214.92, -37.90)	-0.05	129
30°	(-109.12, 189.00)	(-109.12, -189)	(218.23, 0.00)	-1	189
70°	(-205.07, 74.64)	(37.89, -214.94)	(167.18, 140.28)	-3.63	66
80°	(-214.92, 37.90)	(74.64, -205.07)	(140.28, 167.18)	-3.90	129
90°	(-218.24, 0.00)	(-109.11, -189)	(109.11, 189)	-4	189

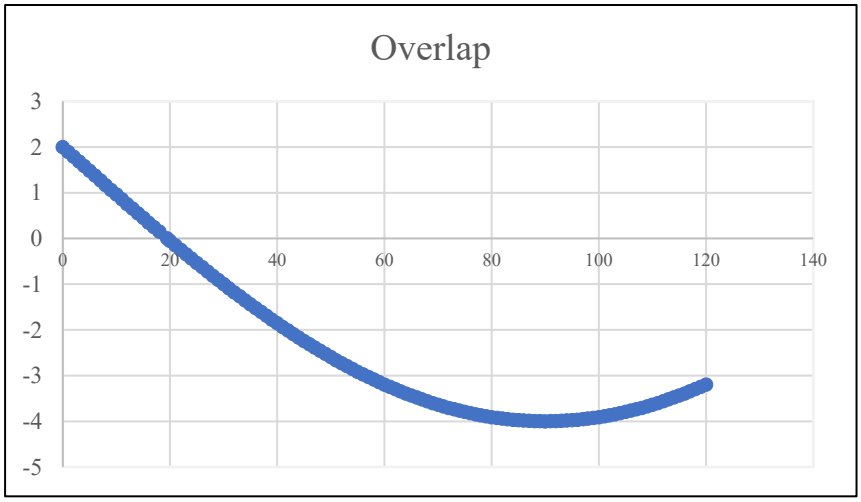

Figure 31. Overlap between Turbines A and B changes in different configurations.

Generally, adjusting the angles between rotors can improve the efficiency of an offshore wind farm. By placing the rotors in a way that reduces overlap, wake losses are minimized, and energy output increases. The key angles in the table highlight points where small changes in rotor layout can make a big difference in performance.

4.2 Power and Thrust Coefficients

Figure 32 illustrates the Mean Power/Thrust Coefficient for three turbines on a triangular platform at different rotational angles. Each bar represents the mean power coefficient of the rotors, with orange for the rotor B (the one facing the wind directly), blue for the A, and green for the rotor C as downstream turbine, which is typically affected by wake effects from the others. Across the angles, rotor B consistently has the highest power coefficient, as it receives the direct impact of the wind. Rotor A shows relatively stable performance, while rotor C exhibits the lowest values at most angles due to reduced wind exposure from wake interference.

As the platform rotates through various angles, performance shifts occur. Rotor C improves significantly at angles like T20, T30, T80, and T90 where wake effects are minimized, allowing it to capture more energy. The highest overall efficiency is observed around the T30 and T90 configurations, where all three rotors exhibit relatively balanced performance. This suggests that rotation can optimize energy generation by mitigating aerodynamic interference between the rotors, particularly by improving the downstream turbine's output. The standard deviation for all rotors is relatively low, indicating more stable and consistent power/thrust output across those orientations. However, at T10 and T70, the downstream rotor shows the highest variability, indicating that this angle produces significant fluctuations in wind energy capture due to complex aerodynamic effects, particularly wake interactions. The relatively low standard deviation at T90 indicates more balanced and stable turbine performance at this orientation, where wake effects appear to be minimized.

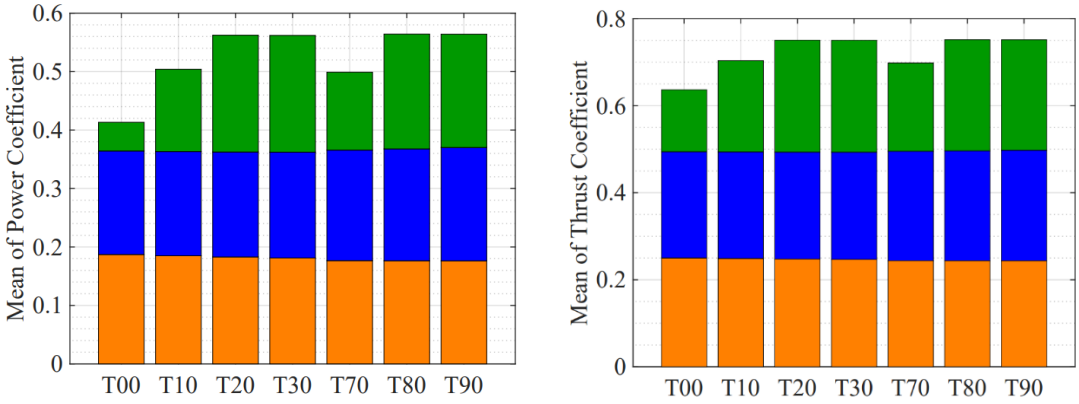

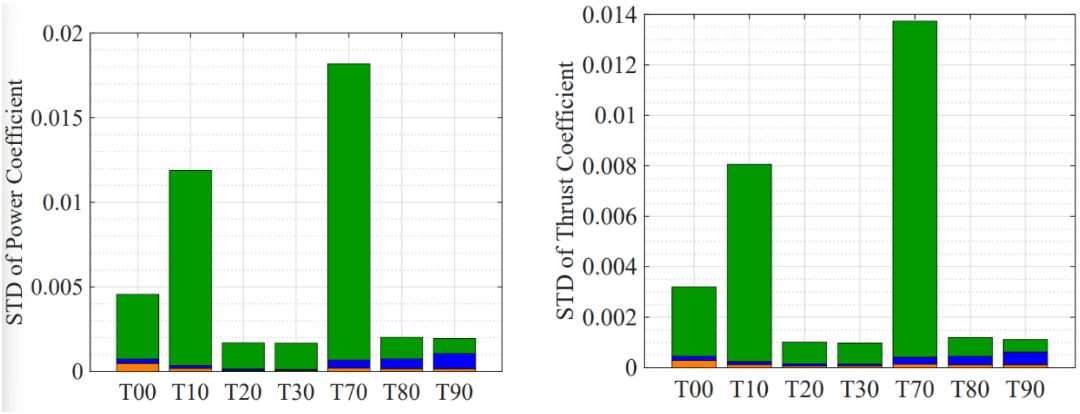

Figure 32. Average and standard deviations of the power and thrust coefficients for different configurations.

4.3 Out-of-Plane (OOP) Bending Moment and Angle of Attack (AoA)

The OOP bending moment is a critical structural parameter that measures the stresses on the turbine blades due to aerodynamic forces. In the Mean OOP Bending Moment graph as shown in Figure 33, Rotor B and A consistently show high bending moments across all angles, as they directly face the wind and experience the strongest forces. Rotor C generally sees lower mean bending moments but peaks around T20, T30, T80, and T90, indicating reduced wake effects and more evenly distributed aerodynamic loads also illustrates the variability in bending moments across different angles. T10 and T70 exhibit significant fluctuations, suggesting that these angles create unstable aerodynamic conditions and strong wake interference.

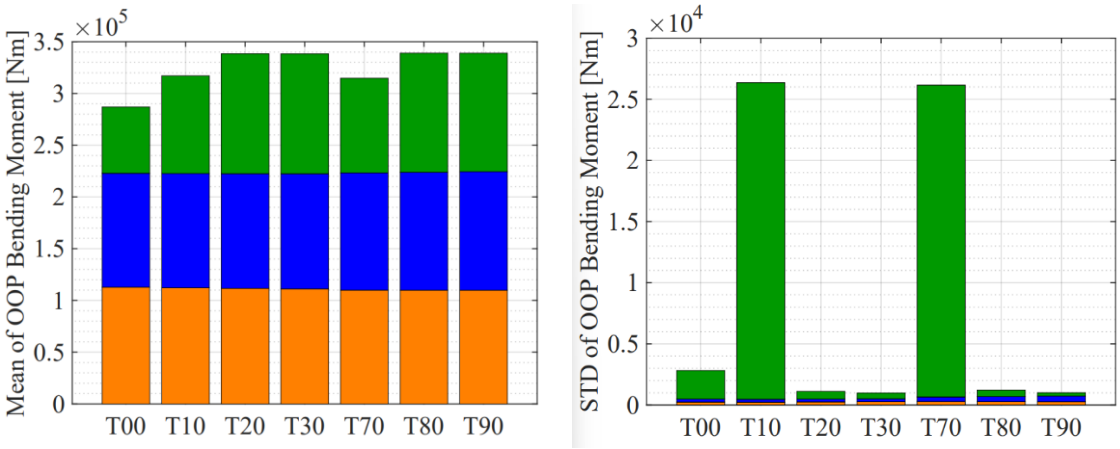

Figure 33. Average and standard deviations of OOP bending moments for different configurations.

Figure 34 illustrates the variations in the angle of attack (AoA) for rotor C under different angular configurations, highlighting the impact of wake interactions at specific angles. At T00, T10, and T70, rotor C experiences significant wake interference, as shown by the dark blue regions in the plots. These regions indicate areas of reduced blade velocity caused by the wake of upstream rotors. At T00, the two rotors are aligned in a straight line, causing the wake from one turbine to directly pass over turbine C, reducing its aerodynamic efficiency. Similarly, at T10 and T70, although the turbines are slightly offset, the wake still affects rotor C due to the proximity and alignment of the turbines in these configurations. The disturbed airflow at these angles leads to reduced energy capture and lower AoA values, showing the detrimental effects of wake interactions.

In contrast, at angles like T20, T30, and T80, rotor C operates in relatively clean airflow, with minimal wake interference from the other turbines. The AoA variations in these configurations are much more uniform, and the absence of dark blue regions indicates that rotor C is not significantly affected by the wake. These angles result in more optimal aerodynamic conditions for rotor C, allowing it to maintain higher efficiency. The comparison between these configurations emphasizes the importance of turbine positioning and angular arrangement in mitigating wake effects and maximizing overall energy capture. By selecting angles where rotors are not directly aligned, such as T20, T30, and T80, the wake interaction can be minimized, leading to improved performance across the wind farm.

Understanding these patterns is crucial for identifying optimal rotor configurations that enhance performance while minimizing aerodynamic stress. By analyzing the Angle of Attack (AoA) over time and across the blade's span, engineers can identify areas where turbulence, wake effects, or flow disturbances occur. Higher fluctuations in AoA indicate regions where the turbine may experience inefficiencies or mechanical stress, leading to performance loss or potential structural issues. Thus, these graphs help in optimizing turbine design and selecting configurations that reduce aerodynamic stress and improve efficiency.

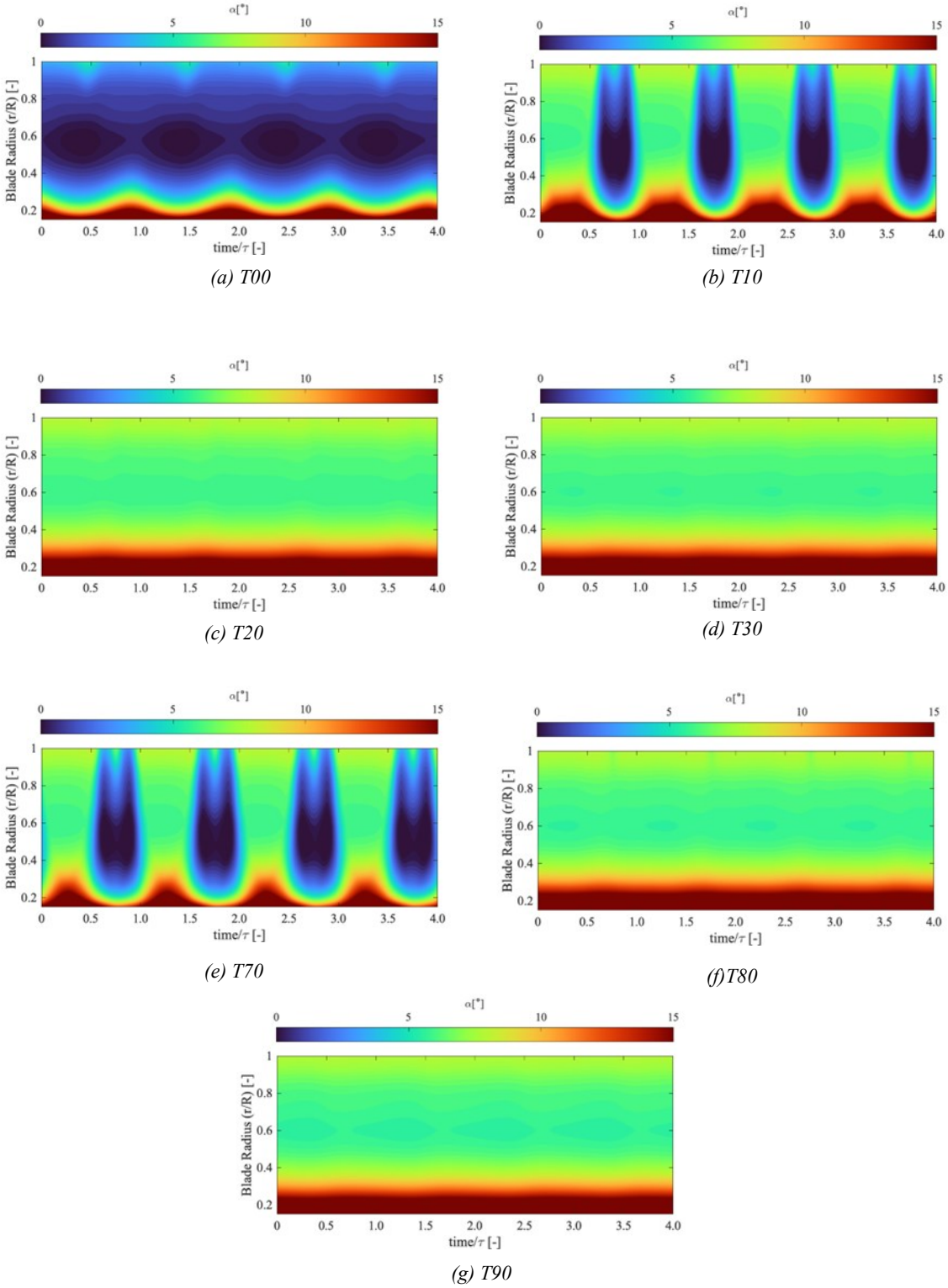

(a) T00

(b) T10

(c) T20

(d) T30

(e) T70

(f)T80

(g) T90

Figure 34. The angle of Attack (AoA) variations over time for turbine C in different platform configurations

4.4 Power Spectral Density (PSD) and Wake Dynamics

The AoA of each spanwise location varies as the rotors rotates. The AOA variation range and its main involving frequencies provide valuable information for turbine designers. Hence, the spanwise distributions of the AoA histogram are presented in figure 35, providing insights into the dynamic behavior of wind turbine blades under different conditions. As shown in these plots, the PSD of AoA for various turbine configurations.

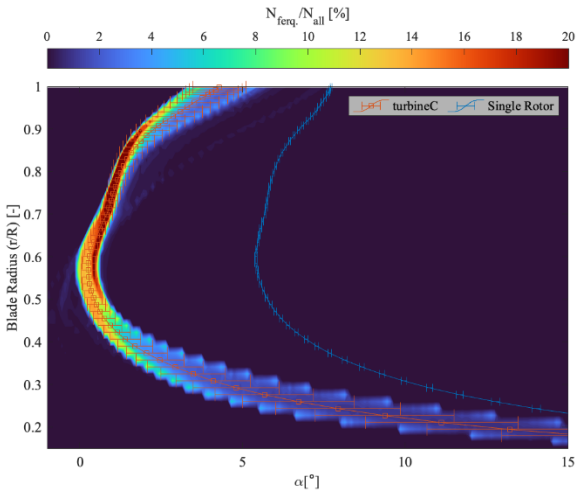

(a) T00

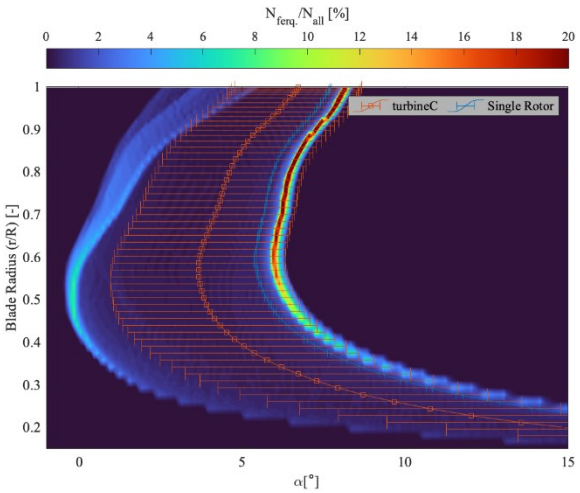

(b) T10

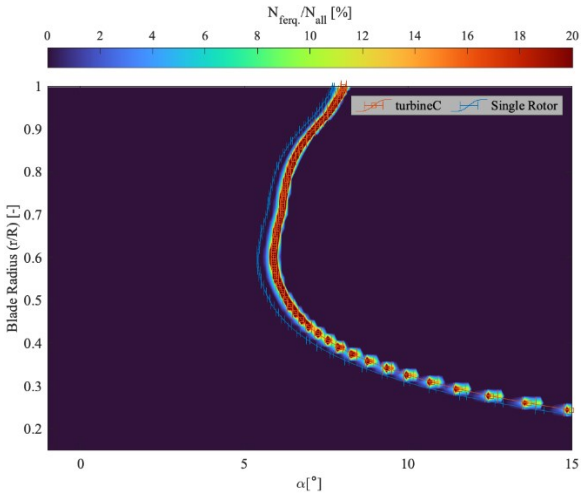

(c) T20

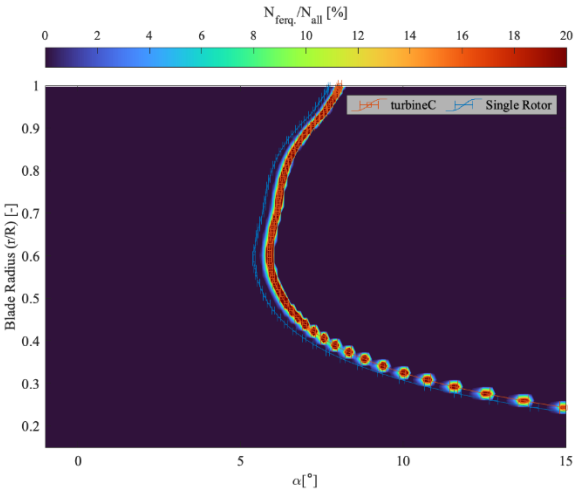

(d) T30

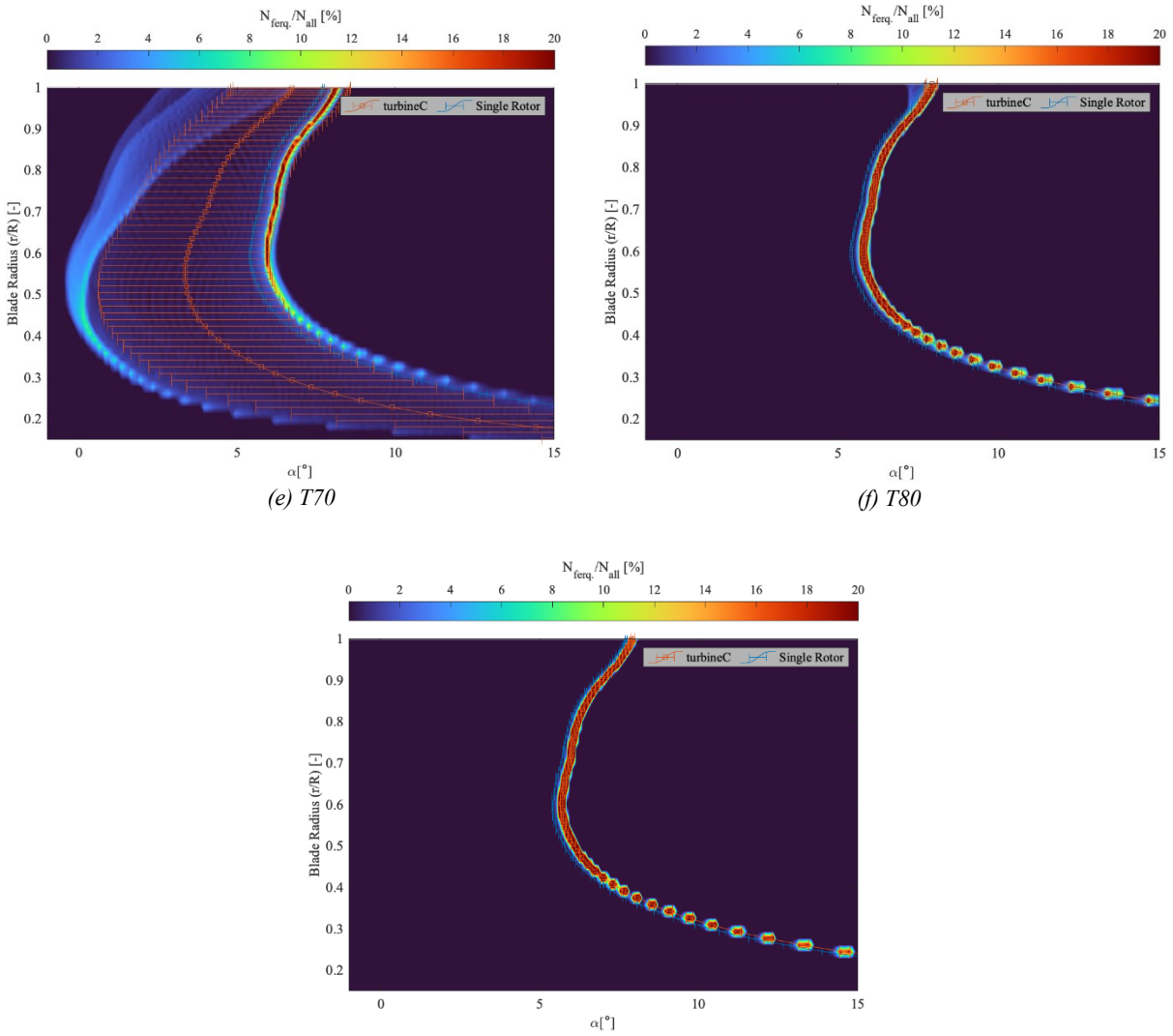

(e) T70 *(f) T80*

(g) T90

Figure 35. The spanwise distributions of the AoA histogram for the blade-1 of the turbine C mounted at various locations.

The AoA variation across the blade's span is shown, with higher PSD values (in warmer colors) indicating more significant fluctuations, which may lead to aerodynamic inefficiencies. Configurations like T20, T30, T80, and T90 display more stable aerodynamic performance, with fewer fluctuations and smoother AoA distributions, indicating minimal turbulence and better flow control.

In contrast, configurations such as T00, T10, and T70 show higher PSD concentrations, particularly toward the blade tip, which suggests increased turbulence and wake effects. These configurations could face aerodynamic inefficiencies due to excessive AoA variations, which would lead to performance losses. The analysis of these graphs helps identify optimal configurations that offer better flow stability and minimize the risk of performance degradation

due to wake interactions and turbulent conditions. This figure also represents the superior capability of ALM with respect to ADM, where the variation of AoA at different spanwise blade locations is presented. In this figure, the corresponding performance of NREL single wind turbine is also given (denoted by single rotor), as a result, one can compare the spanwise variation of AoA for rotor C in a triangular structure with single rotor wind turbine in the same altitude. The blade designer needs to account for the AoA variations at each spanwise location of the turbine blade, so that the blade thickness can be adjusted accordingly, leading to enhanced structural durability with minimum weight, to identify the involved frequencies and the sources of fluctuations at each spanwise location, the corresponding PSD of the spanwise AoA are depicted in figure 36.

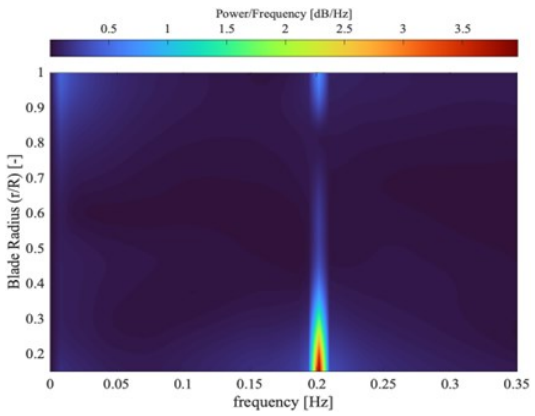

(a) T00

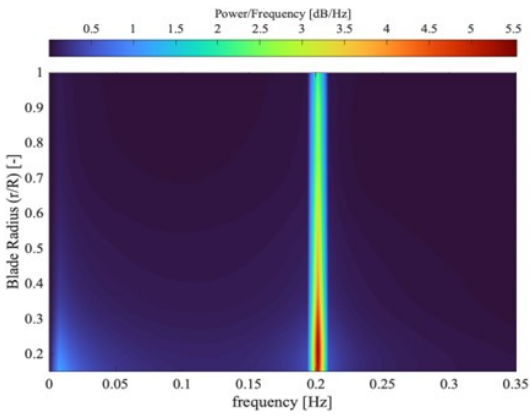

(b) T10

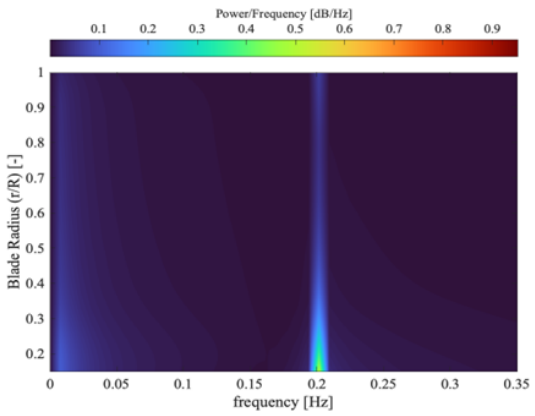

(c) T20

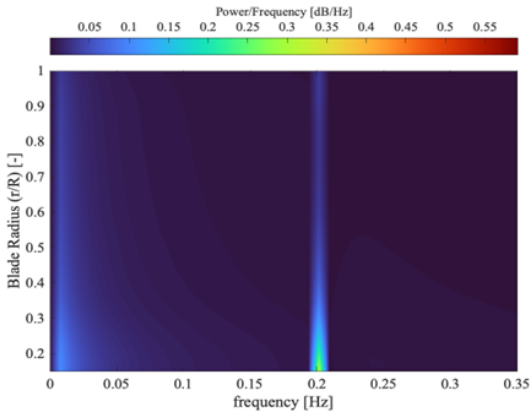

(d) T30

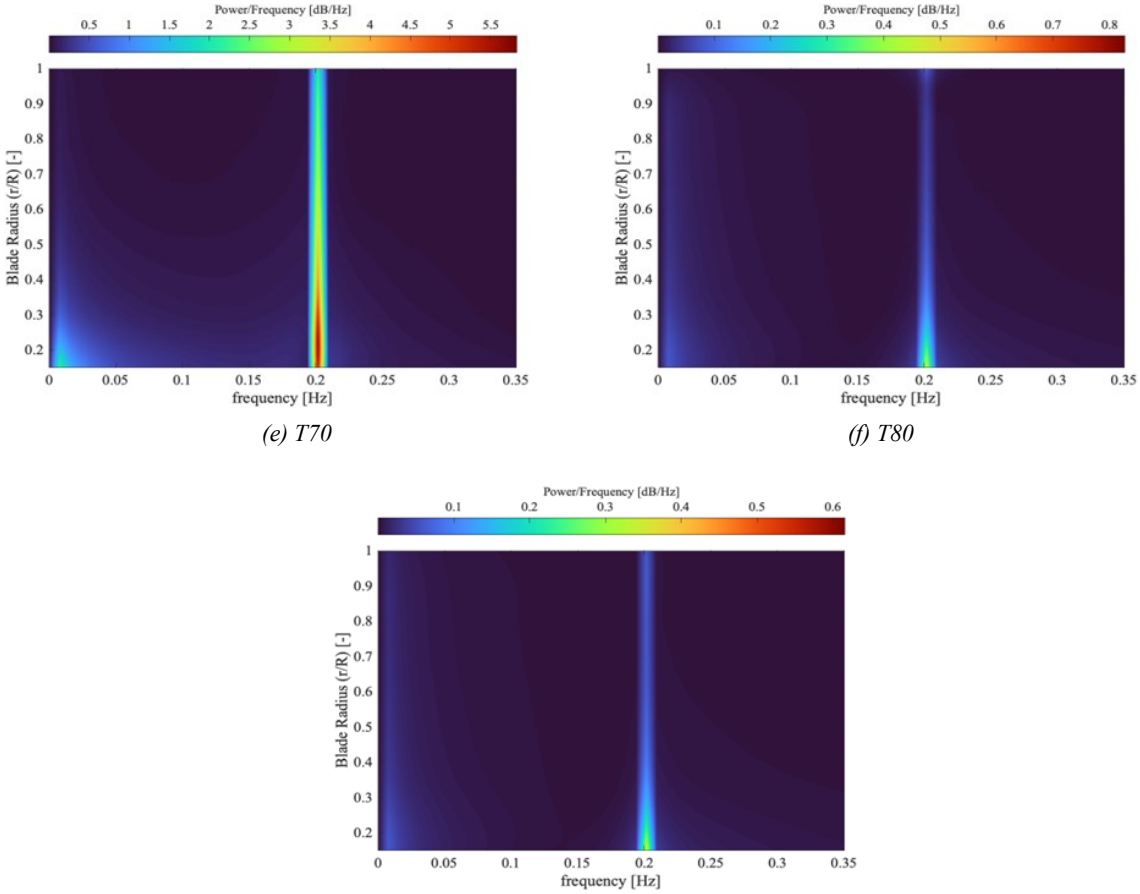

(e) T70

(f) T80

(g) T90

Figure 36. PSD of the spanwise AoA histogram for the blade-1 of the turbine C mounted at various locations.

Figure 36 represents the Power Spectral Density (PSD) distribution for the blade root of rotor C at different configurations. Peaks near 0.2 Hz in T00, T10, and T70 indicate potential resonant frequencies, which could lead to dynamic stresses at the blade root. These peaks suggest increased vibrational power near the root, indicating areas of potential concern for mechanical stress and turbine stability.

On the other hand, configurations T20, T30, T80, and T90 exhibit much lower power across all frequencies, suggesting more stable performance with minimal vibration-induced stress. These configurations are likely more efficient in reducing the dynamic loads on the turbine, particularly near the root, where mechanical stresses are typically higher. The PSD analysis is critical in identifying optimal configurations that minimize resonance and vibrational stress, improving the overall efficiency and durability of the turbine.

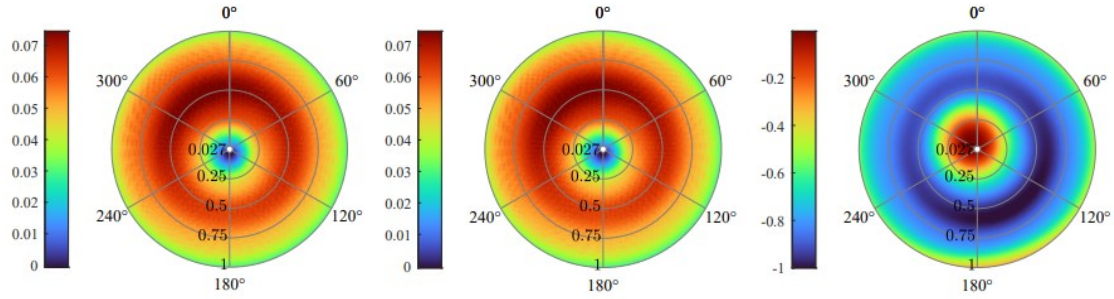

(a)T00

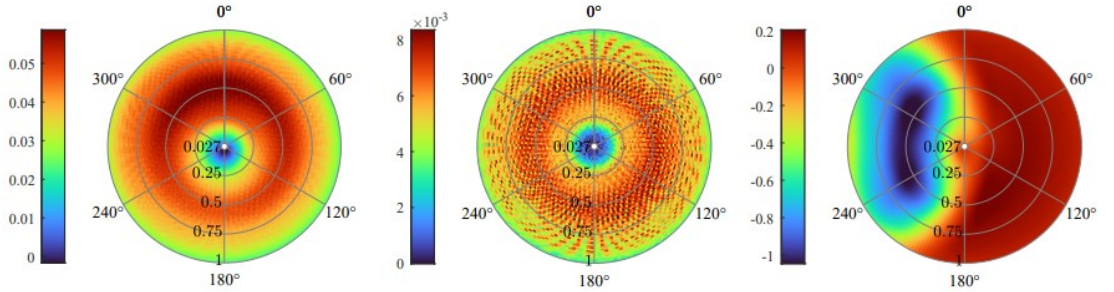

(b) T10

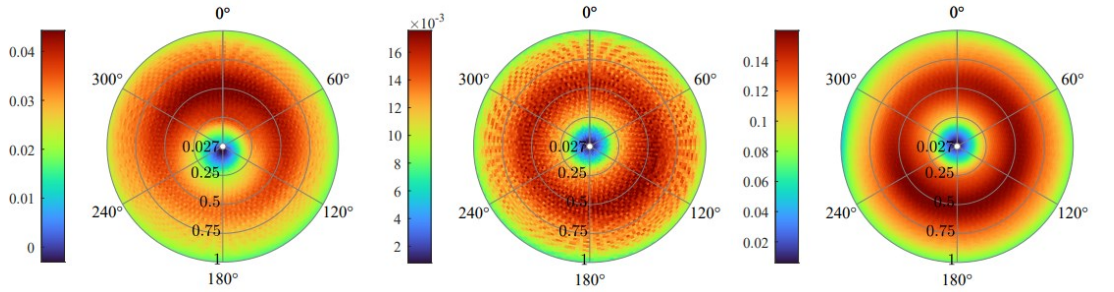

(c) T20

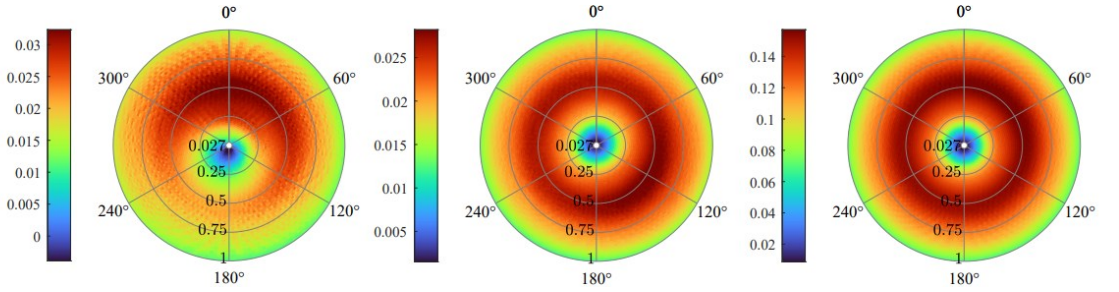

(d) T30

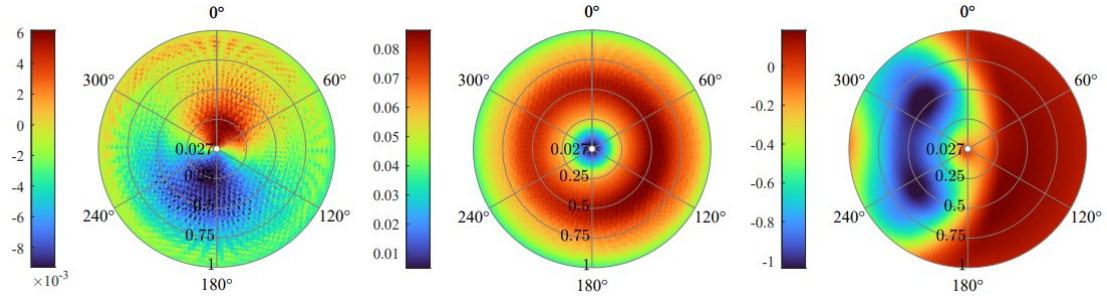

(e) T70

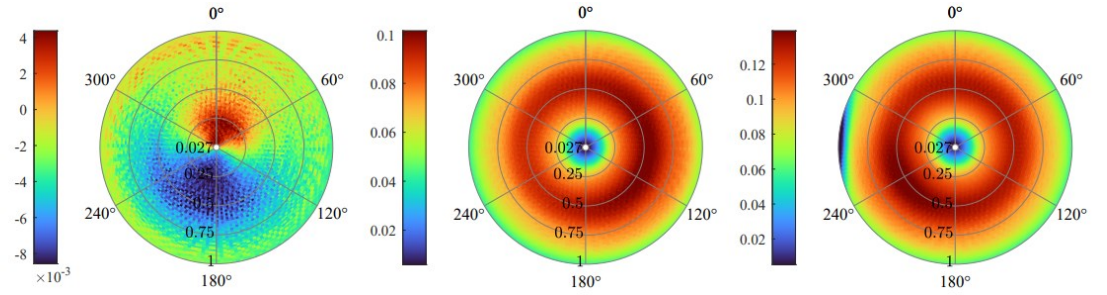

(f) T80

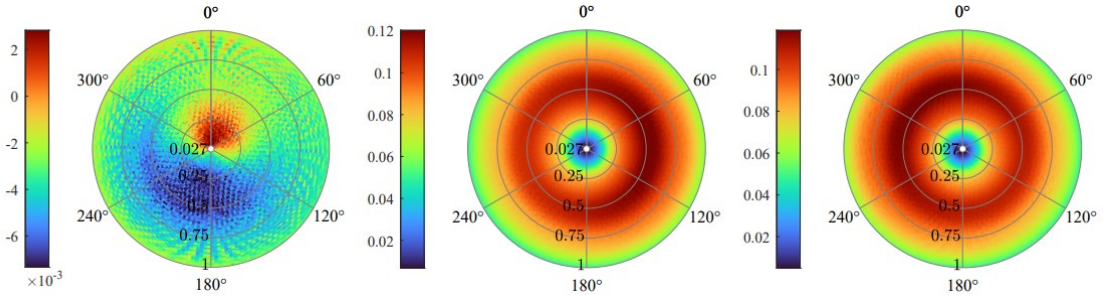

(g) T90

Figure 37. Polar distribution of AOA of one blade for the wind turbines A, B, and C at different platform configurations.

Contour plots shown in Figure 37 illustrate the flow dynamics of rotors A, B, and C (velocity distribution) for different platform configurations labeled from T00 to T90. The plots provide a visual representation of how different angles impact the pressure distribution and the wind velocity, especially of rotor C. The plot shows the intensity of the flow with warmer colors representing higher velocity and cooler colors showing lower values. The third plot helps to identify the wake effects of rotor C in different platform configurations.

In the T00 configuration, the flow appears symmetrical and balanced for the rotor A and B, with minimal wake disturbances as we do not have wake interaction but for rotor C, we have maximum wake interaction and the warmer color in the plot indicates this. In T10 and T70 also we can see wake interaction on rotor C. These configurations reveal more turbulence, which can disrupt energy capture and result in mechanical stress. In contrast, configurations such as T20, T30, T80, and T90 offer more efficient aerodynamic performance for rotor C.

This analysis is critical for optimizing turbine positioning, blade design, and overall energy capture by minimizing turbulence and improving airflow around the blades.

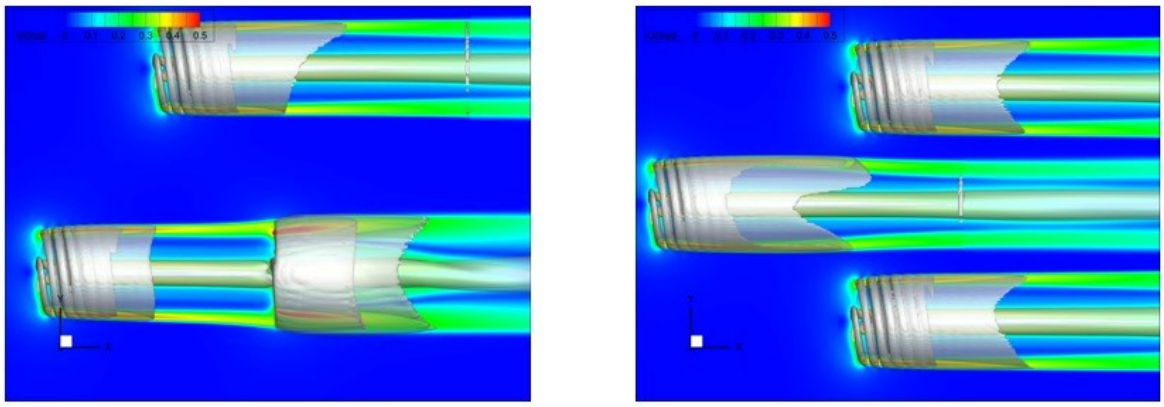

(a) T00 *(b) T90*

Figure 38. Iso surface Q-criterion ($Q=10^{-3}$ and 10^{-4}) colored by velocity gradient magnitude for a) T00 configuration, b) T90 configuration

In this section, the detailed aerodynamic analysis of wake propagation and interaction with turbines are studied to identify the sources of power and thrust variation. Figure 38 shows the top view of the visualized wake for the T00 and T90 configurations. The wake visualization was conducted using the iso-surface of the Q-criterion [160] at values of 10^{-3} and 10^{-4}, with color indicating the magnitude of the velocity and has been calculated using the following relation:

$$Q = \frac{1}{2}[\|\Omega\|^2 - \|S\|^2] \tag{30}$$

Where $\|\Omega\|$ and $\|S\|$ are the antisymmetric and symmetric sections of the velocity gradient tensor, which can be calculated as:

$$\Omega = \frac{1}{2}[\nabla \boldsymbol{u} - (\nabla \boldsymbol{u})^T] \tag{31}$$

$$S = \frac{1}{2}[\nabla \boldsymbol{u} + (\nabla \boldsymbol{u})^T] \quad (32)$$

This equation implies that positive Q-criterion iso-surface isolates the regions where vorticity over weights the strain rate. This figure illustrates how the motion of the upstream rotor influences the inflow of the downstream rotor. In the left image (a), corresponding T00, the wakes are aligned directly behind the rotors, the three-dimensional view shown in Figure 39, shows significant wake interactions for the downstream rotor as you can see three-dimensional. This alignment leads to a reduction in wind speed and increased turbulence for the downstream rotor, diminishing its performance due to the lower energy content in the incoming wind. The visualized wake patterns show a concentrated area of reduced velocity, meaning that the downstream rotor in this configuration is likely to experience higher aerodynamic loads and reduced efficiency.

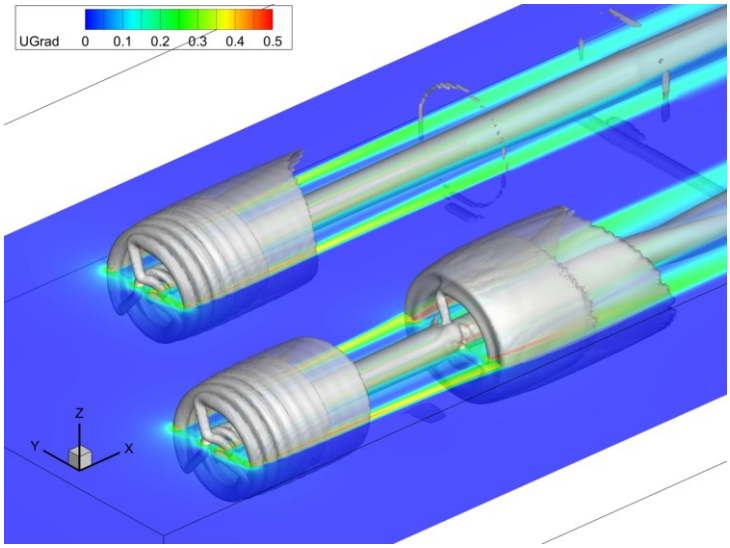

Figure 39. Iso surface Q-criterion ($Q=10^{-3}$ and 10^{-4}) colored by velocity gradient magnitude, Three-dimensional view for T00

In contrast, Figure 38-b, T90, shows the wake spreading in a different pattern, with less direct wake interaction between the rotors. The separation of the wake regions indicates less interference with the downstream rotor, allowing it to operate in a higher-velocity wind field with less turbulence. This results in better performance for the downstream rotor, as it is not as severely affected by the disturbed airflows from the upstream rotors (A and B). Thus, T90

would be more favorable in terms of minimizing wake effects and maximizing the efficiency of the entire turbine array.

The discrepancy observed in wake structures is of paramount importance in wind farm design. Especially from the perspective of a downstream rotor, the axial velocity distribution directly shapes the inflow conditions. These conditions play a key role in determining the aerodynamic and fatigue loads experienced by the downstream rotor. Consequently, the formation of the flow received by the downstream directly influences its power output. A crucial question in wind farm design is determining the configuration at which the inflow received by the downstream rotor sufficiently recovered. The term "recovery" can be defined based on different criteria, like the mean velocity over the rotor disk, the mean velocity at each point, or the instantaneous velocity at each point considering the oscillations in flow velocity. From Figure 38-a and Figure 39, the wake patterns reveal a new consideration in determining the optimum configuration for rotors. In T00, rotor C is significantly affected by upstream wake.

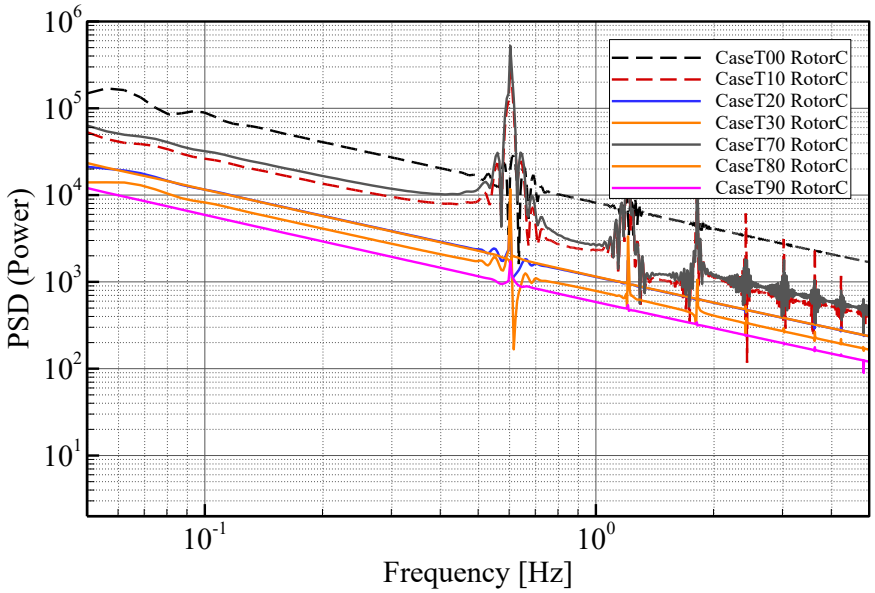

Figure 40. Power Spectral Density (PSD) of rotor C in different configurations.

The PSD graph in Figure 39 helps evaluate how much power is concentrated at specific frequencies, revealing key vibrational modes that affect turbine performance. Configurations T00, T70, and T10 exhibit higher power levels across a broad frequency range, indicating greater dynamic loading and resonance, which could cause stress on the turbine structure.

In contrast, T20, T30, T80, and T90 demonstrate lower power distributions, indicating more stable dynamics and reduced mechanical stress. This analysis is crucial because it helps identify

critical frequencies where turbines may experience resonance, which could lead to fatigue and performance degradation. By minimizing the power at these frequencies, engineers can ensure better turbine longevity and operational efficiency.

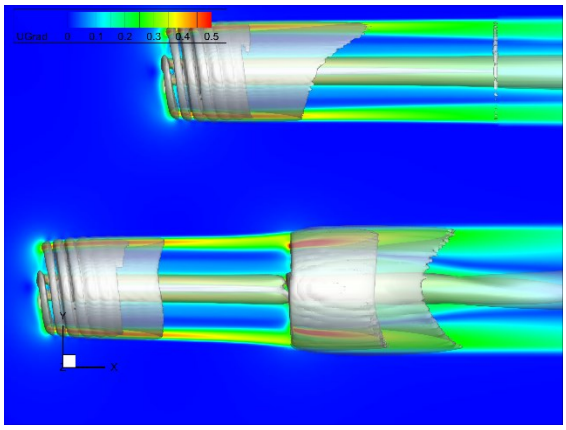

(a) T00

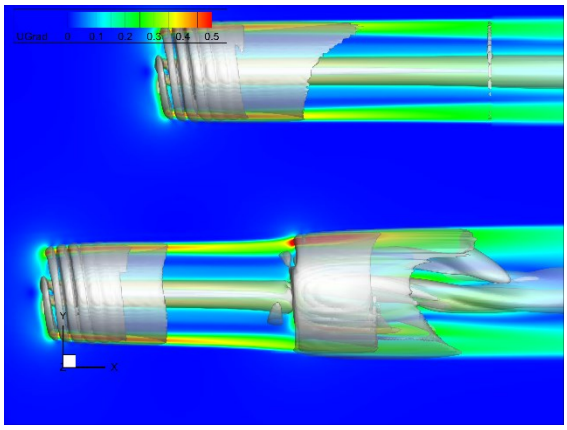

(b) T2.5

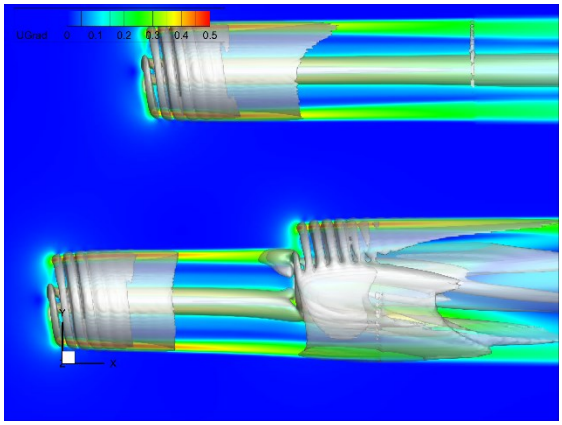

(c) T7.5

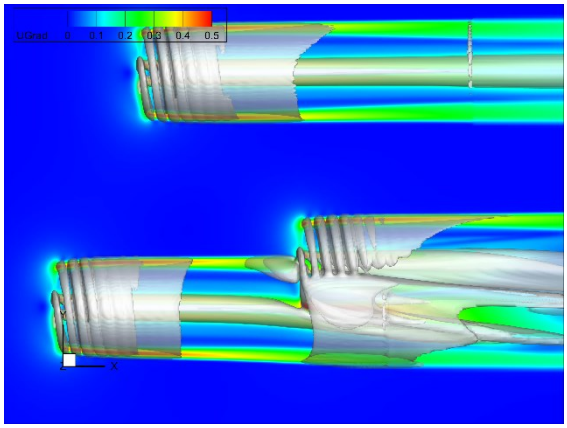

(d) T10

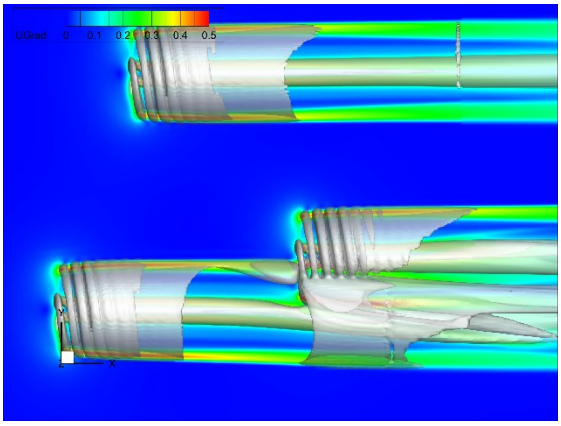

(e) T12.5

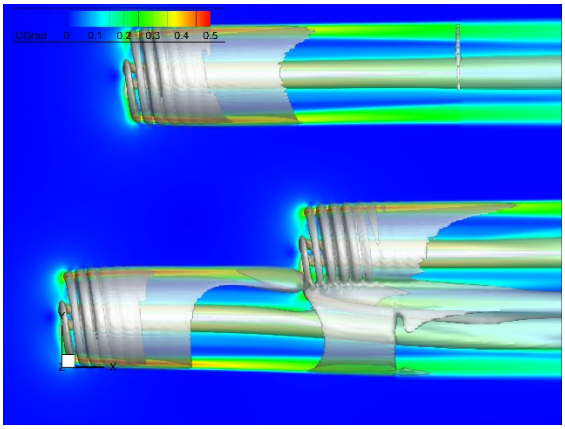

(f) T15

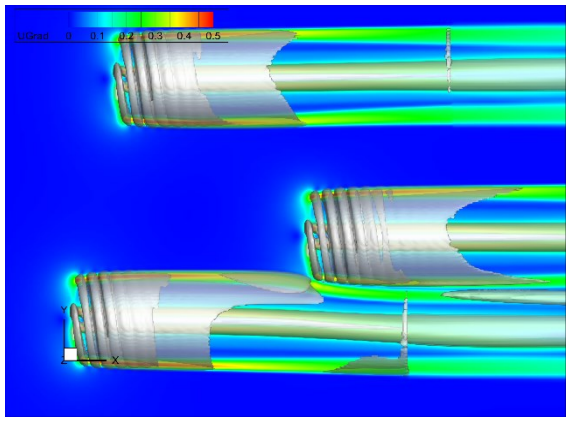

(g) T20

Figure 41. Iso surface Q-criterion ($Q=10^{-3}$ and 10^{-4}) colored by velocity gradient magnitude for different configuration

Due to uncertainties in wind direction, small changes in the rotor's angle can occur, which affects the wake dynamics. To evaluate these effects, simulations were reducing the performance of the downstream rotor. As the rotor angle increases, the relative positioning of the rotor changes, leading to a reduction in wake overlap and interference between rotors B and C. At higher angles, such as T10 and above, the wakes become more staggered, and the wake from rotor B moves away from rotor C, reducing direct wake interaction. By T20, the wakes are sufficiently separated, minimizing the negative effects of wake interference on rotor C. This comparison across different angles shows that even small changes in rotors orientation can significantly alter the wake dynamics and improve turbine performance by reducing wake-induced power losses in the downstream rotor.

4.5. Fatigue and Aerodynamic Load Distribution

Another important parameter to evaluate in different configurations is Fatigue (tiredness) of the Turbine, R_n represents the radial distribution of aerodynamic forces (such as pressure or lift) acting on the turbine blades. Which includes pressure, lift, and drag forces. Mathematically, this can be expressed as the radial coordinate along the span of the blade, where R_n refers to the distance from the center of rotation to the point on the blade where forces

are being measured. The distribution of these forces influences the blade's loading and is critical for assessing fatigue and performance.

This would help analyze how the turbine's blades experience loading from the wind. It directly contributes to the fluctuating aerodynamic forces F_l and F_d computed at each radial point Rn, resulting in cyclic loading that causes fatigue, acting on the turbine and plays a critical role in determining how those forces are distributed, which these forces repeatedly stress the blade structure at different radial locations over time, especially at points closer to the root (higher bending moments).

By analyzing the radial distribution, engineers can identify areas of high stress and work to mitigate them, potentially prolonging the turbine's operational life. Turbine fatigue is caused by cyclic loading due to aerodynamic forces acting on the blades, tower, and other structural components over time. If R_n represents conducted at minor angles T00 to T20 as shown in Figure 40. As discussed before, in T00 the wake of rotor B fully impacts rotor C, resulting in significant wake interference, in which aerodynamic forces like pressure or wind load distributed around the turbine, can influence how the turbine components experience stress.

Figure 42, shows the wake effects at different rotor configurations, focusing on how wake interacts with rotor C. At T00 (0°), the dark blue and purple colors indicate significant wake interference, with rotor C fully exposed to rotor B's disturbed flow. This results in high turbulence and unsteady aerodynamic forces on rotor C, increasing cyclic loading and contributing to accelerated fatigue on its blades and structure. The strong wake presence at this configuration makes T00 the most problematic in terms of structural wear and fatigue for the downstream turbine.

As the configuration changes to T2.5 and T7.5, the blue regions around rotor C start to diminish, showing that rotor C is experiencing less wake interference. While some wake effects remain, especially in T2.5, the shift in wake position reduces the aerodynamic loading compared to T00, though moderate fatigue stress is still present. By T7.5, the wake is significantly shifted away, leading to more stable flow conditions and lower cyclic loading on rotor C. At these angles, while fatigue is reduced, rotor C still experiences some stress from the remaining wake.

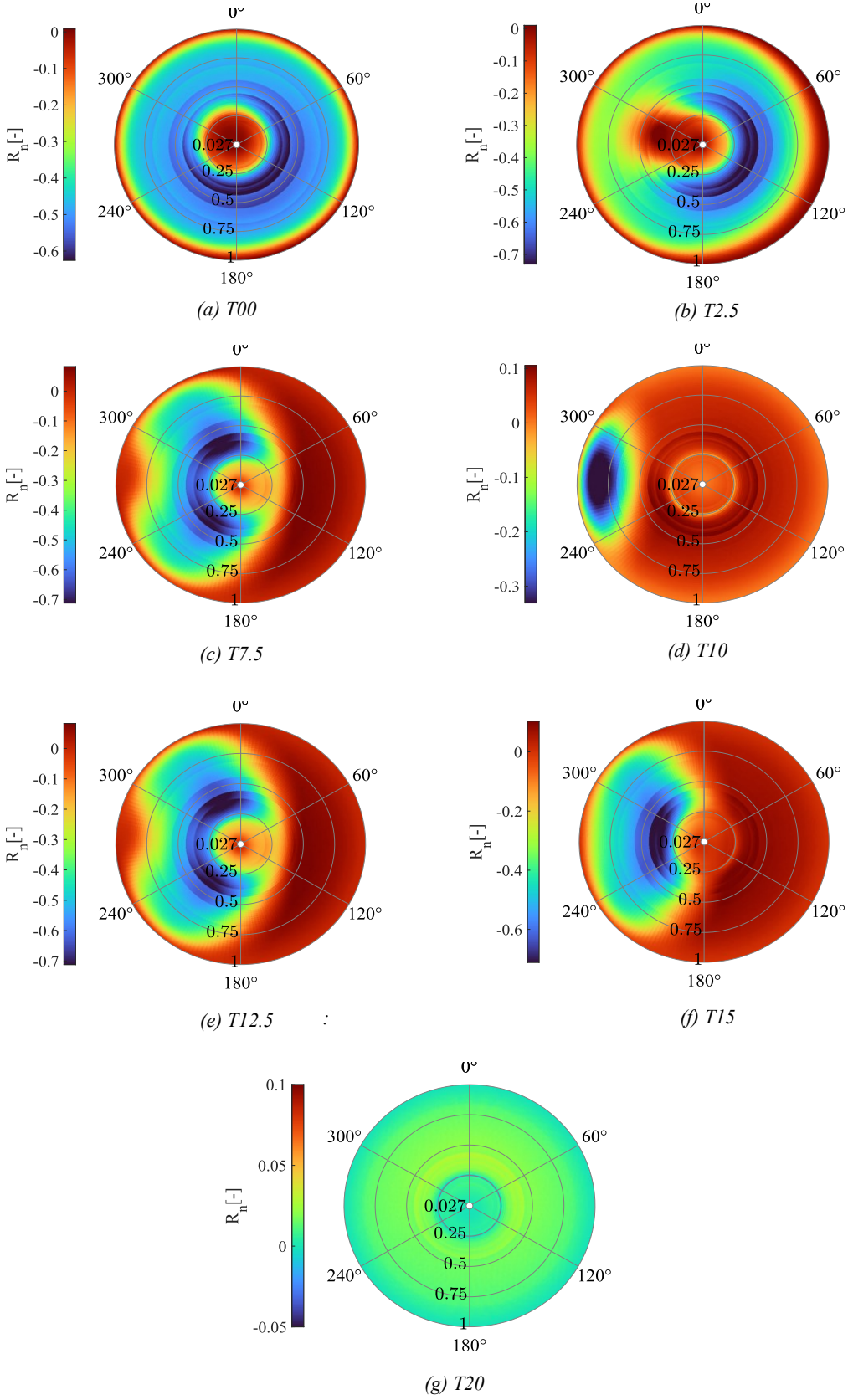

(a) T00

(b) T2.5

(c) T7.5

(d) T10

(e) T12.5

(f) T15

(g) T20

Figure 42. The wake interaction and fatigue load on the downstream turbine in different configurations

At configurations like T10, T12.5, and T15, the wake interference becomes minimal, as indicated by the predominance of green and yellow colors around rotor C. This suggests that rotor C is nearly free from wake, and the resulting aerodynamic loads are much more uniform and stable. This leads to a significant reduction in cyclic stress, minimizing fatigue and allowing rotor C to operate more efficiently. In the T20 configuration, the wake effects are almost entirely gone, as the uniform distribution of green in the plot shows. This is the optimal configuration where rotor C experiences minimal fatigue and the most favorable operating conditions, with negligible wake-induced stresses.

5. Conclusions

This thesis presents the development and implementation of an Actuator Line Model (ALM) within the OpenFOAM framework, tailored specifically for simulating Floating Offshore Wind Turbines (FOWTs). The primary goal was to evaluate the aerodynamic performance and wake interactions under various platform motions and configurations. Through detailed simulations, the model successfully captured the wake behavior and its effect on downstream turbines, providing a practical and computationally efficient alternative to fully blade-resolved models. The incorporation of platform movement was particularly essential, as FOWTs introduce complexities related to their dynamic response to wind and wave forces. The model accurately predicted wake dynamics, power coefficients, and thrust coefficients, offering critical insights into turbine performance under varying conditions.

Key findings from the results indicate that small angular deviations in rotor orientation, which are common due to uncertainties in wind direction, have significant effects on wake interactions and rotor efficiency. At T00, rotor C was heavily impacted by the wake from rotor B, resulting in lower power output and higher fatigue loads due to intense aerodynamic interference. As the higher configuration such as T10 and T20, the wake from rotor B shifted away from rotor C, reducing wake interference and improving overall rotors performance. The study found that at these optimized angles, aerodynamic loads became more evenly distributed, minimizing fatigue and enhancing efficiency. These results demonstrate the importance of optimizing rotor orientation to reduce wake-induced power losses and fatigue effects in downstream rotor.

The study's findings have important implications for the design and operation of FOWTs. By optimizing configurations, operators can mitigate the negative effects of wake interaction, prolong turbine lifespan, and enhance energy production. The Actuator Line Model developed in this thesis provides a robust and scalable tool for understanding and optimizing wake dynamics in floating wind farms. This work contributes significantly to the growing body of

research on FOWTs by offering a more accurate method to predict real-world performance, laying the groundwork for future studies aimed at reducing energy losses, improving turbine reliability, and lowering the levelized cost of energy (LCOE) in offshore wind energy projects.

Bibliography

[1] Wind energy - European Commission, (n.d.). https://research-and-innovation.ec.europa.eu/research-area/energy/wind-energy_en (accessed May 15, 2024).

[2] (16) (PDF) Assessing wind energy potential and economics for three offshore locations on the Persian Gulf in Iran, (n.d.). https://www.researchgate.net/publication/373067341_Assessing_wind_energy_potential_and_economics_for_three_offshore_locations_on_the_Persian_Gulf_in_Iran (accessed October 2, 2024).

[3] A. Moreno Gonzalez, Composites fatigue analysis of the 15 MW offshore reference wind turbine blade in BECAS and OpenFAST, (2023).

[4] E.C. Edwards, A. Holcombe, S. Brown, E. Ransley, M. Hann, D. Greaves, Evolution of floating offshore wind platforms: A review of at-sea devices, Renewable and Sustainable Energy Reviews 183 (2023) 113416. https://doi.org/10.1016/J.RSER.2023.113416.

[5] M. Barooni, T. Ashuri, D. Velioglu Sogut, S. Wood, S. Ghaderpour Taleghani, Floating Offshore Wind Turbines: Current Status and Future Prospects, Energies 2023, Vol. 16, Page 2 16 (2022) 2. https://doi.org/10.3390/EN16010002.

[6] (16) (PDF) Review on Dynamics of Offshore Floating Wind Turbine Platforms - Preprint, (n.d.). https://www.researchgate.net/publication/341464076_Review_on_Dynamics_of_Offshore_Floating_Wind_Turbine_Platforms_-_Preprint (accessed October 3, 2024).

[7] These 3 countries are global offshore wind powerhouses | World Economic Forum, (n.d.). https://www.weforum.org/agenda/2019/04/these-3-countries-are-global-offshore-wind-powerhouses/ (accessed July 24, 2024).

[8] D. Micallef, A. Rezaeiha, Floating offshore wind turbine aerodynamics: Trends and future challenges, Renewable and Sustainable Energy Reviews 152 (2021). https://doi.org/10.1016/J.RSER.2021.111696.

[9] GWECs Global Offshore Wind Report 2022 - Global Wind Energy Council, (n.d.). https://gwec.net/gwecs-global-offshore-wind-report/ (accessed May 15, 2024).

[10] E.C. Edwards, A. Holcombe, S. Brown, E. Ransley, M. Hann, D. Greaves, Evolution of floating offshore wind platforms: A review of at-sea devices, Renewable and Sustainable Energy Reviews 183 (2023) 113416. https://doi.org/10.1016/J.RSER.2023.113416.

[11] J. Bosch, I. Staffell, A.D. Hawkes, Global levelised cost of electricity from offshore wind, Energy 189 (2019) 116357. https://doi.org/10.1016/J.ENERGY.2019.116357.

[12] N. Bento, M. Fontes, Emergence of floating offshore wind energy: Technology and industry, Renewable and Sustainable Energy Reviews 99 (2019) 66–82. https://doi.org/10.1016/j.rser.2018.09.035.

[13] A. Arabgolarcheh, S. Jannesarahamdi, E. Benini, Modeling of Wake Characteristics in Floating Offshore Wind Turbines Using an Actuator Line Method, SSRN Electronic Journal (2021). https://doi.org/10.2139/SSRN.3883871.

[14] E.C. Edwards, A. Holcombe, S. Brown, E. Ransley, M. Hann, D. Greaves, Evolution of floating offshore wind platforms: A review of at-sea devices, Renewable and Sustainable Energy Reviews 183 (2023) 113416. https://doi.org/10.1016/J.RSER.2023.113416.

[15] A. Henderson, D. Witcher, Floating offshore wind energy - A review of the current status and an assessment of the prospects, Wind Engineering 34 (2010) 1–16. https://doi.org/10.1260/0309-524X.34.1.1.

[16] J. Cruz, M. Atcheson, Floating offshore wind energy: the next generation of wind energy, 2016. https://books.google.com/books?hl=en&lr=&id=u7nhDAAAQBAJ&oi=fnd&pg=PR5&ots=EZDKniF25V&sig=NcffOK_QH9HVukEGcHMn6g1PXgU (accessed July 22, 2024).

[17] M. Leimeister, A. Kolios, M.C.-J. of physics: Conference, undefined 2018, Critical review of floating support structures for offshore wind farm deployment, Iopscience.Iop.OrgM Leimeister, A Kolios, M ColluJournal of Physics: Conference

Series, 2018•iopscience.Iop.Org (n.d.). https://doi.org/10.1088/1742-6596/1104/1/012007.

[18] (14) Engineering Challenges for Floating Offshore Wind Turbines | Request PDF, (n.d.). https://www.researchgate.net/publication/237741317_Engineering_Challenges_for_Floating_Offshore_Wind_Turbines (accessed July 24, 2024).

[19] Z. Li, W. Zhang, H. Dong, Y. Tian, Performance analysis and structure optimization of a nautilus isometric spiral wind turbine, Energies (Basel) 13 (2019). https://doi.org/10.3390/EN13010120.

[20] Y. Liu, S. Li, Q. Yi, D. Chen, Developments in semi-submersible floating foundations supporting wind turbines: A comprehensive review, Renewable and Sustainable Energy Reviews 60 (2016) 433–449. https://doi.org/10.1016/J.RSER.2016.01.109.

[21] S. Watson, A. Moro, V. Reis, C. Baniotopoulos, S. Barth, G. Bartoli, F. Bauer, E. Boelman, D. Bosse, A. Cherubini, A. Croce, L. Fagiano, M. Fontana, A. Gambier, K. Gkoumas, C. Golightly, M.I. Latour, P. Jamieson, J. Kaldellis, A. Macdonald, J. Murphy, M. Muskulus, F. Petrini, L. Pigolotti, F. Rasmussen, P. Schild, R. Schmehl, N. Stavridou, J. Tande, N. Taylor, T. Telsnig, R. Wiser, Future emerging technologies in the wind power sector: A European perspective, Renewable and Sustainable Energy Reviews 113 (2019). https://doi.org/10.1016/j.rser.2019.109270.

[22] Offshore Wind Plant Verification Challenges | SDC Verifier, (n.d.). https://sdcverifier.com/articles/problems-of-floating-offshore-wind-plants-verification-according-to-industry-standards/ (accessed May 15, 2024).

[23] C. Ruzzo, V. Fiamma, M. Collu, G. Failla, V. Nava, F. Arena, On intermediate-scale open-sea experiments on floating offshore structures: Feasibility and application on a spar support for offshore wind turbines, Marine Structures 61 (2018) 220–237. https://doi.org/10.1016/J.MARSTRUC.2018.06.002.

[24] Corrosion Risks and Mitigation Strategies for Offshore Wind Turbine Foundations, (n.d.). https://www.materialsperformance.com/articles/material-selection-design/2016/03/corrosion-risks-and-mitigation-strategies-for-offshore-wind-turbine-foundations (accessed October 3, 2024).

[25] J. van der Tempel, N. Diepeveen, D. Cerda Salzmann, W. de Vries, Design of support structures for offshore wind turbines, (2010). https://doi.org/10.2495/978-1-84564-/205-1.

[26] S. Christiansen, Model-Based Control of a Ballast-Stabilized Floating Wind Turbine Exposed to Wind and Waves, (2013).

[27] M. Borg, M. Collu, A comparison between the dynamics of horizontal and vertical axis offshore floating wind turbines, Philosophical Transactions of the Royal Society A: Mathematical, Physical and Engineering Sciences 373 (2015). https://doi.org/10.1098/RSTA.2014.0076.

[28] M. Leimeister, A. Kolios, M. Collu, Critical review of floating support structures for offshore wind farm deployment, J Phys Conf Ser 1104 (2018). https://doi.org/10.1088/1742-6596/1104/1/012007.

[29] Y. Liu, S. Li, Q. Yi, D. Chen, Developments in semi-submersible floating foundations supporting wind turbines: A comprehensive review, Renewable and Sustainable Energy Reviews 60 (2016) 433–449. https://doi.org/10.1016/J.RSER.2016.01.109.

[30] M. Kausche, F. Adam, F. Dahlhaus, J. Großmann, Floating offshore wind - Economic and ecological challenges of a TLP solution, Renew Energy 126 (2018) 270–280. https://doi.org/10.1016/J.RENENE.2018.03.058.

[31] M. Shields, P. Beiter, J. Nunemaker, A. Cooperman, P. Duffy, Impacts of turbine and plant upsizing on the levelized cost of energy for offshore wind, Appl Energy 298 (2021) 117189. https://doi.org/10.1016/J.APENERGY.2021.117189.

[32] Y. Jiang, S. Liu, P. Zao, Y. Yu, L. Zou, L. Liu, J. Li, Experimental evaluation of a tree-shaped quad-rotor wind turbine on power output controllability and survival shutdown capability, Appl Energy 309 (2022) 118350. https://doi.org/10.1016/J.APENERGY.2021.118350.

[33] U. Göltenbott, Y. Ohya, S. Yoshida, P. Jamieson, Aerodynamic interaction of diffuser augmented wind turbines in multi-rotor systems, Renew Energy 112 (2017) 25–34. https://doi.org/10.1016/J.RENENE.2017.05.014.

[34] S. Amherst, P. Verma, Multi Rotor Wind Turbine Design And Cost Scaling, Masters Theses 1911 - February 2014 (2013). https://doi.org/https://doi.org/10.7275/4460782.

[35] L. Fingersh, M. Hand, A. Laxson, Wind Turbine Design Cost and Scaling Model, (2006). https://doi.org/10.2172/897434.

[36] Vestas Multi-Rotor Wind Turbine: 3 Blades Good, 4 Blades Better, (n.d.). https://cleantechnica.com/2016/07/05/vestas-multi-rotor-wind-turbine-3-blades-good-12-blades-better/ (accessed May 19, 2024).

[37] I.H. Sunde, R.E. Torres-Olguin, O. Anaya-Lara, M.P. Van Der Laan, M. Abkar, Improved energy production of multi-rotor wind farms, J Phys Conf Ser 1256 (2019) 012011. https://doi.org/10.1088/1742-6596/1256/1/012011.

[38] The blade load research of the multi-rotor wind turbine in wind shear folow, (n.d.). https://www.researchgate.net/publication/286231257_The_blade_load_research_of_the_multi-rotor_wind_turbine_in_wind_shear_folow (accessed May 19, 2024).

[39] P. Jameson, M. Branney, Multi-rotors; a solution to 20 MW and beyond?, Energy Procedia 24 (2012) 52–59. https://doi.org/10.1016/J.EGYPRO.2012.06.086.

[40] S.P. T, O. S, M. C, Aerodynamic interaction between two wind rotors set next to each other in one plane., European Wind Energy Conference 1984 (1985) 529–533. https://jglobal.jst.go.jp/en/detail?JGLOBAL_ID=200902063879084583 (accessed May 19, 2024).

[41] N.N. Ghaisas, A.A. Ghate, S.S. Lele, Effect of tip spacing, thrust coefficient and turbine spacing in multi-rotor wind turbines and farms, Wind Energy Science 5 (2020) 51–72. https://doi.org/10.5194/WES-5-51-2020.

[42] G.A. Speakman, M. Abkar, L.A. Martínez-Tossas, M. Bastankhah, Wake steering of multirotor wind turbines, Wind Energy 24 (2021) 1294–1314. https://doi.org/10.1002/WE.2633.

[43] M. Bastankhah, M. Abkar, Multirotor wind turbine wakes, Physics of Fluids 31 (2019). https://doi.org/10.1063/1.5097285/1033054.

[44] Marine Renewable Energy Blog: Floating Wind Turbines: all the systems reviewed, (n.d.). https://marinerenewableenergy.blogspot.com/2011/07/floating-wind-turbines-all-systems.html (accessed October 3, 2024).

[45] Single- vs. Multi-Platform - Floating Wind Turbines, (n.d.). https://floatingwindfarm.weebly.com/single--vs-multi-platform.html (accessed October 3, 2024).

[46] Giant floating wall of wind turbines moves a step closer to reality | TechSpot, (n.d.). https://www.techspot.com/news/103933-massive-floating-wall-wind-turbines-moves-step-closer.html (accessed October 3, 2024).

[47] SSAB, Hexicon to Optimize Steel for Offshore Wind Platforms | Offshore Wind, (n.d.). https://www.offshorewind.biz/2014/05/12/ssab-hexicon-to-optimize-steel-for-offshore-wind-platforms/ (accessed May 15, 2024).

[48] SSAB and Hexicon agree to develop floating platforms for wind power, (n.d.). https://www.windpowerengineering.com/ssab-hexicon-agree-develop-floating-platforms-wind-power/ (accessed October 3, 2024).

[49] Offshore wind for the future, (n.d.). https://forcetechnology.com/no/cases/offshore-wind-for-the-future (accessed July 25, 2024).

[50] Floating wind turbine platforms, (n.d.). https://forcetechnology.com/en/cases/windsea-floating-wind-turbine-platforms (accessed October 3, 2024).

[51] M.A. Siddiqui, F.C.W. Hanssen, M. Greco, E. Anda, Comparing the Utility of Coupled Aero-Hydrodynamic Analysis Using a CFD Solver versus a Potential Flow Solver for Floating Offshore Wind Turbines, Energies 2023, Vol. 16, Page 7833 16 (2023) 7833. https://doi.org/10.3390/EN16237833.

[52] J.R. Morison, M.P. O'brien, J.W. Johnson, S.A. Schaaf, The Force Exerted by Surface Waves on Piles, Journal of Petroleum Technology 2 (1950) 149–154. https://doi.org/10.2118/950149-G.

[53] A. Otter, J. Murphy, V. Pakrashi, A. Robertson, C. Desmond, A review of modelling techniques for floating offshore wind turbines, Wind Energy (2021). https://doi.org/10.1002/we.2701.

[54] M.A. Benitz, D.P. Schmidt, M.A. Lackner, G.M. Stewart, J. Jonkman, A. Robertson, Validation of Hydrodynamic Load Models Using CFD for the OC4-DeepCwind Semisubmersible, in: Volume 9: Ocean Renewable Energy, American Society of Mechanical Engineers, 2015. https://doi.org/10.1115/OMAE2015-41045.

[55] M. Sirigu, E. Faraggiana, A. Ghigo, G. Bracco, Development of MOST, a fast simulation model for optimisation of floating offshore wind turbines in Simscape Multibody, J Phys Conf Ser 2257 (2022). https://doi.org/10.1088/1742-6596/2257/1/012003.

[56] L. Pustina, C. Lugni, G. Bernardini, J. Serafini, M. Gennaretti, Control of power generated by a floating offshore wind turbine perturbed by sea waves, Renewable and Sustainable Energy Reviews 132 (2020). https://doi.org/10.1016/J.RSER.2020.109984.

[57] D. Ward, M. Collu, J. Sumner, Reducing tower fatigue through blade back twist and active pitch-to-stall control strategy for a semi-submersible floating offshore wind turbine, Energies (Basel) 12 (2019). https://doi.org/10.3390/EN12101897.

[58] F. Porté-Agel, M. Bastankhah, S. Shamsoddin, Wind-Turbine and Wind-Farm Flows: A Review, Boundary Layer Meteorol 174 (2019) 1–59. https://doi.org/10.1007/S10546-019-00473-0.

[59] P.K. Jha, M.J. Churchfield, P.J. Moriarty, S. Schmitz, Guidelines for volume force distributions within actuator line modeling of wind turbines on large-eddy simulation-type grids, Journal of Solar Energy Engineering, Transactions of the ASME 136 (2014). https://doi.org/10.1115/1.4026252.

[60] J. Bosch, I. Staffell, A.D. Hawkes, Global levelised cost of electricity from offshore wind, Energy 189 (2019). https://doi.org/10.1016/J.ENERGY.2019.116357.

[61] M. Kausche, F. Adam, F. Dahlhaus, J. Großmann, Floating offshore wind - Economic and ecological challenges of a TLP solution, Renew Energy 126 (2018) 270–280. https://doi.org/10.1016/J.RENENE.2018.03.058.

[62] A. Rezaeiha, R. Pereira, M. Kotsonis, Fluctuations of angle of attack and lift coefficient and the resultant fatigue loads for a large Horizontal Axis Wind turbine, Renew Energy 114 (2017) 904–916. https://doi.org/10.1016/J.RENENE.2017.07.101.

[63] T. Wang, H. Jin, X. Wu, Coupled Dynamic Analysis of a Tension Leg Platform Floating Offshore Wind Turbine, Journal of Offshore Mechanics and Arctic Engineering 142 (2020). https://doi.org/10.1115/1.4044075/955898.

[64] Y. Liu, Q. Xiao, A. Incecik, C. Peyrard, D. Wan, Establishing a fully coupled CFD analysis tool for floating offshore wind turbines, Renew Energy 112 (2017) 280–301. https://doi.org/10.1016/J.RENENE.2017.04.052.

[65] Y.P. Chodnekar, S. Mandal, K. Balakrishna Rao, Hydrodynamic analysis of floating offshore wind turbine, Procedia Eng 116 (2015) 4–11. https://doi.org/10.1016/J.PROENG.2015.08.258.

[66] P. Trubat, C. Molins, X. Gironella, Wave hydrodynamic forces over mooring lines on floating offshore wind turbines, Ocean Engineering 195 (2020). https://doi.org/10.1016/J.OCEANENG.2019.106730.

[67] J.M. Jonkman, M.L.Jr. Buhl, FAST User's Guide - Updated August 2005, Related Information: For Latest Updates Go to Http://Wind.Nrel.Gov/Designcodes/Simulators/Fast/FAST.Pdf (2005). https://doi.org/10.2172/15020796.

[68] L. Roald, J. Jonkman, A. Robertson, N. Chokani, The effect of second-order hydrodynamics on floating offshore wind turbines, Energy Procedia 35 (2013) 253–264. https://doi.org/10.1016/J.EGYPRO.2013.07.178.

[69] G.K.Y. Chan, P.D. Sclavounos, J. Jonkman, G. Hayman, Computation of Nonlinear Hydrodynamic Loads on Floating Wind Turbines Using Fluid-Impulse Theory, Proceedings of the International Conference on Offshore Mechanics and Arctic Engineering - OMAE 9 (2015). https://doi.org/10.1115/OMAE2015-41053.

[70] H. Shin, P. Thanh Dam, K. Jin Jung, J. Song, C. Rim, T. Chung, Model test of new floating offshore wind turbine platforms, International Journal of Naval Architecture and Ocean Engineering 5 (2013) 199–209. https://doi.org/10.3744/JNAOE.2013.5.2.199.

[71] T. Sebastian, M. Lackner, Analysis of the induction andwake evolution of an offshore floating wind turbine, Energies (Basel) 5 (2012) 968–1000. https://doi.org/10.3390/EN5040968.

[72] D. Micallef, A. Rezaeiha, Floating offshore wind turbine aerodynamics: Trends and future challenges, Renewable and Sustainable Energy Reviews 152 (2021). https://doi.org/10.1016/J.RSER.2021.111696.

[73] Y. Fang, L. Duan, Z. Han, Y. Zhao, H. Yang, Numerical analysis of aerodynamic performance of a floating offshore wind turbine under pitch motion, Energy 192 (2020). https://doi.org/10.1016/J.ENERGY.2019.116621.

[74] S. Fu, Y. Jin, Y. Zheng, L.P. Chamorro, Wake and power fluctuations of a model wind turbine subjected to pitch and roll oscillations, Appl Energy 253 (2019). https://doi.org/10.1016/J.APENERGY.2019.113605.

[75] X. Shen, J. Chen, P. Hu, X. Zhu, Z. Du, Study of the unsteady aerodynamics of floating wind turbines, Energy 145 (2018) 793–809. https://doi.org/10.1016/j.energy.2017.12.100.

[76] V. Leble, G. Barakos, 10-MW Wind Turbine Performance under Pitching and Yawing Motion, Journal of Solar Energy Engineering, Transactions of the ASME 139 (2017). https://doi.org/10.1115/1.4036497/379737.

[77] B. Wen, X. Dong, X. Tian, Z. Peng, W. Zhang, K. Wei, The power performance of an offshore floating wind turbine in platform pitching motion, Energy 154 (2018) 508–521. https://doi.org/10.1016/J.ENERGY.2018.04.140.

[78] T. Sant, D. Bonnici, R. Farrugia, D. Micallef, Measurements and modelling of the power performance of a model floating wind turbine under controlled conditions, Wind Energy 18 (2015) 811–834. https://doi.org/10.1002/WE.1730.

[79] D. Micallef, T. Sant, Loading effects on floating offshore horizontal axis wind turbines insurge motion, Renew Energy 83 (2015) 737–748. https://doi.org/10.1016/J.RENENE.2015.05.016.

[80] M. Jeon, S. Lee, S. Lee, Unsteady aerodynamics of offshore floating wind turbines in platform pitching motion using vortex lattice method, Renew Energy 65 (2014) 207–212. https://doi.org/10.1016/j.renene.2013.09.009.

[81] L. Lin, K. Wang, D. Vassalos, Detecting wake performance of floating offshore wind turbine, Ocean Engineering 156 (2018) 263–276. https://doi.org/10.1016/J.OCEANENG.2018.03.028.

[82] A. Rezaeiha, D. Micallef, Wake interactions of two tandem floating offshore wind turbines: CFD analysis using actuator disc model, Renew Energy 179 (2021) 859–876. https://doi.org/10.1016/J.RENENE.2021.07.087.

[83] T. Göçmen, P. Van Der Laan, P.E. Réthoré, A.P. Diaz, G.C. Larsen, S. Ott, Wind turbine wake models developed at the technical university of Denmark: A review, Renewable and Sustainable Energy Reviews 60 (2016) 752–769. https://doi.org/10.1016/J.RSER.2016.01.113.

[84] N. Couto, A. Rouboa, E. Monteiro, J. Viera, Computational Fluid Dynamics Analysis of Greenhouses with Artificial Heat Tube, World Journal of Mechanics 02 (2012) 181–187. https://doi.org/10.4236/WJM.2012.24022.

[85] R.J. Barthelmie, L. Folkerts, G.C. Larsen, K. Rados, S.C. Pryor, S.T. Frandsen, B. Lange, G. Schepers, Comparison of Wake Model Simulations with Offshore Wind Turbine Wake Profiles Measured by Sodar, J Atmos Ocean Technol 23 (2006) 888–901. https://doi.org/10.1175/JTECH1886.1.

[86] T. Burton, N. Jenkins, E. Bossanyi, D. Sharpe, M. Graham, Wind Energy Handbook, Third Edition, Wind Energy Handbook: Third Edition (2021) 1–952. https://doi.org/10.1002/9781119992714.

[87] J.F. Manwell, J.G. McGowan, A.L. Rogers, Wind Energy Explained: Theory, Design and Application, Wind Energy Explained: Theory, Design and Application (2010). https://doi.org/10.1002/9781119994367.

[88] Enhanced CFD Modeling of Wind Turbine Wakes - Universidad ..., (n.d.). https://www.yumpu.com/en/document/view/10274939/enhanced-cfd-modeling-of-wind-turbine-wakes-universidad- (accessed May 15, 2024).

[89] M.P. Van Der Laan, N.N. Sørensen, P.E. Réthoré, J. Mann, M.C. Kelly, N. Troldborg, The k-ε-fP model applied to double wind turbine wakes using different actuator disk force methods, Wind Energy 18 (2015) 2223–2240. https://doi.org/10.1002/WE.1816.

[90] H. Glauert, Airplane Propellers, Aerodynamic Theory (1935) 169–360. https://doi.org/10.1007/978-3-642-91487-4_3.

[91] M.O.L. Hansen, Aerodynamics of wind turbines: Third edition, Aerodynamics of Wind Turbines: Third Edition (2015) 1–173. https://doi.org/10.4324/9781315769981.

[92] Actuator Disc Methods Applied to Wind Turbines – Projects — Welcome to DTU Research Database, (n.d.). https://orbit.dtu.dk/en/publications/actuator-disc-methods-applied-to-wind-turbines/projects/ (accessed May 16, 2024).

[93] S. Voutsinas, State of the art in wind turbine aerodynamics and aeroelasticity, Prog Aerosp Sci (2006). https://www.academia.edu/52119484/State_of_the_art_in_wind_turbine_aerodynamics_and_aeroelasticity (accessed May 16, 2024).

[94] A. Crespo, J. Hernández, Turbulence characteristics in wind-turbine wakes, Journal of Wind Engineering and Industrial Aerodynamics 61 (1996) 71–85. https://doi.org/10.1016/0167-6105(95)00033-X.

[95] R.J. Barthelmie, L. Folkerts, G.C. Larsen, K. Rados, S.C. Pryor, S.T. Frandsen, B. Lange, G. Schepers, Comparison of Wake Model Simulations with Offshore Wind Turbine Wake Profiles Measured by Sodar, J Atmos Ocean Technol 23 (2006) 888–901. https://doi.org/10.1175/JTECH1886.1.

[96] D.J. Renkema, Validation of wind turbine wake models: Using wind farm data and wind tunnel measurements, (2007). https://repository.tudelft.nl/islandora/object/uuid%3A0fbea4b9-990a-4d03-bb97-3474c4728d2f (accessed May 16, 2024).

[97] Wind Energy | Research | Gruppo di ricerca REASE - UniFI, (n.d.). https://www.rease.unifi.it/vp-166-wind-energy.html (accessed May 16, 2024).

[98] B. Lange, H.P. Waldl, A.G. Guerrero, D. Heinemann, R.J. Barthelmie, Modelling of offshore wind turbine wakes with the wind farm program FLaP, Wind Energy 6 (2003) 87–104. https://doi.org/10.1002/WE.84.

[99] M.D. Esteban, J.J. Diez, J.S. López, V. Negro, Why offshore wind energy?, Renew Energy 36 (2011) 444–450. https://doi.org/10.1016/J.RENENE.2010.07.009.

[100] S. Frandsen, On the wind speed reduction in the center of large clusters of wind turbines, Journal of Wind Engineering and Industrial Aerodynamics 39 (1992) 251–265. https://doi.org/10.1016/0167-6105(92)90551-K.

[101] [PDF] A note on wind generator interaction | Semantic Scholar, (n.d.). https://www.semanticscholar.org/paper/A-note-on-wind-generator-interaction-Jensen/385f829b931fa647df18d8f2226dd577b63f8660 (accessed May 19, 2024).

[102] I. Katic, A simple model for cluster efficiency, (1986). https://www.academia.edu/79033727/A_simple_model_for_cluster_efficiency (accessed May 19, 2024).

[103] [PDF] Wind Atlas Analysis and Application program (WAsP): Vol. 3: Utility programs | Semantic Scholar, (n.d.). https://www.semanticscholar.org/paper/Wind-Atlas-Analysis-and-Application-program-(WAsP)%3A-Mortensen-Landberg/90205d3de1801104e520cea03f03250437d83a27 (accessed May 19, 2024).

[104] A. Peña, O. Rathmann, Atmospheric stability-dependent infinite wind-farm models and the wake-decay coefficient, Wind Energy 17 (2014) 1269–1285. https://doi.org/10.1002/WE.1632.

[105] A. Penã, P.E. Réthoré, M.P. Van Der Laan, On the application of the Jensen wake model using a turbulence-dependent wake decay coefficient: The Sexbierum case, Wind Energy 19 (2016) 763–776. https://doi.org/10.1002/WE.1863.

[106] (13) (PDF) On the application of the Jensen wake model using a turbulence-dependent wake decay coefficient: The Sexbierum case, (n.d.). https://www.researchgate.net/publication/276074083_On_the_application_of_the_Jensen_wake_model_using_a_turbulence-dependent_wake_decay_coefficient_The_Sexbierum_case (accessed May 19, 2024).

[107] A. Peña, P.E. Réthoré, O. Rathmann, Modeling large offshore wind farms under different atmospheric stability regimes with the Park wake model, Renew Energy 70 (2014) 164–171. https://doi.org/10.1016/j.renene.2014.02.019.

[108] G.Chr. Larsen, A Simple Wake Calculation Procedure, Risø National Laboratory, 1988. https://orbit.dtu.dk/en/publications/a-simple-wake-calculation-procedure (accessed May 19, 2024).

[109] T. Göçmen, P. Van Der Laan, P.E. Réthoré, A.P. Diaz, G.C. Larsen, S. Ott, Wind turbine wake models developed at the technical university of Denmark: A review, Renewable and Sustainable Energy Reviews 60 (2016) 752–769. https://doi.org/10.1016/J.RSER.2016.01.113.

[110] G.Chr. Larsen, A simple stationary semi-analytical wake model, Risø National Laboratory for Sustainable Energy, Technical University of Denmark, 2009.

https://orbit.dtu.dk/en/publications/a-simple-stationary-semi-analytical-wake-model (accessed May 19, 2024).

[111] R.E. Keck, D. Veldkamp, H.A. Madsen, G. Larsen, Implementation of a mixing length turbulence formulation into the dynamic wake meandering model, Journal of Solar Energy Engineering, Transactions of the ASME 134 (2012). https://doi.org/10.1115/1.4006038.

[112] G.C.; Larsen, H.; Madsen Aagaard, F.; Bingöl, J.; Mann, S.; Ott, J.N.; Sørensen, V.; Okulov, N.; Troldborg, N. Nielsen, ; Morten, K. Thomsen, G.C. Larsen, M. Aagaard, H. Bingöl, J. Ott, Dynamic wake meandering modeling, Risø National Laboratory, 2007. https://orbit.dtu.dk/en/publications/dynamic-wake-meandering-modeling (accessed May 19, 2024).

[113] (13) (PDF) Theoretical prediction of dynamic-in ow derivatives, (n.d.). https://www.researchgate.net/publication/238355026_Theoretical_prediction_of_dynamic-in_ow_derivatives (accessed May 19, 2024).

[114] E. Branlard, Vortex systems and models of a rotor - bound, root and wake vorticity, Research Topics in Wind Energy 7 (2017) 121–133. https://doi.org/10.1007/978-3-319-55164-7_5.

[115] Q. Guo, L. Zhou, Z. Wang, Comparison of BEM-CFD and full rotor geometry simulations for the performance and flow field of a marine current turbine, Renew Energy 75 (2015) 640–648. https://doi.org/10.1016/J.RENENE.2014.10.047.

[116] M. Edmunds, A.J. Williams, I. Masters, A. Banerjee, J.H. VanZwieten, A spatially nonlinear generalised actuator disk model for the simulation of horizontal axis wind and tidal turbines, Energy 194 (2020). https://doi.org/10.1016/J.ENERGY.2019.116803.

[117] N. Troldborg, Actuator Line Modeling of Wind Turbine Wakes, 2009. https://orbit.dtu.dk/en/publications/actuator-line-modeling-of-wind-turbine-wakes (accessed May 19, 2024).

[118] P.K. Jha, M.J. Churchfield, P.J. Moriarty, S. Schmitz, Guidelines for volume force distributions within actuator line modeling of wind turbines on large-eddy simulation-type grids, Journal of Solar Energy Engineering, Transactions of the ASME 136 (2014) 1–11. https://doi.org/10.1115/1.4026252.

[119] R. Mikkelsen, J.N. Sørensen, S. Øye, N. Troldborg, Analysis of power enhancement for a row of wind turbines using the actuator line technique, J Phys Conf Ser 75 (2007). https://doi.org/10.1088/1742-6596/75/1/012044.

[120] P.K. Jha, M.J. Churchfield, P.J. Moriarty, S. Schmitz, Accuracy of state-of-the-art actuator-line modeling for wind turbine wakes, 51st AIAA Aerospace Sciences Meeting Including the New Horizons Forum and Aerospace Exposition 2013 (2013). https://doi.org/10.2514/6.2013-608.

[121] W.Z. Shen, R. Mikkelsen, J.N. Sørensen, C. Bak, Tip loss corrections for wind turbine computations, Wind Energy 8 (2005) 457–475. https://doi.org/10.1002/WE.153.

[122] L.A. Martinez-Tossas, C. Meneveau, Filtered lifting line theory and application to the actuator line model, J Fluid Mech 863 (2019) 269–292. https://doi.org/10.1017/JFM.2018.994.

[123] B. Rocchio, U. Ciri, M.V. Salvetti, S. Leonardi, Appraisal and calibration of the actuator line model for the prediction of turbulent separated wakes, Wind Energy 23 (2020) 1231–1248. https://doi.org/10.1002/WE.2483.

[124] L.A. Martínez-Tossas, M.J. Churchfield, C. Meneveau, Optimal smoothing length scale for actuator line models of wind turbine blades based on Gaussian body force distribution, Wind Energy 20 (2017) 1083–1096. https://doi.org/10.1002/WE.2081.

[125] C.S. Watters, C. Masson, Modeling of lifting-device aerodynamics using the actuator surface concept, Int J Numer Methods Fluids 62 (2010) 1264–1298. https://doi.org/10.1002/FLD.2064.

[126] M. Shives, C. Crawford, Mesh and load distribution requirements for actuator line CFD simulations, Wind Energy 16 (2013) 1183–1196. https://doi.org/10.1002/WE.1546.

[127] L.A. Martínez-Tossas, M.J. Churchfield, S. Leonardi, Large eddy simulations of the flow past wind turbines: Actuator line and disk modeling, Wind Energy 18 (2015) 1047–1060. https://doi.org/10.1002/WE.1747.

[128] A.C.W. Creech, A.G.L. Borthwick, D. Ingram, Effects of Support Structures in an LES Actuator Line Model of a Tidal Turbine with Contra-Rotating Rotors, Energies (Basel) 10 (2017) 1–25. https://ideas.repec.org/a/gam/jeners/v10y2017i5p726-d99155.html (accessed May 19, 2024).

[129] M. Edmunds, A.J. Williams, I. Masters, T.N. Croft, An enhanced disk averaged CFD model for the simulation of horizontal axis tidal turbines, Renew Energy 101 (2017) 67–81. https://doi.org/10.1016/J.RENENE.2016.08.007.

[130] P. Mycek, B. Gaurier, G. Germain, G. Pinon, E. Rivoalen, Experimental study of the turbulence intensity effects on marine current turbines behaviour. Part I: One single turbine, Renew Energy 66 (2014) 729–746. https://doi.org/10.1016/j.renene.2013.12.036.

[131] A. Wimshurst, R.H.J. Willden, Extracting lift and drag polars from blade-resolved computational fluid dynamics for use in actuator line modelling of horizontal axis turbines, Wind Energy 20 (2017) 815–833. https://doi.org/10.1002/WE.2065.

[132] W.Z. Shen, J.N. Sørensen, R. Mikkelsen, Tip loss correction for actuator/Navier-Stokes computations, Journal of Solar Energy Engineering, Transactions of the ASME 127 (2005) 209–213. https://doi.org/10.1115/1.1850488.

[133] A. Wimshurst, R.H.J. Willden, Analysis of a tip correction factor for horizontal axis turbines, Wind Energy 20 (2017) 1515–1528. https://doi.org/10.1002/WE.2106.

[134] A. Wimshurst, R.H.J. Willden, Computational observations of the tip loss mechanism experienced by horizontal axis rotors, Wind Energy 21 (2018) 544–557. https://doi.org/10.1002/WE.2177.

[135] L.A. Martínez-Tossas, M.J. Churchfield, A.E. Yilmaz, H. Sarlak, P.L. Johnson, J.N. Sørensen, J. Meyers, C. Meneveau, Comparison of four large-eddy simulation research codes and effects of model coefficient and inflow turbulence in actuator-line-based wind turbine modeling, Journal of Renewable and Sustainable Energy 10 (2018). https://doi.org/10.1063/1.5004710.

[136] View article, (n.d.). https://scholar.google.com/citations?view_op=view_citation&hl=en&user=uKlecC4AAAAJ&citation_for_view=uKlecC4AAAAJ:gsN89kCJA0AC (accessed October 3, 2024).

[137] A. Arabgolarcheh, S. Jannesarahmadi, E. Benini, Modeling of near wake characteristics in floating offshore wind turbines using an actuator line method, Renew Energy 185 (2022) 871–887. https://doi.org/10.1016/J.RENENE.2021.12.099.

[138] M.J. Churchfield, S. Schreck, L.A. Martínez-Tossas, C. Meneveau, P.R. Spalart, An advanced actuator line method for wind energy applications and beyond, 35th Wind Energy Symposium, 2017 (2017). https://doi.org/10.2514/6.2017-1998.

[139] A. Mittal, K. Sreenivas, L.K. Taylor, L. Hereth, Improvements to the actuator line modeling for wind turbines, 33rd Wind Energy Symposium (2015). https://doi.org/10.2514/6.2015-0216.

[140] W.Z. Shen, W.J. Zhu, J.N. Sørensen, Actuator line/Navier-Stokes computations for the MEXICO rotor: Comparison with detailed measurements, Wind Energy 15 (2012) 811–825. https://doi.org/10.1002/WE.510.

[141] H.G. Weller, G. Tabor, H. Jasak, C. Fureby, A tensorial approach to computational continuum mechanics using object-oriented techniques, Computers in Physics 12 (1998) 620. https://doi.org/10.1063/1.168744.

[142] F. Porté-Agel, M. Bastankhah, S. Shamsoddin, Wind-Turbine and Wind-Farm Flows: A Review, Boundary Layer Meteorol 174 (2020) 1–59. https://doi.org/10.1007/s10546-019-00473-0.

[143] R. Chow, C.P. Van Dam, Verification of computational simulations of the NREL 5 MW rotor with a focus on inboard flow separation, Wind Energy 15 (2012) 967–981. https://doi.org/10.1002/WE.529.

[144] T.O. Foundation, OpenFOAM: User Guide, n.d.

[145] T.-H. Shih, W.W. Liou, A. Shabbir, Z. Yang, J. Zhu, A new k-ϵ eddy viscosity model for high reynolds number turbulent flows, Comput Fluids 24 (1995) 227–238. https://doi.org/10.1016/0045-7930(94)00032-T.

[146] B.E. Launder, D.B. Spalding, The numerical computation of turbulent flows, Comput Methods Appl Mech Eng 3 (1974) 269–289. https://doi.org/10.1016/0045-7825(74)90029-2.

[147] M.M. Hand, D. a Simms, L.J. Fingersh, D.W. Jager, J.R. Cotrell, S. Schreck, S.M. Larwood, Unsteady Aerodynamics Experiment Phase VI: Wind Tunnel Test Configurations and Available Data Campaigns, Golden, CO, 2001. https://doi.org/10.2172/15000240.

[148] P. Giguere, M.S. Selig, Design of a tapered and twisted blade for the NREL combined experiment rotor, National Renewable Energy Lab., Golden, CO (US), 1999.

[149] D.M. Somers, Design and experimental results for the S809 airfoil, Golden, CO (United States), 1997. https://doi.org/No. NREL/SR-440-6918.

[150] M.M. Hand, D.A. Simms, L.J. Fingersh, D.W. Jager, J.R. Cotrell, S. Schreck, S.M. Larwood, Unsteady Aerodynamics Experiment Phase VI: Wind Tunnel Test Configurations and Available Data Campaigns, (2001). https://doi.org/10.2172/15000240.

[151] A. Arabgolarcheh, S. Jannesarahmadi, E. Benini, L. Menegozzo, Numerical Study of a Horizontal Wind Turbine under Yaw Conditions, Math Probl Eng 2021 (2021) 1–17. https://doi.org/10.1155/2021/9978134.

[152] J.M. Jonkman, M.L.Jr. Buhl, FAST User's Guide - Updated August 2005, Golden, CO, 2005. https://doi.org/10.2172/15020796.

[153] P. Cheng, Y. Huang, D. Wan, A numerical model for fully coupled aero-hydrodynamic analysis of floating offshore wind turbine, Ocean Engineering 173 (2019) 183–196. https://doi.org/10.1016/j.oceaneng.2018.12.021.

[154] B.D. Hirth, J.L. Schroeder, Documenting Wind Speed and Power Deficits behind a Utility-Scale Wind Turbine, J Appl Meteorol Climatol 52 (2013) 39–46. https://doi.org/10.1175/JAMC-D-12-0145.1.

[155] N.N. Sørensen, J. Johansen, UPWIND, aerodynamics and aero-elasticity rotor aerodynamics in atmospheric shear flow, European Wind Energy Conference and Exhibition 2007, EWEC 2007 2 (2007) 1233–1241.

[156] H. Lee, D.J. Lee, Effects of platform motions on aerodynamic performance and unsteady wake evolution of a floating offshore wind turbine, Renew Energy 143 (2019) 9–23. https://doi.org/10.1016/j.renene.2019.04.134.

[157] L. Menegozzo, A. Dal Monte, E. Benini, A. Benato, Small wind turbines: A numerical study for aerodynamic performance assessment under gust conditions, Renew Energy (2018). https://doi.org/10.1016/j.renene.2017.12.086.

[158] N. Sedaghatizadeh, M. Arjomandi, R. Kelso, B. Cazzolato, M.H. Ghayesh, Modelling of wind turbine wake using large eddy simulation, Renew Energy 115 (2018) 1166–1176. https://doi.org/10.1016/j.renene.2017.09.017.

[159] A. Lamei, M. Hayatdavoodi, H.R. Riggs, R.C. Ertekin, Dynamic response of multi-unit floating offshore wind turbines to wave, current, and wind loads, Journal of Renewable and Sustainable Energy 16 (2024). https://doi.org/10.1063/5.0172543.

[160] J. JEong, F. Hussain, On the identification of a vortex, J Fluid Mech 285 (1995) 69–94. https://doi.org/10.1017/S0022112095000462.